"Thermoelectric properties of nanostructured and nanoparticular compounds"

Dissertation

zur Erlangung des akademischen Grades eines
"Doktor der Naturwissenschaften"

am Fachbereich Chemie,
Pharmazie und Geowissenschaften der

Johannes Gutenberg-Universität Mainz

Gregor Kieslich
geboren in Mannheim

Mainz, Juni 2013

Dekan:	Prof. Dr. [redacted]
Erstgutachter:	Prof. Dr. [redacted]
Zweitgutachter:	Prof. Dr. [redacted]
Tag der mündlichen Prüfung:	26.06.2013

Für meine Familie

Die experimentellen Arbeiten welche dieser Arbeit zugrunde liegen wurden im Zeitraum vom 1. Oktober 2010 bis 1. Juni 2013 unter der Leitung von Herrn Prof. Dr. [redacted] an der *Johannes Gutenberg-Universität Mainz*, Herrn Prof. Dr. [redacted] am *Max Planck Institut für Chemische Physik fester Stoffe Dresden* und Herrn Prof. Dr. [redacted] an der *University of California Santa Barbara (UCSB), USA* durchgeführt.

The work for this thesis was carried out at the *Johannes Gutenberg-Universität Mainz*, at the *Max Planck Institute Dresden* and the *University of California Santa Barbara* in the period between October 1st 2010 and July 1st 2013 under the guidance of Prof. Dr. [redacted], Prof. Dr. [redacted] and Prof. Dr. [redacted].

Mainz, 2013

Publications

[9] **G. Kieslich**, C. S. Birkel, M. Gaultois, R. Seshadri, G. Stucky, Y. Grin, W. Tremel "Reduced thermal conductivity via nanosized crystallites and defects: enhanced thermoelectric properties of the *n*-tpye Magnéli oxide $WO_{2.90}$" *J. Am. Chem. Soc.* submitted.

[8] **G. Kieslich**, C. S. Birkel, M. Gaultois, R. Seshadri, G. Stucky, Y. Grin, W. Tremel "SPS-assisted preparation of the Magnéli phase $WO_{2.90}$ for thermoelectric applications" *J. Mater. Chem. A* submitted.

[7] **G. Kieslich**, I. Veremchuck, W. G. Zeier, C. Birkel, K. Weldert, C. P. Heinrich, E. Visnow, M. Panthoefer, Y. Grin, W. Tremel "Using Crystallographic Shear to Reduce Lattice Thermal Conductivity: High Temperature Thermoelectric Characterization of the Spark Plasma Sintered Magnéli Phases $WO_{2.90}$ and $WO_{2.722}$" *Phys. Chem. Chem Phys.* **2012**, DOI:10.1039/C3CP52361F.

[6] **G. Kieslich**, C.S. Birkel, I. Veremchuk, Y. Grin, W. Tremel "Thermoelectric properties of nanoparticular $FeSb_2$ prepared by a facile wet chemistry approach" *Dalton Trans.* **2013**, submitted.

[5] T. Claudio, D. Bessas, C.S. Birkel, **G. Kieslich**, M. Panthoefer, I. Sergueev, W. Tremel, R. P. Hermann "Enhanced Debye level in nano $Zn_{1+x}Sb$,$FeSb_2$ and NiSb: nuclear inelastic spectroscopy on ^{121}Sb" *Phys. Stat. Sol. A* **2013**, submitted.

[4] **G. Kieslich***, E. Morsbach*, C. Heinrich, C.S. Birkel, M. Panthoefer, W. Tremel "Wet chemistry route and oxidative purification of $CoSb_3$ nanoparticles" *Physica Status Solidi A*, **2013**, to be submitted.

[3] C. S. Birkel, **G. Kieslich**, D. Bessas, T. Claudio, R. Branscheid, U. Kolb, M. Panthoefer, R. Hermann, W. Tremel "Wet Chemical Synthesis and a Combined X-ray and Moessbauer Study of the Formation of $FeSb_2$ Nanoparticles" *Inorg. Chem.* **2011**, 50, 11807, [DOI: 10.1021/ic201940r].

[2] **G. Kieslich**, C. S. Birkel, A. Stewart, U. Kolb, W. Tremel "Solution Synthesis of Nanoparticular Binary Transition Metal Antimonides." *Inorg. Chem.* **2011**, 50, 6938. [DOI: 10.1021/ic200074z]

[1] C. S. Birkel, T. Claudio, M. Panthoefer, A. Birkel, D. Koll, **G. Kieslich**, J. Schmidt, R. Hermann, W. Tremel "Properties of Spark Plasma Sintered Nanostructured $Zn_{1+x}Sb$" *Phys. Stat. Sol. A* **2011**, 208, 1913. [DOI: 10.1002/pssa.201026665]

Acknowledgements

A lot of people supported me during the last three years and made this thesis possible, not only scientifically, but also mentally - many thanks to all of you! However, some special thanks in the following lines.

At the beginning I want to thank my supervisor Prof. Dr. [redacted] for giving me the opportunity to work on such an interesting research topic. Besides, he always took time to discuss any occuring problems. I also want to thank Prof. Dr. [redacted] for the fruitful discussions and collaboration. I have learned a lot during my several visits in Dresden and without you and [redacted] the Magnéli project would not have been that successfull. Also thanks to Prof. Dr. [redacted] and [redacted] for the productive discussions during the several MAINZ meetings.

Many thanks to my supervisors abroad, Prof. Dr. [redacted] and Prof. Dr. [redacted]. Research at the UCSB has been lot of fun due to a perfect mixture of motivation, knowledge, sun, beach and BBQ'ing. Thank you for giving me this amazing opportunity.

I want to give thanks to the Konrad-Adenauer Stiftung not only for the financial support but also for the off-topic seminars I visited. During the several seminars I learned a lot about culture, society and myself than I could ever imagine. I also want to thank the Graduate School of MAINZ (funded through the Excellence Initiative DFG/GSC266). In particular, many thanks to all people involved in the coordiation office.

Many thanks to [redacted] and [redacted]. I will never forget the time we have spent together in Santa Barbara and Mainz. Thank you, [redacted], [redacted] and all the other Santa Barbarians for the amazing time in Santa Barbara. The time I spent in paradise really broadened my horizon.

To all the friends and colleagues in the Tremel group I want to say thank you for being a lot of fun. You supported me during the last three years and made all this possible - I will never forget the nights we spent out partying, the several hikes we did and - of course - the "Fastnachtsumzuege".

Abstract

This work has investigated the thermoelectric properties of tungsten Magnéli oxides and sinterend $FeSb_2$ nanoparticles, and has revealed that complex oxides (such as the Magnéli phases) are promising thermoelectric materials.

The conventional approach in finding thermoelectrics is to empirically search for materials with large α, small ρ and small κ thereby increasing the thermoelectric figure of merit, $zT = \left(\alpha^2/\rho\kappa\right) \cdot T$. Optimizing such a relationship quickly reduces the space of available materials, and it is well known that all good thermoelectrics are small-band-gap semiconductors or semi-metals. There has been renewed interest in the field of thermoelectrics after recent predictions that crystalline interfaces can lead to lower thermal conductivity and thus higher thermoelectric performance.

The main focus of this thesis lies on the thermoelectric characterization of tungsten Magnéli oxides. The combination of crystallographic shear planes, a large unit cell, and a metal-like electrical conductivity make tungsten Magnéli oxides promising candidates for high-performance thermoelectric materials. In this proof of principle study, $WO_{2.90}$ and $WO_{2.722}$ were prepared by classic solid state reaction and yielding single phase materials. SPS was used to consolidate the materials and produce dense, single phase pellets. For $WO_{2.90}$, {103} crystallographic shear planes have been identified by structure determination, whereas pentagonal columns are the dominating structural feature in $WO_{2.722}$. The obtained thermal conductivities are $\kappa = 3\text{-}3.5\,\mathrm{W\,m^{-1}\,K^{-1}}$ ($WO_{2.90}$) and $\kappa = 9\text{-}6\,\mathrm{W\,m^{-1}\,K^{-1}}$ ($WO_{2.722}$). The differences are mainly ascribed to crystallographic shear planes, which act as scattering centers for phonons. The thermal conductivity of $WO_{2.90}$ is comparable to current *n*-type oxide state of the art materials. The obtained figure of merits are 0.13 ($WO_{2.90}$) and 0.07 ($WO_{2.722}$) at 1100 K, which are promising.

A rapid SPS-assisted preparation of dense and single phase $WO_{2.90}$ pellets has been elaborated, allowing the simultaneous preparation and consolidation of $WO_{2.90}$ starting from commercially available precursors, WO_3 and W. Although the thermal conductivity of these prepared pellets is $\approx 15\%$ higher than in conventionally processed $WO_{2.90}$, the zT of 0.1 is still comparable to convetionally processed $WO_{2.90}$.

This work also demonstrates the SPS-assisted approach can be used for the introduction of additional scattering centers on the nanoscale. By adding small amounts of Ta_2O_5, the lattice thermal conductivity of $WO_{2.90}$ decreases steadily with the introduction of (W)-Ta-O scattering centers. Additionally, HRTEM studies reveal dislocations, oxygen vacancies and Wadsley-defects in the pellets, which also contribute to a low thermal conductivity. Similar to recent breakthroughs, scattering centers on the atom scale (defects) and the nano scale (nanoinclusions) lead to an improvement of the lattice thermal conductivity and values of $\kappa_{lat.} = 2\,\mathrm{W\,m^{-1}\,K^{-1}}$ are observed. This leads to an enhancement of the zT of $\approx 50\%$ to 0.15 at 1100 K.

Through the rapid sample preparation method developed in this work high-throughput exploration of new phases may help playing a key role in understanding the underlying physics in Magnéli oxides and related complex materials.

In addition to the investigation of complex oxides, the more conventional approach was pursued in $FeSb_2$ to increase its thermoelectric performance by introduction of crystalline interfaces on the nanoscale.

Nanoparticular $FeSb_2$ was prepared *via* a new, facile wet chemistry approach which is also suitable for the preparation of other binary antimonides such as CoSb, NiSb, Cu_2Sb, ZnSb and Zn_4Sb_3. $FeSb_2$ is an important material of considerable interest due to the recent discoveries of a colossal Seebeck effect of -42000 $\mu V\,K^{-1}$ at 10 K.

However, the application of $FeSb_2$ thus far has been limited because of its high thermal conductivity. The nanoparticles prepared in this work were consolidated using SPS, which does not lead to significant particle growth. Transport measurements show that the thermal conductivity is reduced about 80% with respect to the bulk value. However, an improvement of the figure of merit is not gained due to a reduction of the thermopower, which is caused by a collapsse of the correlation effects in the nanoparticles. These results underline the challenge in thermoelectrics to overcome the interrelation of the different material properties, the decrease of the thermal conductivity while maintaining the high thermopower.

Abstract - German

Diese Arbeit beschäftigt sich mit dem Einfluss von intrinsischen Nanostrukturen und Korngrenzen auf die thermische Leitfähigkeit von Festkörpern. In diesem Zusammenhang werden die thermoelektrischen Eigenschaften von Wolfram Magnéli Phasen und gesinterten $FeSb_2$ Nanopartikel untersucht.

Der gewöhnliche Weg Materialien mit guten thermoelektrischen Eigenschaften zu finden ist die empirische Suche nach Materialien mit hohem Seebeck Koeffizienten, hoher elektrischer Leitfähigkeit und geringer thermischer Leitfähigkeit um den thermoelektrischen Gütefaktor, $zT = \left(\alpha^2/\rho\kappa\right) \cdot T$ zu maximieren. Die Bedingungen des Gütefaktors grenzen die Auswahl an möglichen Materialien schnell ein, und stark dotierte Halbleiter stellen aktuell die state-of-the-art Materialien dar.

Der Fokus der Arbeit liegt auf der Charakterisierung der thermoelektrischen Eigenschaften von Wolfram Magnéli Phasen. Die Kombination aus kristallographischen Scherebenen, einer großen primitiven Einheitszelle, einer hohen Defektdichte gepaart mit einer metallartigen elektrischen Leitfähigkeit machen diese Verbindungsklasse zu vielversprechenden Kandidaten für die thermoelektrische Anwendung.

Zunächst wurden die Verbindungen $WO_{2.90}$ und $WO_{2.722}$ mittels Festkörpersynthese dargestellt. Die Pulver wurden per Spark Plasma Sintering (SPS) kompaktiert und anschließende Mikrostrukturuntersuchungen zeigen dichte, homogene Pellets. Während $WO_{2.90}$ eine {103} kristallographische Scherebene besitzt welche als intrinsische Nanostruktur interpretiert werden kann, sind in $WO_{2.722}$ pentagonale Tunnel das dominierende Strukturmotiv. Die gemessenen thermischen Leitfähigkeiten sind im Bereich von κ= 3-3.5 $\mathrm{W\,m^{-1}\,K^{-1}}$ ($WO_{2.90}$) und κ = 9-6 $\mathrm{W\,m^{-1}\,K^{-1}}$ ($WO_{2.722}$). Der Unterschied in den thermischen Leitfähigkeiten ist hauptsächlich durch kristallographische Scherebenen in $WO_{2.90}$ zu erklären, welche als Phononenstreuzentren wirken. Die thermische Leitfähigkeit ist etwas geringer als für derzeitige *n*-typ oxidische state-of-the-art Materialien. Die erhaltenen Gütefaktoren sind mit 0.13 ($WO_{2.90}$) und 0.07 $WO_{2.722}$ vielversprechend.

Aufbauend auf diesen Ergebnissen wurde eine SPS unterstützte Preparation von $WO_{2.90}$-Pellets entwickelt, ausgehend von kommerziell erhältlichem WO_3 und W. Obwohl die thermische Leitfähigkeit dieser Proben $\approx$15% höher ist als konventionell hergestellte Pellets aus $WO_{2.90}$, ist der Gütefaktor mit $zT = 0.1$ vergleichbar. Damit erlaubt die SPS unterstützte Präparation die Synthese und gleichzeitige Präparation von Pellets ohne weiteren Kompaktierungsschritt und kann in Zukunft maßgeblich zur systematischen Untersuchung der Struktur--Eigenschafts-Beziehungen in komplexen Oxiden und Magnéli Phasen beitragen.

Folgend wurde die entwickelte SPS-unterstützte Präparation verwendet um zusätzliche Streuzentren für Phononen einzuführen. Durch Zugabe von wenigen Prozent Ta_2O_5, konnte der Gitteranteil der thermischen Leitfähigkeit verringert werden, ohne die elektronischen Eigenschaften zu beeinflussen. HRTEM Untersuchungen zeigen neben (W)-Ta-O Streuzentren eine höhere Anzahl an Versetzungen, Sauerstoff-Fehlstellen und Wadsley-Defekten welche ebenfalls zur verringerten thermischen Leitfähigkeit beitragen. Ähnlich zu kürzlich publizierten Durchbrüchen, wirken demnach Streuzentren jeder Grössenskala (atom-, nano-) als

Streuzentren für Phononen, was zu thermischen Gitterleitfähigkeiten von $\kappa_{lat.} = 2\,\mathrm{W\,m^{-1}\,K^{-1}}$ führt.

Die thermoelektrischen Gütefaktoren konnten damit um 50% auf einen Wert von $zT = 0.15$ bei 1100 K erhöht werden.

Zusätzlich zu der Untersuchung von Magnéli Phasen wurde der Einfluss von kristallinen Grenzflächen im Nanometerbereich auf die thermische Leitfähigkeit an kompaktierten $FeSb_2$ Nanopartikeln untersucht. Aufgrund des publizierten Seebeck Koeffizienten von -42000 $\mu\mathrm{V\,K^{-1}}$ bei 10 K zog $FeSb_2$ in den letzten Jahren viel Aufmerksamkeit auf sich.

In diesem Kontext wurde eine nasschemische Syntheseroute für die Darstellung von $FeSb_2$ Nanopartikel entwickelt, welche sich auch zur Synthese weiterer nanopartikulärer Übergangsmetallantimoniden wie z.B. CoSb, NiSb, Cu_2Sb, ZnSb und Zn_4Sb_3 eignet.

Die dargestellten $FeSb_2$ Nanopartikel wurden mittels SPS kompaktiert. Aufgrund der sehr hohen Heiz- und Abkühlraten ermöglicht SPS die Kompaktierung von Nanopartikeln ohne Kornwachstum. Die thermische Leitfähigkeit konnte bis zu 80% im Vergleich zu Einkristallen verringert werden, wobei der Hauptanteil der Reduktion auf Phononenstreuung an den Korngrenzen zurückzuführen ist. Eine Verbesserung des thermoelektrischen Gütefaktors konnte aufgrund des geringeren Seebeck Koeffizienten nicht erreicht werden. Elektronenkorrelation welche in einkristallinem- und bulk-$FeSb_2$ für den hohen Seebeck Koeffizienten verantwortlich ist, wird in Nanopartikeln weitestgehend unterdrückt.

Diese Ergebnisse unterstreichen die anspruchsvolle Aufgabenstellung im Forschungsfeld der Thermoelektrik die miteinander verknüpften Materialeigenschaften unabhängig voneinander zu optimieren.

Contents

List of Figures

List of Tables

List of symbols and notations

α	Seebeck coefficient (thermopower)
CS	crystallographic shear
CAPAD	current activated and pressure assisted densification
DSC	differential scanning calorimetry
d	density
DC	direct current
C_{AB}	spring constant between atom A and atom B
E	electric field
F	Faraday constant, $9.6586 \cdot 10^4\,\mathrm{C\,mol^{-1}}$
D_i	diffusivitiy
η	efficiency
η_C	Carnot efficiency
η_T	thermogenerator efficiency
$\hbar$	Planck's constant, $6.6261 \cdot 10^{-34}\,\mathrm{m^2\,kg\,s^{-1}}$
HP	hot press
HRTEM	high resolution transmission electron microscopy
I	electric current
J	current density
j	j-th phonon branch
κ	thermal conductivity
$\kappa_{el.}$	electronic part of the thermal conductivity
$\kappa_{lat.}$	lattice part of the thermal conductivity
LED	light emitting diode
L	Lorenz number, $2.44 \cdot 10^{-8}\,\mathrm{W\,\Omega\,K^{-2}}$
l	phonon mean free path
M	atomic mass
μ_T	Thomson coefficient
N	atom number
PXRD	powder x-ray diffraction
ω	vibrational frequency
q	phonon wave vector
Q	thermal current density
dq_p	Peltier heat
dq_T	Thomson heat
Π_x	Peltier coefficient of material x

PF	power-factor ($\alpha^2\sigma$)
ρ	electrical resistivity
σ	electrical conductivity
SPS	spark plasma sintering
SEM	scanning electron microscopy
T	absolute temperature
T_D	Debye temperature
TG	thermogravimetry
TOA	trioctylamine
TEG	tetraethylene glycol
τ_{EP}	scattering relaxation time for electron-phonon scattering
τ_{GB}	scattering relaxation time for grain-boundary scattering
τ_N	scattering relaxation time for normal scattering
τ_{PD}	scattering relaxation time for point defect scattering
τ_U	scattering relaxation time for Umklapp scattering
ν_g	phonon group velocity
$\langle n \rangle$	phonon number
$\langle n \rangle^{eq.}$	phonon number in equilibrium
V	voltage
V	volume
z	piston position
zT	thermoelectric figure of merit

1 Introduction

Diminishing fossil fuel ressources combined with the increasing demand for energy will become a major challenge not only for our society, but also for future generations. In this context, renewable energy technologies play a key role and therefore plenty of effort has been devoted over the past years in the development of more efficient materials for photovoltaics, water splitting, light emitting diodes, batteries and thermoelectrics. In particular since German nuclear power plants will be decommissioned, new and sustainable energy sources are required.

Thermoelectric generators which are able to convert heat energy into electric energy can help to face this challenge by increasing the efficiency of certain processes such as in industrial plants, cars or even in solar cells. Although thermoelectric materials are already used in spacecraft, the performance needs to be increased for commercial application.

The conventional approach to finding thermoelectrics is to empirically search for materials with suitable electronic and thermal properties which reduces the space of available materials. The approach pursued in this work is to investigate materials with low intrinsic thermal conductivities.

1.1 Summary

This chapter provides a substantial introduction into the topic covered within this thesis.

At the beginning the thermoelectric phenomenon will be discussed and the upcoming challenges in this research field will be outlined. Afterwards heat transport in the solid state will be treated from a qualitative point of view which directly leads to requirements towards a good thermoelectric.

A rough review on properties of tungsten based Magnéli phases will be given and the properties will be compared to those required for a good thermoelectric material.

At the end, spark plasma sintering will be presented which was used as consolidation method for all materials investigated in this thesis.

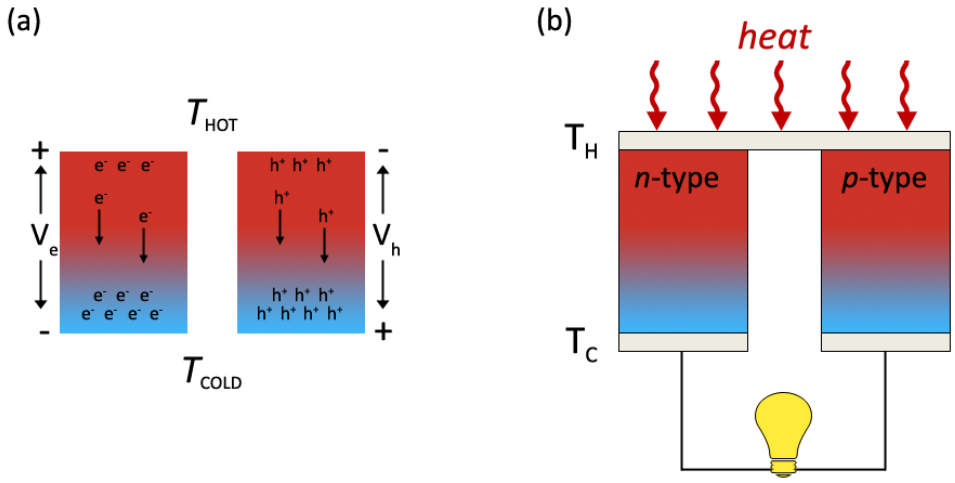

Figure 1.1: Schematic of **(a)** the Seebeck effect and **(b)** a thermogenerator which is used to convert heat energy into usable electrical energy. Due to the temperature gradient the charge carriers (e^- and h^+) diffuse to the cold end until the equilbrium between chemical potential and the electrostatic repulsion is reached.

1.2 Thermoelectrics

The thermoelectric phenomenon allows for the conversion of heat energy into usable, electric energy and *vice versa*. Motivated by theoretical studies which showed that crystalline interfaces on the nanoscale reduce the thermal conductivity of a material, a lot of effort has been devoted in optimizing materials for thermoelectric application.[1] Due to the rising interest, a couple of stimulating review papers appeared and therefore, just a brief introduction is presented here.[2–4]

1.2.1 Basic theory

In 1821 *J.T. Seebeck* discovered that a compass needle is deflected when a temperature gradient is applied to a loop formed by two metals joined in two places. At this point he did not realize that an electric current is involved and called the phenomenon the thermomagnetic effect.[5–7] *H. C. Oersted* corrected the mistake and coined the term *thermoelectricity*.

Due to the applied temperature gradient a diffusion of charge carriers is caused from the hot to cold end of the material. The diffusion continues until the equilibrium between the chemical potential and electrostatic repulsion is reached. In the equilibrium state, the material is charged, as illustrated in Fig. 1.1(a). For small temperature differences the arising voltage is linearly dependent on the temperature gradient applied,

$$V = \alpha \Delta T \tag{1.1}$$

with V the voltage, α the Seebeck coefficient (thermopower) and ΔT the temperature difference applied, respectively. Depending on the nature of the charge carriers, the Seebeck effect is negative (electron conduction) or positive (hole conduction).[5] For the measurement of

the Seebeck voltage the material must be in contact with another material (closed circuit conditions).

Note at this point that the thermoelectric current also occurs under open circuit conditions, which is a common misconception in literature.

The Seebeck effect is utilized in a so-called thermogenerator, cf. Fig. 1.1(b) where p-type and n-type materials are wired electrically in series and thermally in parallel. Radiosotope thermogenerators are already used in spacecraft where Pu^{239} acts as heat source.[8, 9] However, for commercial application the efficiency of such devices is still not sufficient.

Applying an electric current on a junction of two materials causes heating or cooling, depending on the direction of the current.[6] This effect is called the Peltier effect, after *J.P. Peltier*. The dissipated heat is proportional to the current,

$$dq_p = (\Pi_A - \Pi_B)\ I = \Pi_{AB}\, I \tag{1.2}$$

with dq_p the Peltier heat, $\Pi_A(\Pi_B)$ the Peltier coefficient of material A(B) and I the electric current from A to B. Peltier elements (corresponding devices to thermogenerators) are widely used in temperature regulation, e.g. in optics, X-ray detectors and seat warmers/coolers. Both the Seebeck effect and the Peltier effect are thermodynamically reversible processes and should not be confused with irreversible Joule heating, eq. 1.19.

The third thermoelectric effect was found by *W. Thomson* in 1854, who postulated a connection between the Seebeck effect and Peltier effect. He applied the second law of thermodynamics and discovered an experimental inconsistency. Considering a conductor where a temperature gradient is applied, he supposed that an electrical current causes a Thomson heat dq_T:

$$dq_T = \mu_T J \nabla T, \tag{1.3}$$

with μ_T the Thomson coefficient, J the current density.

From this qualitative point of view, a good thermoelectric material requires (i) a low thermal conductivity to keep the temperature gradient stable, (ii) a good electrical conductivity to assure charge carrier diffusion and (iii) a high Seebeck coefficient. However, all these parameters are interrelated and the main task in thermoelectric research is to overcome this interrelation.[10]

1.2.2 Thermoelectric figure of merit, zT

A thermogenerator is a heat engine which converts heat energy into usable electric energy. Therefore, the efficiency is connected to the Carnot process,[11]

$$\eta = \frac{W}{Q_H} = \eta_C \cdot \eta_T = \eta_C \cdot \frac{\sqrt{1+zT}-1}{\sqrt{1+zT}+\frac{T_C}{T_H}}, \tag{1.4}$$

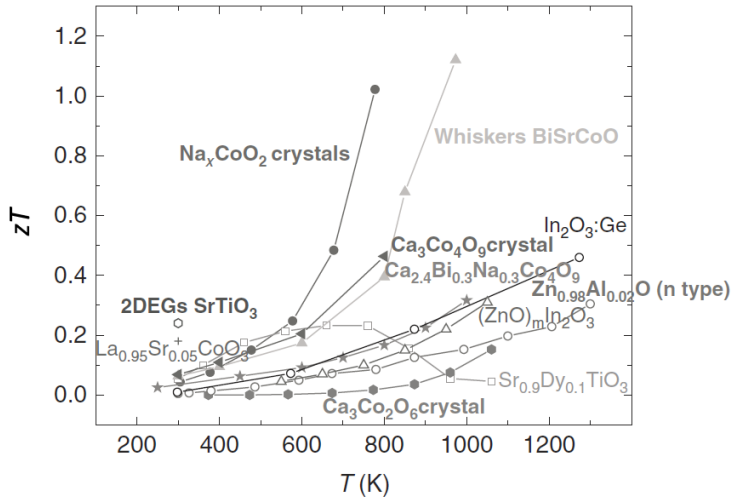

Figure 1.2: Overview of zT values of different oxide materials. Note that depending on the material, the maxium zT is reached at different temperatures.[12]

with W the power generated, Q_H net heat flow, η_C the efficiency of the Carnot process, zT figure of merit, T_C and T_H as the temperature at the cold and the hot side, respectively.[5, 7] In the thermoelectric figure of merit, all the materials properties are included:

$$zT = \frac{\alpha^2 \sigma}{\kappa} \cdot T, \tag{1.5}$$

with σ the electrical conductivity, κ the total thermal conductivity and T the absolute temperature. The zT is a dimensionless quantity of the performance of a certain material and reflects the previously stated requirements for a good thermoelectric material. Increasing a material's zT and therefore the device efficiency has been the challenge in the field of thermoelectric research since the early 60s.

1.2.3 State of the art materials

Current state of the art materials show peak zT values >2, although the cycling stability seems questionable in some cases.[13, 14] Materials such as PbTe, SiGe and Bi_2Te_3 with zT values around 1.5 - 1.8 are well studied compounds and their zT values have been increased significantly over the past decades.[3, 9, 15] The long-time stability of SiGe alloys is proven in the spacecraft mission Voyager II where a SiGe based radioisotope thermogenerator has acted as an as energy source for now more than 30 years.[8] Recently, a PbTe/TAGS based thermogenerator has become popular, installed in the Mars Rover mission "Curiosity"with device efficiencies of 5 %.[9] Other promising materials include Zintl phases, Skutterudites and Half-Heusler compounds, having zT values of $\approx$ 1.5 at temperatures above 400 K.[16–18]

In general, oxide materials have lower zT values and only p-type compounds show zT values greater than one.[19] Usually limited by a high thermal conductivity due to the simple crystal structure, oxides are still of interest because of their inherent chemical and physical stability.[12] An overview of oxide state of the art materials is shown in Fig. 1.2

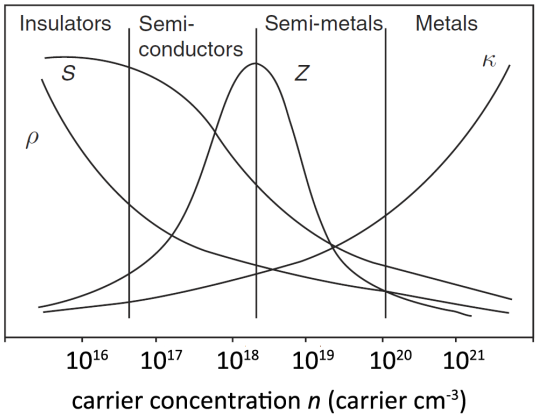

Figure 1.3: Illustrated are the Seebeck coefficient, electrical resistivity, thermal conductivity and z in dependence of the charge carrier concentration

Since the 70s, Na_xCoO_2 and related compounds such as Li_xCoO_2 have been investigated as anode materials for batteries and also exhibit promising thermoelectric properties. The compounds exhibit a layered structure made of edge-shared CoO_6 octahedrons and Na^+ or Li^+ cations between the layers.[20] Thermal conductivities smaller than $2\,W\,m^{-1}\,K^{-1}$ are obtained between 300 K and 800 K, fulfilling the concept of a "phonon-glass electron-crystal".[7] Other *p*-type oxides include structurally related compounds such as $Ce_3Co_4O_9$ misfits and BiSrCoO Whiskers.[21, 22] Recently, p-type oxyselenides (family of BiCuOSe) have drawn the attention due to zT values greater than 1. In contrast to cobalt oxides, oxyselenides seem to be highly stable under ambient conditions.[23]

N-type oxides show significantly lower zT values and the best investigated compound is $Zn_{0.98}Al_{0.02}O$ with a reproducible maxium of 0.4 at 1300 K.[24] Other materials such as the Ruddleson-Popper phases and related compounds exhibit highly interesting properties but the achieved figure of merit is still smaller than 0.3.[19]

So far, there is a big discrepancy between n-type and p-type oxide materials and zT values of oxides are signficiantly lower as current state of the art materials. However, the large variety of conductive oxides, including Magnéli phases which have been barely investigated so far, contain a lot of potential.

In comparison to other state of the art materials which are usually comprised of toxic and scarce elements (e.g. telluride, lead), oxides have smaller zT values, but the high chemical and physical stability combined with the usually low toxicity make oxides to promising candidates for future application in thermoelectrics and material science in general.[22]

1.2.4 Future challenges

The challenge in finding materials with high zT values lies in the interrelation of the material properties, illustrated in Fig. 1.3. Whereas insulators exhibit high Seebeck coefficients, low thermal conductivites and large resistivities, the situation is somewhat reversed for metals. *Slack* et *al.* introduced the concept of a perfect thermoelectric material, a so called "phonon-glass electron-crystal"- the need of glass-like thermal properties and electronic transport prop-

erties of a crystal. This concept is best realized in compounds such as filled Skutterudites, Zn_4Sb_3 and Zintl phases.[25]

A prominent approach to enhance the zT of a promising material is the introduction of crystalline interfaces on every lengthscale. Due to phonon scattering at the grain boundaries, the thermal conductivity can be altered reaching glassy values.

However, other approaches which focus on the optimization of electronic properties include band engneering and the introduction of resonant state levels to gain advantage of the correlation between the Seebeck effect and the slope of the density of states next to the chemical potential.[26]

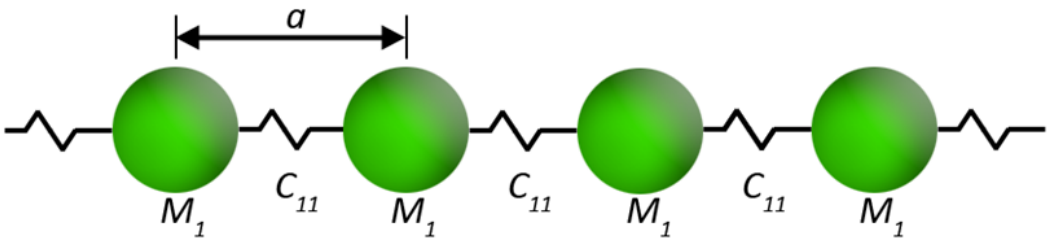

Figure 1.4: Illustration of a monoatomic chain, with one atom in the unit cell and a unit cell length of a. Although this simple model has little in common with a real solid, important relations for the description of $\kappa_{lat.}$ can be derived.

1.3 Thermal transport in the solid state

As stated before, good thermoelectric materials desire small thermal conductivities. In this section basic concepts of thermal transport in the solid state will be introduced and linked to current approaches in the field of thermoelectrics towards low thermal conductivites of promising materials.[3, 27]

Neglecting bipolar contributions the thermal conductivity can be written as the sum of electronic and lattice contributions,

$$\kappa = \kappa_{lat.} + \kappa_{el.} \tag{1.6}$$

with $\kappa_{lat.}$ the lattice part of the thermal conductivity and $\kappa_{el.}$ the electronic part of the thermal conductivity.[28]

This thesis focuses on oxide materials with intrinsic low lattice thermal conductivities, thus, the lattice part $\kappa_{lat.}$ will be stressed here. For a detailed description of the electronic part of the themal conductivity, the reader is referred to comprehensive reviews.[29–31]

1.3.1 The monoatomic and diatomic linear chain

Within the adiabatic approximation introduced by *Born* and *Oppenheimer*, the dynamic of electrons and atomic *nuclei* can be separated which is justified by the large mass difference of atomic *nuclei* and electrons.[32] Although the following model has little in common with a real solid, the monomatic (diatomic) chain is a reasonable starting point which illustrates the situation qualitatively.

In Fig. 1.4, the monoatomic chain with one atom in the unit cell is illustrated. At temperatures $>0\,$K atoms oscillate around their equilibrium positions. In the monoatomic chain the atoms are connected by identical springs and the oscillation is highly coupled to neighboring atoms. Thus, the force constant C_{11} (bond strength) is an important property. By applying Newton's law on the monoatomic chain the dispersion relation for a monoatomic chain can be calculated to be

$$\omega = 2\sqrt{\frac{C_{11}}{M}}\,|sin(qa/2)| \qquad q = \frac{n\pi}{a} \tag{1.7}$$

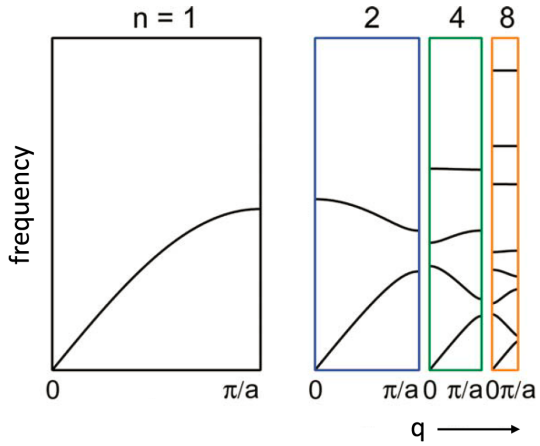

Figure 1.5: Phonon dispersion curve in dependence of the number of atoms in the primitive unit cell. With increasing atom number flat optical branches are introduced in the dispersion curve, which lead to low phonon group velocities. Figure adapted and modified from reference [27].

with ω the vibrational frequency, M the mass of the atom and q the phonon wave vector.[29]. The function is usually illustrated in a phonon dispersion curve where the frequency ω is plotted as function of q, cf. Fig. 1.5 (N = 1), with N the atom number in the unit cell.[27] The vibrational frequency is periodic in $q = \frac{2\pi}{a}$ thus it is sufficient to plot the function between 0 and $\frac{\pi}{a}$.

The branch illustrated for N = 1 is the so called accoustic branch ($\omega(q)$=0 for q=0). Increasing the atom number in the primitive unit cell, by increasing the unit cell length from a' = 2a, leads to a second branch, the so called optical branch, cf. Fig. 1.5 (N = 2, diatomic chain).[33, 34] In general, a phonon dispersion curve has 3 acoustic branches and 3 N- 3 optical branches. Note at this point that "optical" not necessarily imply optical activity, of course, an optic active vibration must be accompanied with a change of the dipole moment.
Another import quantity is the group velocity v_g of the phonons which is defined as the slope of the phonon branches[31]:

$$v_g = \frac{\partial \omega}{\partial q} = a\sqrt{\frac{C_{11}}{M_1}}cos(qa/2) \tag{1.8}$$

Thus, the phonon dispersion increases with increasing force constants and decreasing masses. Although v_g is difficult to access because of the broad spectrum of phonons, v_g directly influences the thermal conductivity which will be shown in the following section.

1.3.2 Lattice thermal conductivity

Thermal conductivity, in general, is a nonequilibrium phenomenon and a thermal current only arises when a temperature gradient is applied. The thermal conductivitiy of a material describes the proportionality of the thermal current density Q and the applied temperature difference[35]:

$$Q = \kappa_{lat.} \nabla T \tag{1.9}$$

Considering small areas with constant temperatures, a phonon number $\langle \mathrm{n} \rangle$ can be defined, using the *canonical distribution*. Neighboring areas will then have different temperatures and the phonon number becomes a function of position. The thermal current density Q, is then expressed in terms of the properties of phonons, here for one direction:

$$Q_x = \frac{1}{V} \sum_{\mathbf{q},j} \hbar\omega \langle n \rangle \nu_x \tag{1.10}$$

Note, in the thermal equilibrium the thermal current density is of course zero. This can be seen directly derived using eq. 1.10. In equilibrium, the phonon numbers $\langle \mathrm{n} \rangle$ are equal for positive and negative values of q and due to the symmetry requirement we have $\nu_x(q) = -\nu_x(-q)$. Therefore a thermal current can only occur when the phonon number $\langle \mathrm{n} \rangle$ deviates from the equilibrium value $\langle \mathrm{n} \rangle^{eq.}$,

$$Q_x = \frac{1}{V} \sum_{\mathbf{q},j} \hbar\omega \left(\langle n \rangle - \langle n \rangle^{eq.} \right) \nu_x \tag{1.11}$$

Now the time variation of phonons can be considered. A change of the phonon number can occur by (i) diffusion of phonons into or out of the observed area and (ii) phonons may decay into other phonons by scattering processes. Using the so called Boltzmann equation[30]:

$$\frac{d\langle n \rangle}{dt} = \left. \frac{\partial \langle n \rangle}{\partial t} \right|_{diff.} + \left. \frac{\partial \langle n \rangle}{\partial t} \right|_{decay}. \tag{1.12}$$

This is a special form of the Boltzmann equation which can also be used for considering problems concerning electron transport. However, assuming steady state conditions, the total time derivative of the phonon number is constant and therefore $d\langle n \rangle / dt$ is zero. Considering the diffusion of phonons in more detail, within a time intervall Δt all the phonons that were originally within the region $x - v_x \delta t$ will arrive in the region of interest around x.

$$\left. \frac{\partial \langle n \rangle}{\partial t} \right|_{diff.} = \lim_{\Delta t \to 0} \frac{1}{\Delta t} \left[\langle n \left(x - \nu_x \Delta t \right) \rangle - \langle n \left(x \right) \rangle \right] = -\nu_x \frac{\partial \langle n \rangle^{eq.}}{\partial T} \frac{\partial T}{\partial x} \tag{1.13}$$

For the decay process, the relaxation time τ is introduced *via*,

$$\left. \frac{\partial \langle n \rangle}{\partial t} \right|_{decay} = \frac{\langle n \rangle - \langle n \rangle^0}{\tau} \tag{1.14}$$

By substitution of eq. 1.14,1.13, 1.12 into eq. 1.11 an expression for the thermal current density in dependence of phonon properties is derived[29, 35].

$$Q_x = -\frac{1}{V} \sum_{\mathbf{q},j} \hbar\omega \left(\mathbf{q}, j \right) \tau \left(\mathbf{q}, j \right) \nu_x^2 \left(\mathbf{q}, j \right) \frac{\partial \langle n \left(\mathbf{q}, j \right) \rangle^{eq.}}{\partial T} \frac{\partial T}{\partial x} \tag{1.15}$$

By a comparison of eq. 1.15 with eq. 1.9 and considering an isotropic system, $\langle v_x^2 \rangle = \frac{1}{3}v^2$ an expression for $\kappa_{lat.}$ is obtained.

$$\kappa_{lat.} = \frac{1}{3V} \sum_{\mathbf{q},j} v\left(\mathbf{q},j\right) \Lambda\left(\mathbf{q},j\right) \frac{\partial}{\partial T} \epsilon\left[\omega\left(\mathbf{q},j\right),T\right], \tag{1.16}$$

with $\partial/\partial T \epsilon\left[\omega\left(\mathbf{q},j\right),T\right]$ the heat capacity of phonon j with wave vector q.

Eq. 1.16 shows the dependence of the thermal conductivity of the group velocity on the different phonons. Phonons close to the zone boundary $(\mathbf{q}) \rightarrow 0, \omega \rightarrow 0$ and optical phonons contribute less to the thermal conductivity. Furthermore, the contribution of the specific heat capacity of every phonon is emphasized.[27, 35] In the Debye approximation (phonon group velocities are approximated as constant), we derive eq. 1.17:

$$\kappa = \frac{1}{3} C v_g l \tag{1.17}$$

This phenomenlogical equation, also holds for gases and electrons. In general, eq. 1.17 is used as an approximation and the frequency dependency of the single parameters is then introduced qualitatively.[31]

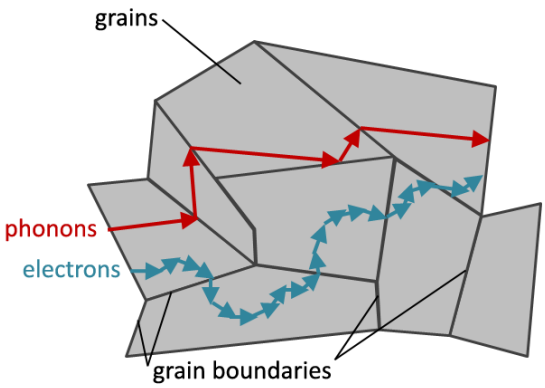

Figure 1.6: Schematic of the differences of the mean free path of phonons and electrons. Whereas the mean free path of phonons is significantly reduced due to scattering at crystalline interfaces, the electrons mean free path is smaller thus the influence of these additional scattering sites is less significant.

1.3.3 Complex unit cell approach

Experiments show that compounds with many atoms in the primitive unit cell usually exhibit low lattice thermal conductivities. This finding can be qualitatively understood within the model of the monoatomic chain, discussed above.[36, 37]

As illustrated in Fig.1.5, doubling the number of atoms in the unit cell means doubling the number of optical branches in the dispersion curve. The optical branches usually exhibit small group velocities, v_g, eq. 1.8. Neglecting interactions between optical and acoustic phonons, this directly leads to a small $\kappa_{lat.}$, cf. eq. 1.17.[31, 38] Interactions between optical- and acoustic phonons are strong for a small phonon gap and weak for a large phonon gap. The size of

the gap strongly depends on the mass difference of the atoms, hence, a large mass difference leads to a large gap between acoustic and optical phonons.[39]

By considering the monoatomic chain, it is easily shown that (i) many atoms in the unit cell and (ii) large mass differences of the atoms lead to low thermal conductivites. Both requirements are fulfilled by tungsten Magnéli oxides.

1.3.4 Grain boundary scattering towards low lattice thermal conductivities

The mean free path of a phonon is the product of the scattering relaxation time τ and ν_g. Before, the influence of the phonon disperson on ν_g was illustrated, now the scattering relaxation time is discussed in more detail.
According to Matthiessen's rule, the relaxation time can be written as the sum of all scattering processes[29],

$$\tau^{-1} = \sum_i \tau^{-1} = \tau_U^{-1} + \tau_{GB}^{-1} + \tau_{PD}^{-1} + \tau_N^{-1} + \tau_{EP}^{-1} \tag{1.18}$$

with the relaxation times of Umklapp phonon-phonon scattering (τ_U), Normal-processes (τ_N), grain-boundary scattering (τ_{GB}), electron-phonon scattering (τ_{EP}) and point-defect scattering (τ_{PD}). Whereas Umklapp phonon-phonon scattering is often the dominating scattering process for temperatures significantly higher than T_D (Debye temperature), electron-phonon interactions and normal-processes can usually be neglected.[27, 31] In the context of this thesis, grain-boundary scattering and point defect scattering have to be discussed in more detail.

An effective approach towards decreased thermal conductivity is the introduction of crystalline interfaces on different lengthscales. These interfaces act as scattering centers for phonons which directly affects τ_{GB}. The electronic conductivity is usually not affected significantly due to the smaller mean free path of electrons, illustrated in Fig.1.6.[1, 4] Already shown for superlattices of Bi_2Te_3-Sb_2Te_3, nanoparticular $CoSb_3$, recently Kanatzidis et al. reported on phonon scattering on different length scales in PbTe leading to a peak zT of 2.2.[14, 15] However, interfaces on the nanoscale tend to grow at high temperatures which challenges the high temperature application.

Another powerful approach to thermal conductivity reduction is the introduction of point defects into the lattice which is usually achieved by alloying with isoelectronic elements. The scattering relaxation time of point defect scattering is influenced by (i) mass differences of the atom (mass field fluctuations), the larger the better and by (ii) differences in the radii (strain field influences) which usually affect the bonding between the atoms.[40] Good examples are the alloying in half-heusler compounds and the void filling in skutterudites.[41, 42]

In conclusion, a good thermoelectric material requires a low lattice thermal conductivity which is usually achieved by compounds with large primitive unit cells and high mass differences of the atoms. In a following step the thermal conductivity can then be optimized by the introduction of scattering centers on different length scales and by alloying.

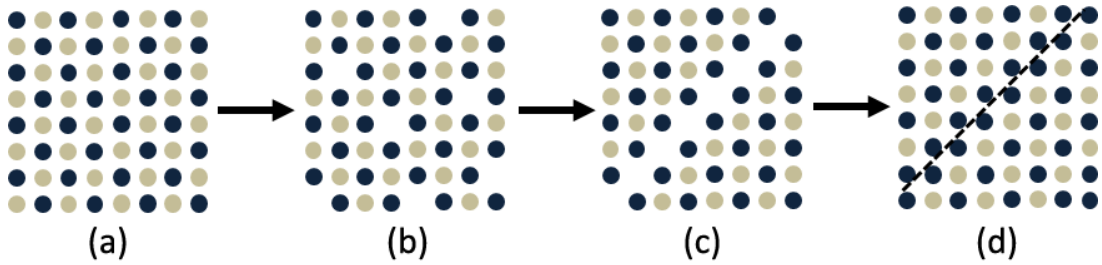

Figure 1.7: Schematic of the formation of crystallographic shear planes. In case of WO_{3-x}, the vacant oxygen sites which are introduced by a slight reduction of the compound tend to diffuse to certain planes within the crystal structure. The condensation process in which edge-sharing octahedras are introduced eliminates the oxygen defects. Concurrently, the oxidation number of W_6^+ central-ions (corner-shared) are partially changed to W^{5+}(edge−shared).

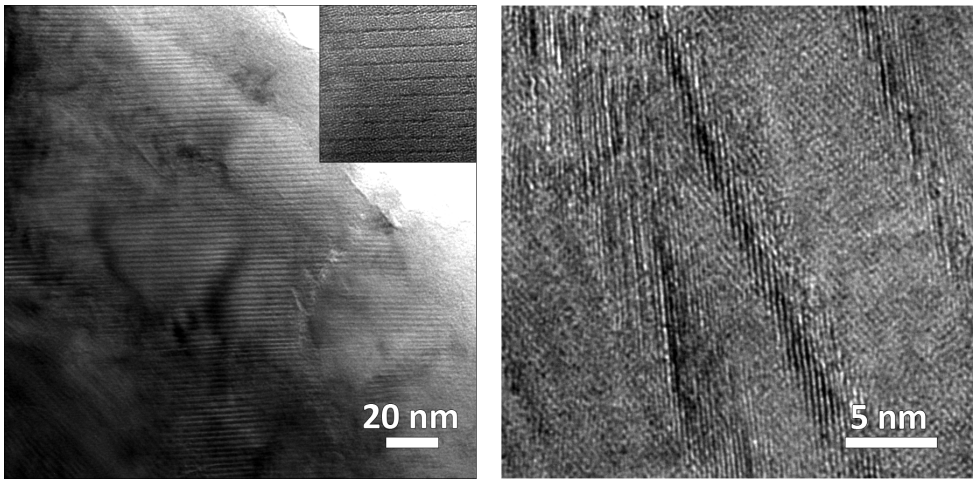

Figure 1.8: Illustrated is the difference between **(a)** CS planes in $WO_{2.90}$ and **(b)** a Wadsley defect. Whereas the CS is a part of the structure and a long-range can be observed, the Wadsley defect is a local phenomenon.

1.4 Tungsten Magnéli oxides

This thesis focuses on the investigations of high temperature transport properties of tungsten based Magnéli oxides. Here, the unique structural features of Magnéli phases are highlighted and the reports about the properties of tungsten Magnéli phases are reviewed.

The structural features will be linked to the requirements for good thermoelectric materials, showing the great potential of Magnéli phases. The determined thermoelectric properties are then presented in Chapters 2, 3, and 4.

1.4.1 Crystallographic shear planes

In 1949 *A. Magnéli* performed extensive structural research on slightly reduced early transition-metal oxides of Ti, V, Nb and W. He found alternating layers of corner- and edge shared octahedras and thereafter, Wadsley established the structural concept of crystallographic shear

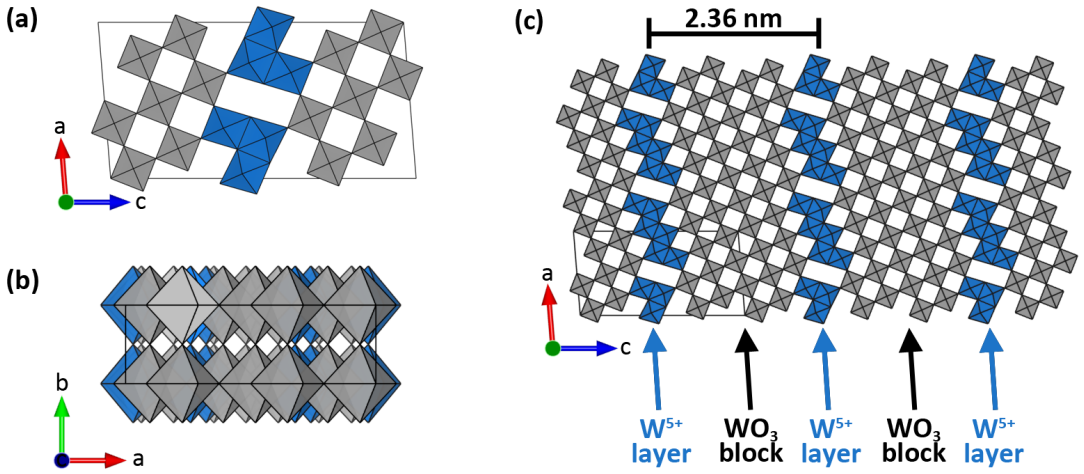

Figure 1.9: Illustrated is the ideal unit cell of $WO_{2.90}$ ($W_{20}O_{58}$) in **(a)** 010 direction and **(b)** 001 direction, respectively. **(c)** illustrates the superlattice structure which originates in the occuring crystallographic shear planes. The structure can be interpreted as 2D structure where WO_3 building blocks (light grey) are separated by layers of edge shared octahedrons with W^{5+} as central atoms (blue). The W^{5+} ions are responsible for the n-type conductivity in this compound.

planes, CS.[43–46] In literature, sometimes CS planes are called "(extended) Wadsley defects" which is a common misconception, cf. Fig. 1.8. In the idealized structures, the CS planes are long range ordered and therefore a part of the structure.[47]

In Fig. 1.7 the formation of the CS planes is illustrated. Starting from a perfect crystal **(a)**, oxygen vacancies are introduced either by heating or chemical reduction **(b)**. In the early transition metal oxides, these vacancies tend to diffuse to certain crystallographic planes to form ordered defects **(c)**. The vacancies are then eliminated by the introduction of corner-sharing octahedras. Similar ordering processes of vacant oxygen sites can be observed in $Fe_{1-x}S$ and $Fe_{1-x}O$ where ordering with maximum seperation and clusters can be found.[48, 49] All these structural changes can be interpreted as assimilation of defects to incorporate them as new structural elements.

CS planes have been widely studied in solid state chemistry, in particular in the 70s and 80s when electron diffraction techniques became more common.[50] In the quasi binary system WO_3 - WO_2, {102} and {103} crystallographic shear planes have been identified by structural determination techniques.[43, 51] A variety of different, non-equilibrium compounds have been identified *via* electron diffraction: {102} CS planes (ordered and disordered), {103} CS planes (ordered and disordered) and the combination of {103} and {102} planes.[52, 53]

A more fundamental study was conducted by Booth et al. who summarized all structural reports and tried to prepare equilibrium phases of the tungsten suboxides.[51] He found four different regions in the phase diagram of WO_3 - WO_2 system: (i) Defect WO_{3-x} with disordered and ordered {102} CS, (ii) a phase region around the formal composition of $WO_{2.90}$ where only {103} CS planes are found (iii) a smaller phase region around $WO_{2.833}$ with disordered pentagonal columns and (iv) a strictly stoichiometric phase $WO_{2.722}$.

In Fig. 1.9(c) the structure of $WO_{2.90}$ is illustrated. As a consequence of the {103} CS planes with a separation of 2.36 nm the structure can be interpreted as a superlattice structure.

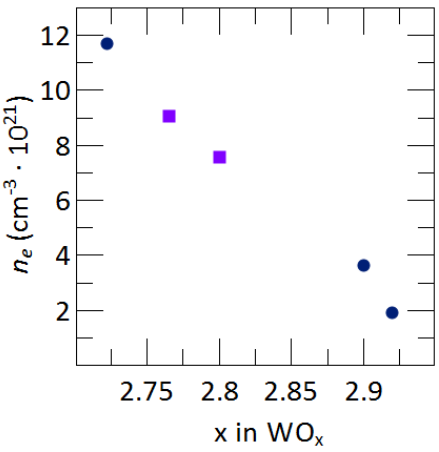

Figure 1.10: Calculated carrier concentrations for the tungsten suboxides WO_x. As expected, with increasing degree of reduction the carrier concentration increases linearly. Data from ref.[54]. Purple data points represent nonequilibrium compounds.

1.4.2 Electrical conductivity in Magnéli phases

A good thermoelectric material requires an electrical conductivity in the order of a heavily doped semiconductor with typical carrier concentration of $\approx 10^{19}$-10^{21} carriers cm^{-3}.

In Magnéli oxides, electrical conductivity occur due to the mixed valence of tungsten and the one electron remaining at the W^{5+} sites. One could expect a temperature activated electrical conductivity similar to a hopping mechanism. However, such a behavior is not observed which suggests that electrical conductivity mainly occurs along the $W^{5+}O_6$ layers in the compounds.

$WO_{2.90}$ has been identified as a promising candidate for thermoelectric application and in this thesis the high temperature properties of $WO_{2.90}$ are determined.[55] As illustrated in Fig. 1.9, the W^{5+} ions form layers in which conduction can occur. For more reduced oxides, metal like behavior is expected, for less reduced oxides, more insulting properties are expected which is in agreement with calculated carrier densities, cf. Fig.1.10.[54]

1.4.3 State of the art: thermoelectric properties of Magnéli phases

So far, no high temperature properties neither on electrical transport nor thermal transport have been reported on tungsten Magnéli oxides. However, room temperature and low temperature electrical conductivity show increasing conductivity with increasing degree of reduction.[56–58] It can be assumed that $WO_{2.90}$ is a heavily doped semiconductor whereas $WO_{2.722}$ has a metal-like electrical conductivity. These results are supported by carrier concentration calculations, which show a linearly increasing amount of carriers with reduction, cf. Fig.1.10.

The room temperature Seebeck coefficients with 16 μ V K^{-1} ($WO_{2.722}$) and 35 μ V K^{-1} ($WO_{2.90}$) further confirm the metal-like conductivitiy of $WO_{2.722}$ and the more semiconducting behavior of $WO_{2.90}$.

High temperature thermoelectric investigations on titanium based Magnéli oxides revealed *n*-type conduction and a reduced thermal conductivity with increasing amount of shear structures in the TiO_{2-x} system.[59] The authors were able to show that CS planes act as sources for phonon scattering without affecting the electronic conduction and zT values of ≈ 0.1 at 1000 K have been reached. Therefore, Magnéli compounds seems very promising to us and are potential candidates to close the current gap between *n*-type and *p*-type oxide thermoelectrics.

In conclusion tungsten Magnéli oxides with their large unit cells fulfill many requirements for compounds with low thermal conductivities. Because of its semiconducting behavior, $WO_{2.90}$ is identified as a promising candidate for thermoelectric application. The tungsten based Magnéli oxide combines an intrinsic nanostructure, a large primitive unit cell with an electrical conductivity comparable to a heavily doped semiconductor.

The intrinsic nanostructure acts as a scattering center for phonons while the large unit cell shall be responsible for low phonon group velocities. The conductivity is comparable to a heavily doped semiconductor, making this compound and Magnéli phases in general highly interesting for thermoelectric research. However, so far, high temperature investigations have not been conducted and proof of principle studies are necessary to verify these expectations.

Figure 1.11: In the field of thermoelectrics the convential processing can be divided into three parts, **(i)** the preparation of the powder, **(ii)** the densification into pellets and the subsequent **(iii)** characterization. In case of nanoparticular compounds the preparation and the consolidation step are exceptionally challenging.

1.5 Spark Plasma Sintering (SPS)

The conventional processing steps in the field of thermoelectrics can be divided into three main parts, illustrated in Fig. 1.11. After the preparation, the material needs to be consolidated in order to perform transport measurements. Depending on the material, the preparation can be challenging, e.g. the characterization of materials that include intermetallic nanoparticles is usually connected with some inaccuracies.[60, 61]

In this section the consolidation step is highlighted and a brief introduction into the technique of spark plasma sintering is provided which is used as consolidation technique for all materials described in this thesis.

In general, two widely known techniques can be applied for consolidation, conventional hot pressing (HP) and spark plasma sintering (SPS), sometimes denoted as current activated and pressure assisted densification (CAPAD).[62–64] Driven by efforts in the research field of nanoparticles, SPS has recently gained much interested. [1, 65, 66] SPS has been shown to be a suitable tool for the consolidation of nanoparticles, due to its ability to maintain their small size.[67, 68] Note at this point, it has been shown that plasma is absent in the SPS process, however, owing to the high recognition value in the community SPS is used as a label in this work.[63, 69]

SPS is a current- (field) and pressure assisted densification method which allows rapid heating and cooling rates (>100 $\mathrm{K\,min^{-1}}$), short holding times and the preparation of dense samples at sintering temperatures of several hundred degrees lower than conventional HP. Instead of using an external heat source (as in conventional HP), an electrical current (DC, pulsed DC) is passed through the conducting pressure die and/or through the sample. The heat is the result of the passed current in the form of Joule heat, eq. 1.19.

$$P = JE, \tag{1.19}$$

with P the power (energy per unit time), J the current density and E the electric field. Although the main densification occurs due to the interplay of temperature and applied pressure, the passed current has nonthermal benefits and generally speaking current promotes densification.[64, 70]

Usually high quality graphite is used as a die material, illustrated in Fig. 1.12. It has been

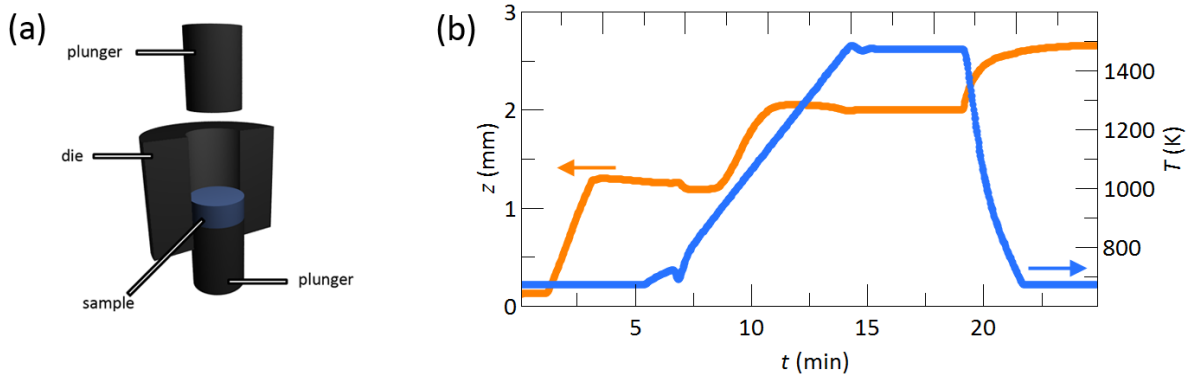

Figure 1.12: **(a)** illustrates a carbon die which is commonly used in SPS and conventional hot pressing processes. **(b)** shows an example of a sintering profile typically obtained during the sintering process with the time dependent piston position z and the absolute temperature T.

shown that SPS can be used for the preparation and simultaneous densification of materials, starting from commercially available precursors which will be emphasized in Chapter 3.[71–73] The single-step preparation of a dense pellet makes this technique interesting for a widespread application, especially for industry, where a single-step preparation is desired.

New SPS devices provide the opportunity of live monitoring sintering parameters such as applied pressure, pyrometer temperature and piston position and a typical sintering profile is shown in Fig. 1.12(b) where the observed temperature and piston position are plotted as function of time. The sintering profile is an important tool to obtain the ideal sintering parameters which have to be carried out for each material. Usually, the goal is densification within a short time period and at temperatures as low as possible. Therefore, in a first sintering experiment of a new material, consolidation is conducted at temperatures $\approx 150\,\mathrm{K}$ below the decomposition temperature. Afterwards, the main consolidation step is identified in the corresponding sintering profile (cf. 1.12(b), $\approx 1200\,\mathrm{K}$). In a second experiment, sintering is done at temperatures $\approx 50\,\mathrm{K}$ above the main consolidation step with a holding time of 1 min. In general, this procedure is a good guide towards high quality pellets of unknown materials. In case of using SPS as tool for consolidation and simultaneous preparation, the situation is not as easy and the holding must be extended usually.

1.5.1 Mechanisms of densification

In a simple picture, densification refers to the elimination of porosity in a loose powder to form a physically stable, dense pellet. Usually three different mechanisms contribute to densification, (i) plastic deformation, (ii) sintering and (iii) particle rearrangement.[63, 74] Whereas plastic deformation occurs instantaneously when a certain, material-dependent stress is exceeded, sintering and particle deformation include temperature dependent processes.

Sintering generally includes surface minimizing processes and the driving force is the reduction of surface energy. As illustrated in Figure 1.13, different mass transport processes can be regarded but not all contribute to densification of the material. Surface diffusion and evaporation are certainly connected with mass transport, but they do not bring the particle centers

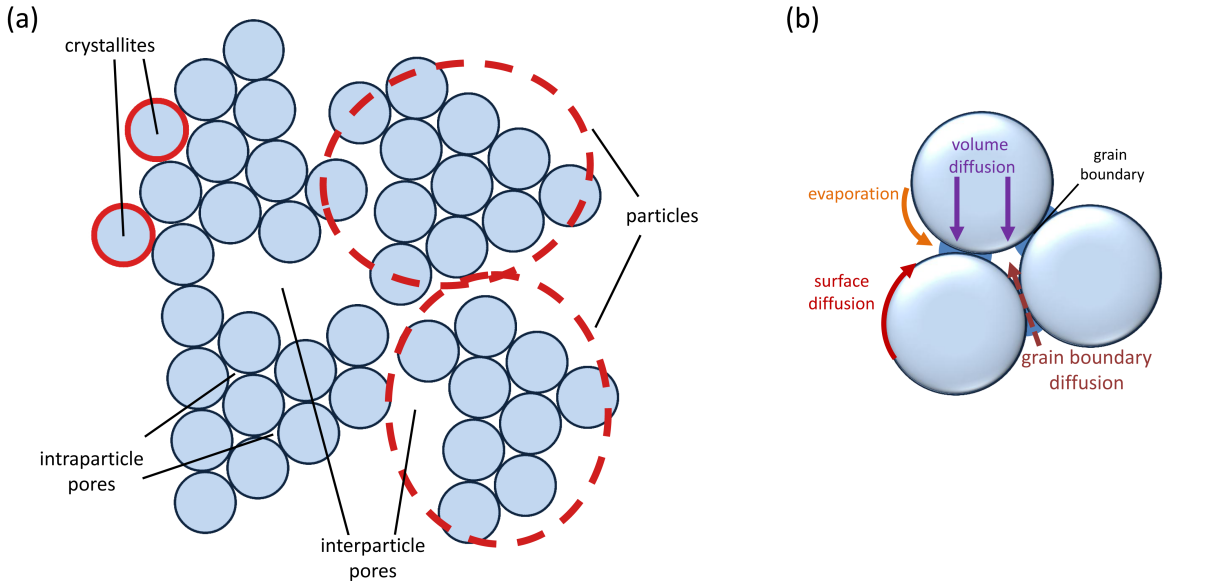

Figure 1.13: (a) illustrates the situation before sintering, highlighting inter- and intraparticle pores. **(b)** Schematic of the underlying processes during sintering. In a qualitative picture, densification can be regarded as competition between sintering and particle growth.

closer together and therefore do not contribute to actual densification. In fact, these processes are mainly responsible for particle growth during consolidation and usually exhibit lower activation energies which makes surface diffusion and evaporation to the dominating mass transport processes in the lower temperature regime. At higher temperatures, grain boundary and volume diffusion are more preferred and particle growth is mainly suppressed.

The second temperature dependent mechanism is particle rearrangement, cf. Fig. 1.13, and is a direct consequence of the applied pressure, however, particle sliding is clearly promoted by grain boundary and/or surface diffusion and is therefore also favored at higher temperatures.

Even this simplified discussion of the underlying densification mechanisms explains why SPS is a suitable tool for the consolidation of nanoparticles thereby maintaining the small size of the particles. The competition of particle growth and densification can be influenced by the large heating rates accessible in the SPS process.

1.5.2 Current effects in SPS

The specific role of the applied current (and corresponding field) highly depends on the nature of the material being investigated. The theory of electromigration which describes the transport of material caused by momentum transfer between conduction electrons and diffusing atoms seems to be a reasonable starting point.[64] The diffusions of the ith species is then described with

$$J_i = -\frac{D_i C_i}{RT}\left[\frac{RT\partial lnC_i}{\partial x} + Fz^* E\right] \tag{1.20}$$

with J_i the flux of the diffusing i-th species, D_i the diffusion coefficient, C_i the conentration, F the Faraday constant, z^* the effective charge of the diffusing species, E the field, R the gas constant and T the absolute temperature, respectively.

However, in a typical SPS experiment the temperature and current are not independent parameters, and therefore thermal effects cannot be separated from the intrinsic role of the current easily. A couple of experiments have been conducted on the formation of intermetallic Al-Au phases, using a three layered geometry (Al-Au-Al) perpendicular to the applied field.[70] The effect of current on growth of the intermetallic phases was then investigated by annealing the layers at 723 K with different current densities. This study shows a remarkable effect of the applied current on the product which supports the formation of the intermetallic phase. However, it is difficult to generalize these results. Even the calculation of the current density which goes through the sample is challenging. It is likely that electromigration effects are active in SPS, but this depends on several parameters, such as the material being processed as well as the stage of densification and the processing parameters employed.

In general SPS is a useful tool not only for the consolidation of a certain material but also for simultaneous preparation and consolidation. The fast heating and cooling rate allow for the consolidation of materials where decomposition and grain growth are known issues during consolidation, e.g. for oxides and nanoparticles. So far, the aimed and systematic SPS-research is somewhat limited due to difficulties in the determination of the current density which passes through the sample.

2 Proof of principle: thermoelectric properties of $WO_{2.90}$ and $WO_{2.722}$

2.1 Summary

This chapter presents the first experimental investigation on the high temperature thermoelectric properties of Magnéli phases $WO_{2.90}$ and $WO_{2.722}$ consolidated *via* SPS. The combination of crystallographic shear planes, a large primitive unit cell and a metal like electrical conductivtiy make Magnéli oxides interesting for thermoelectric application.

Since *A. Magnéli* has discovered crystallographic shear planes in binary M-O systems where M is an early transition metal oxide, a lot of effort has been devoted in the detailed structural investigations of complex oxides. In this context the binary W-O system gained much interest including the compounds $WO_{2.90}$ and $WO_{2.722}$. Whereas {103} crystallographic shear planes have been identified as structure motif in $WO_{2.90}$, the more reduced $WO_{2.722}$ is built of pentagonal tunnels without crystallographic shear planes, cf. Fig. 2.1. Although the carrier concentration slightly differ because of the different degree of reduction, these two compounds are most suitable to investigate the influence of crystallographic shear planes on the thermal conductivity in the W-O system.

For this proof of principle study, $WO_{2.90}$ and $WO_{2.722}$ were prepared *via* solid-state synthesis. The materials were consolidated using SPS and powder X-ray diffraction was used to ensure phase purity. Thermoelectric properties were measured in the temperature regime between 300 K and 1100 K reavealing a significant difference in the thermal conductivity of the compounds.

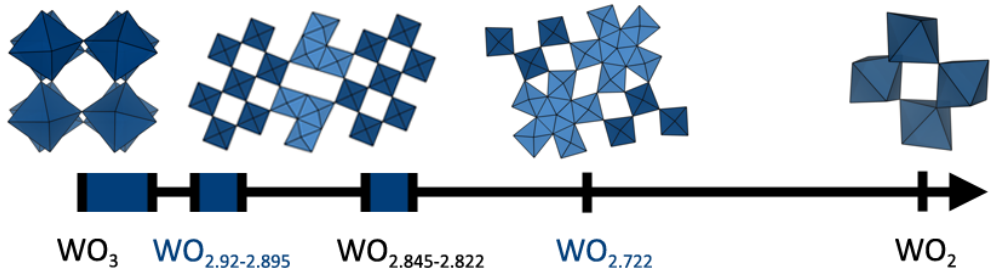

Figure 2.1: Schematic of the WO_3 - WO_2 system and the dominating structure motifs of the different compounds. Not shown are the high-pressure compounds $WO_{2.66}$ and $WO_{2.625}$. The degree of reduction increases from left to right and except $WO_{2.722}$ all compounds exhibit a certain phase width. Illustrated are the distorted ReO_3-type structure of WO_3, crystallographic shear planes which can be found in $WO_{2.92\text{-}2.895}$ and $WO_{2.845\text{-}2822}$. For $WO_{2.722}$ pentagonal tunnels are identified and WO_2 exhibit a distorted TiO_2-type structure.

2.2 Motivation

The results presented here are in parts an adapted reproduction, from *Phys. Chem. Chem. Phys.* 2013, **15**, 15399.[55]

Thermoelectric devices allow for the direct conversion of heat into usable energy and could play a key role in handling the upcoming challenges in the energy sector. Therefore, much effort has been devoted towards designing and improving materials for such devices. It has been shown that interfaces on the nanoscale can enhance the thermoelectric properties by acting as scattering centers for phonons, thereby lowering the thermal conductivity.[7] The use of nanoparticles and artifically superstructures usually involves low yield preparation methods and high cost processes.

Instead of using expensive artificial superstructures and sintered nanoparticles, the concept pursued here is based on an intrinsic, layered nanostructure defined by crystallographic shear planes as structure motifs.[59] Recent studies on structurally related compounds already showed exceptionally low thermal condutivities.[59] As mentioned in the introduction, crystallographic shear planes are a structural feature in reduced early transition metal oxides.

For tungsten oxide, WO_{3-x}, a representative of the Magnéli phases, {102} and {103} crystal shear planes have been identified. Fig. 2.1 shows the idealized unit cell of $WO_{2.90}$ with corner sharing octahedra of the ReO_3-type structure of stoichiometric WO_3 and the crystallographic shear highlighted in light blue.[43, 44, 51] Along the c-axis in $WO_{2.90}$ an intrinsic layered structure with a 2.34 nm separation between adjacent layers have been observed. *Ab initio* calculations showed the possibility of treating $WO_{2.90}$ as an *n*-type degenerate semiconductor, which is also reflected in the low temperature values of the Seebeck coefficient.[54] Although the synthesis of the Magnéli-type tungsten oxides has been reported before, $WO_{2.90}$ is not well investigated. In the synthesis the equilibrium state is usually not achieved, and the crystal structure remains highly disordered.

Monoclinic $WO_{2.722}$ with the largest oxygen deficiency in the WO_3 - WO_2 region is reported as the only oxide that can be isolated in a pure form under ambient condition, which is not the case for other tungsten sub-oxides. The structure of $WO_{2.722}$ contains pentagonal columns (PC) instead of CS, shown in the Fig. 2.1. *Ab initio* calculations predict metallic behaviour, which is in accordance with the higher degree of reduction and the reported temperature dependence of the electrical resistivity.[54] In contrast to $WO_{2.90}$, $WO_{2.722}$ compound is stoichiometric and detailed electron microscopy studies showed the presence of well ordered crystals.[51, 75]

By using bulk compounds with intrinsic nanostructures as thermoelectrics, advantages of bulk phases such as cycling stability and simple preparation are paired with the concept of using crystalline interfaces on the nanoscale to ensure low thermal conductivities.

In case of nanoparticles, the preparation of the desired material and the consolidation has shown to be challenging and remaining solvent molecules on the surface, phase decomoposition, grain growth during densification and low densities are issues which have to be solved for each material very carefully. Therefore, the use of bulk materials with intrinsic nanotructures prepared *via* low cost methods is preferred.

2.3 Procedure and experimental

The approach used here to pellets of $WO_{2.90}$ and $WO_{2.722}$ follows the conventional procedure illustrated in Fig. 1.11. Solid state synthesis was used as preparation method of the powders. After consolidation *via* SPS the obtained pellets were characterized in terms of density, microstructure and transport properties.

Unless stated otherwise, all chemicals were purchased from Sigma-Aldrich with a purity of 99.9 % or higher. For the preparation of $WO_{2.90}$ and $WO_{2.722}$ stoichiometric amounts of W and WO_3 were sealed in evacuated quartz ampules and heated for 24 h at 1323 K ($WO_{2.90}$) and 1073 K ($WO_{2.722}$) with a heating rate of 10 K min^{-1}. After the first heating cycle the powders were thoroughly ground for 10 min and annealed for an additional period of 24 h at the given temperatures. SPS experiments were provided on the SPS - 515 ET, Dr. Sinter - LAB machine (Japan). The materials were ground to a fine powder and loaded into graphite dies with an inner diameter of 8 mm. Carbon foil was used to surround the powder specimen on all sides, isolating the specimen from contact with the graphite die and plungers during SPS experiments. Compaction was achieved following the following temperature protocol: the samples were treated at 1273 K ($WO_{2.90}$) and 1473 K ($WO_{2.722}$) with a heating rate of 100 K min^{-1} under a uniaxial pressure of 50 MPa *in vacuo* and directly cooled to room temperature . These temperatures were held for 1 min; subsequently the samples were cooled to room temperature. For the transport measurements the samples were cut with a diamond wire saw into bar shaped specimens, with typical dimensions of $1.5 \times 1.5 \times 8$ mms.

PXRD was performed with the X-ray Guinier diffraction technique (Huber G670 camera, Cu-$K_{\alpha 1}$ radiation, λ = 0.15409 nm, graphite monochromator. The electrical resistivity and Seebeck coefficient were measured simultaneously in the temperature range from 573 K to 1323 K using a ZEM-3 instrument (ULVAC-RIKO). Specific heat measurements were performed on a Netzsch Pegasus differential scanning calorimeter. The specimens were heated up to 1073 K under Ar atmosphere with a heating rate of 10 K min^{-1}. The thermal diffusivity D was determined in the temperature range from 573 K to 1323 K using the laser flash technique (LFA 447 Micro Flash, Netzsch). The temperature dependent thermal conductivity κ was calculated using the relationship $\kappa = C_p \cdot D \cdot d$, with the geometric density d. For metallographic characterization the SPS specimens were cut perpendicular to the pressure direction. The surface area was prepared by SiC grinding and vibration polishing (VibroMet 2, Buehler) with a 0.05 μm Al_2O_3 slurry. The microstructures were studied by optical microscopy (Axioplan2, Zeiss). Scanning electron microscopy was performed on a Philips XL30 LaB6; EDAX Pheonix system with Si(Li) detector. Carbon-coated specimens were used for SEM analyses.

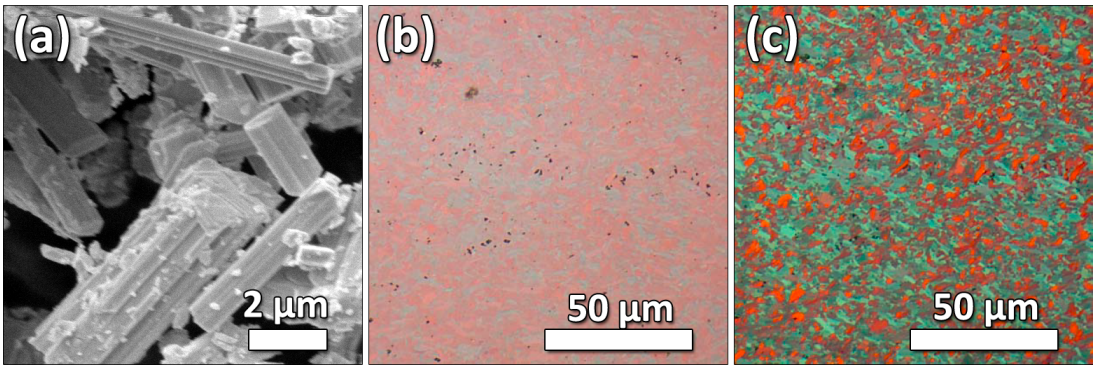

Figure 2.2: Scanning electron micrographs of **(a)** the as prepared $WO_{2.90}$ powder. **(b)** Bright field and **(c)** polarized light images of the sintered pellet show randomly oriented crystallites and a dense sample.

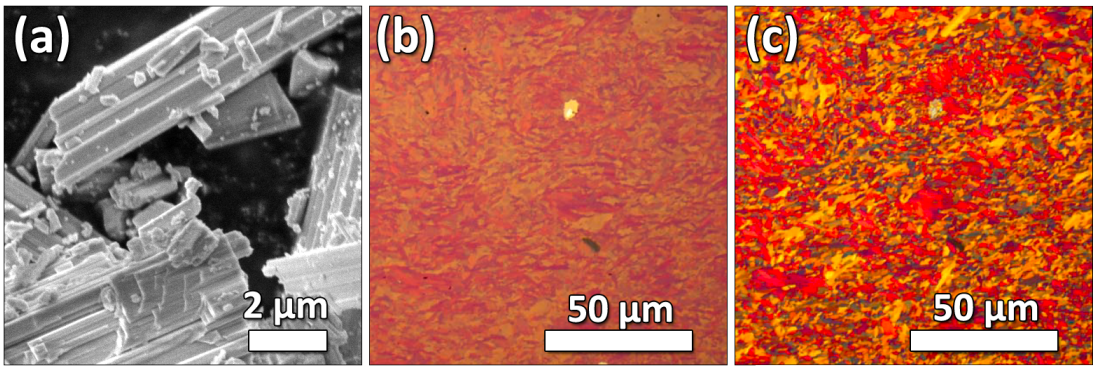

Figure 2.3: Scanning electron micrographs of **(a)** the as prepared $WO_{2.722}$ powder. **(b)** Bright field and **(c)** polarized light images of the sintered pellet show randomly oriented crystallites and a dense sample.

2.4 Results and discussion

2.4.1 Microstructure analysis

The crystallites of both compounds have highly anisotropic morphologies, cf. Fig. 2.2 (a) and 2.3 (a). Spark plasma sintering was used for consolidation, enabling fast heating and cooling rates and minimizing any additional loss of oxygen at higher temperatures which is a well-known effect in oxide chemistry.[47, 64]

Powder X-ray diffraction before and after the sintering process, cf. SI-Fig. 7.1, reveal no phase decomposition or transformation during the sintering process. The lattice parameters for $WO_{2.90}$ (a = 1.208 nm, b = 0.378 nm, c = 2.359 nm) and $WO_{2.722}$ (a = 1.832 nm, b = 0.379 nm, c =1.404 nm) match with those reported in the literature.[51] For $WO_{2.90}$ triclinic WO_3 is taken into account in the Pawley refinement. The amount of WO_3 is around the resolution limit of PXRD, therefore the corresponding features in the powder pattern may also be due to domain structure in the $WO_{2.90}$ crystallites, originating from dislocations of the shear planes.

The sintering process enhances the crystallinity of the materials which is reflected in the calculated crystallite sizes (250 nm for $WO_{2.90}$ and 321 nm for $WO_{2.722}$ and the densities of ≈

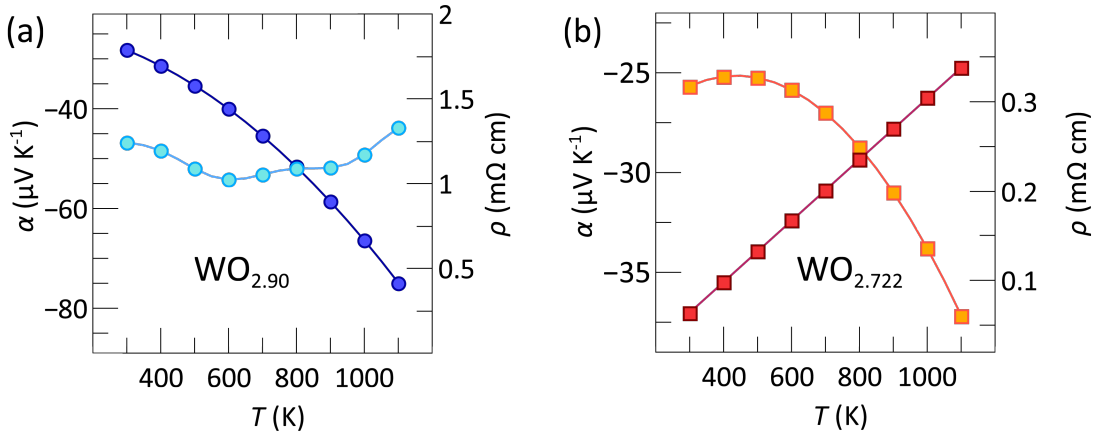

Figure 2.4: Temperature dependence of the thermopower and electrical resistivity of **(a)** $WO_{2.90}$ and **(b)** $WO_{2.722}$. Whereas the electronic transport properties of $WO_{2.90}$ show a temperature behavior of a heavily doped semiconductor, $WO_{2.722}$ exhibit mainly metal-like properties.

100% (7.7 g cm^{-3}, $WO_{2.722}$) and ≈ 98% (6.95 g cm^{-3}, $WO_{2.90}$) [76]. Surface microscopy images of the sintered samples confirm the observed high densities of the pellets and show two different main orientations, indicated by different colors in the polarized-light images.

2.4.2 Electronic transport properties

Temperature dependent Seebeck coefficient and electrical resistivity of both compounds are shown in Fig. 2.4. Both compounds exhibit *n*-type conduction. For $WO_{2.722}$, the electrical resistivity shows a metallic behavior, whereas α features a more complex temperature dependence. $|\alpha|$ first decreases with increasing temperature, passes through a minimum and finally increases monotonically. The reason for the minimum of $|\alpha|$ around 425 K is still unclear, but considering the low temperature data from the literature, $|\alpha|$ passes through the minimum followed by a maximum around 50 K. A similar behaviour, which can be attributed to a charge density wave (CDW), was observed for the structurally related MoO_{3-x} [57, 77]. For $WO_{2.722}$ no evidence for the appearance of a CDW in the electrical conductivity can be found. The absence of a maximum in the high temperature regime indicates that the temperature is not reached, where carriers are excited across the band gap.[28, 78] This would lead to a reduction of the thermoelectric voltage.

For $WO_{2.90}$ the Seebeck coefficient has the expected temperature dependence of a heavily doped semiconductor. The relatively low maximum value of 80 μV K^{-1} at 1000 K can be attributed to a high carrier concentration. The temperature dependence of the electrical resistivity may be explained from a superposition of two different effects.

Band structure calculations for $WO_{2.90}$ show a Fermi surface with hole and electron pockets. In addition, one band lies above but very close to the Fermi level. Therefore thermal excitation of electrons can occur.[29, 31] These electronic features are compatible to the observed metal-like and semiconductor conduction mechanism. With increasing temperature more carriers from defect states close to the unoccupied states of the conduction band are activated leading to a small drop of resistivity. Above a threshold temperature the metal-like

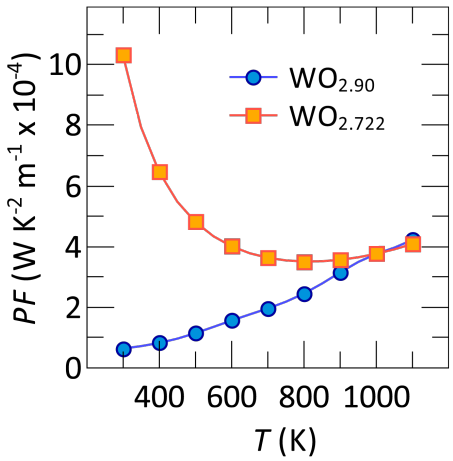

Figure 2.5: Temperature dependence of the power-factor ($\alpha^2\sigma$) of $WO_{2.90}$ (blue) and $WO_{2.722}$ (orange). Above the 850 K both materials show nearly the same values which makes the thermal conductivity the dominating influence for the zT.

behavior becomes dominant and electron-phonon interactions usually play a key role.[35] This leads to a decrease of the electrical conductivity.

Based on the crystal structure and microscope images, one might expect anisotropy contributions to the resistivity. Samples measured in different directions and different diameters showed similar resitivities which indicates that anisotropy effects are not important in polycrystalline sintered samples.

2.4.3 Thermal transport properties

The temperature dependences of the thermal conductivity of $WO_{2.722}$ and $WO_{2.90}$ are shown in Fig. 2.6(a). The lattice parts of the thermal condutivities have not been calculated due to the inherent inaccuracies of the Lorenz number for the WO_{3-x} Magnéli phases, which do not follow the Drude-Sommerfeld model.[79]

The thermal conductivity of $WO_{2.722}$ is very high which reflects the metallic character. The temperature dependence is in rough agreement with the expected T^{-1} behavior for high temperatures, indicating phonon-phonon Umklapp scattering as dominant scattering mechanism.[80]

For $WO_{2.90}$ an exceptionally low thermal conductivity was observed, with values of $\kappa \approx 3$-$3.8\,W\,K^{-1}\,m^{-1}$, which is lower than the state-of-the-art material for n-type oxides ($Zn_{1-x}Al_xO$: $>5.4\,W\,K^{-1}\,m^{-1}$[24] and slightly higher than those in the current state-of-the-art materials (e.g. $Tl_{0.01}Pb_{0.99}Te$[78]: 2.3-1 $W\,K^{-1}\,m^{-1}$, Bi_2Te_3[81, 82]: $<2\,W\,K^{-1}\,m^{-1}$, $Yb_{14}AlSb_{11}$[16, 25]: $<1\,W\,K^{-1}\,m^{-1}$). Above 600 K the thermal conductivity increases slightly and a T^{-1} behavior cannot be found which seems unusual at first. However, considering that Umklapp processes can be suppressed by defects and dislocations, the thermal conductivity at least its lattice part presumably reflects the disorder of the shear structures in the $WO_{2.90}$ compound.[42]

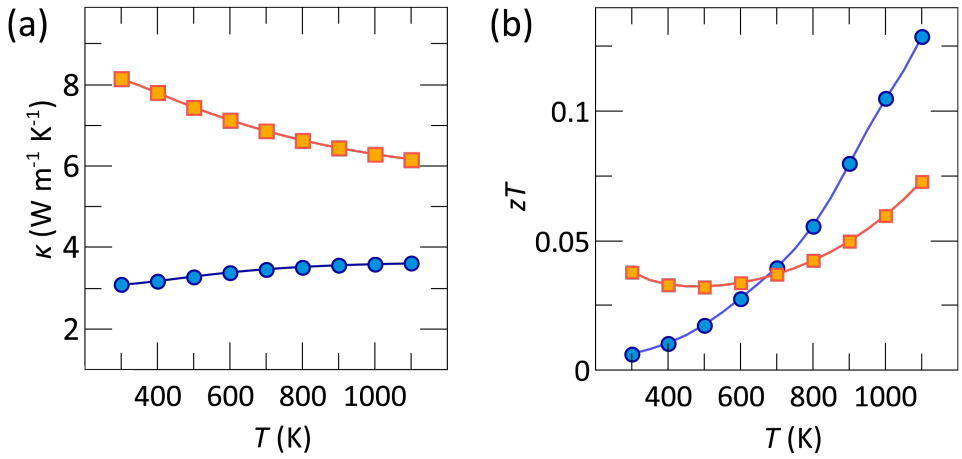

Figure 2.6: Temperature dependence of κ and zT for $WO_{2.90}$ (blue) and $WO_{2.722}$ (orange). Taking into account the values of the temperature dependent PF, the low thermal conductivity of $WO_{2.90}$ is mainly responsible for the difference in the figure of merit.

2.4.4 Figure of merit

The figure of merits are shown in Fig. 2.6(b) with maximum values of 0.13 at 1100 K ($WO_{2.90}$) and 0.07 at 1100 K ($WO_{2.722}$). For $WO_{2.722}$ zT just slightly increases with temperature which mirrors the drop of the power factor for high temperatures, cf. Fig. 2.5. The $WO_{2.90}$ phase shows a much stronger temperature dependence and reveals a better thermoelectric performance than $WO_{2.90}$ above 700 K.

Comparing the different power factors, cf. Fig. 2.5, $WO_{2.722}$ exhibits the better electronic properties over almost the entire temperature range. Therefore, the enhanced thermoelectric performance for $WO_{2.90}$ originates from the low thermal conductivity, which is correlated to the presence of shear structures and dislocations.

However, these systems are not optimized in terms of their thermoelectric performance. The small Seebeck coefficients indicate carrier concentrations that are about one order of magnitude higher than those in doped semiconductors like $Cu_{2+x}Zn_{1-x}GeSe_4$ or chalcopyrites such as $CuGaTe_2$.[83, 84]

In conclusion, the thermoelectric properties of Magnéli-type $WO_{2.90}$ and $WO_{2.722}$ have been described. The more conventional approach to looking for thermoelectric materials has focused on finding systems with large power factors followed by attempts to reduce their thermal conductivity. The strategy to decrease the thermal conductivity through crystallographic shear planes allows approaching the problem from the other direction, i.e. starting with a material that has a comparably low thermal conductivity, and then attempting to increase its power factor by adjusting power factor by changing the oxidation state of the metal. A remarkable low thermal conductivity was observed for $WO_{2.90}$, which can compete with values of the state-of-the-art materials.
Spark plasma sintering was used for consolidating the powders. Electron microscopy studies confirm the anisotropic crystal growth, which reflects the structural building principles of the

Magnéli phases. It is also reflected in the surface structure of the sintered samples, where crystallites with two main orientations appear.
However, no evidence of anisotropy was found in the physical transport properties. The non-optimized zT values of 0.13 and 0.07 at 1100 K are promising. Considering the power factor of both compounds, the more encouraging thermoelectric properties of $WO_{2.90}$ can be attributed to the low thermal conductivity, which is related to crystallographic shear, oxygen vacancies and dislocations. This study represents a proof of concept for the development of promising, cheaper, and more efficient thermoelectric conversion devices based on the strategy to use intrinsically nanostructured materials rather than artificially structured layered systems to reduce lattice thermal conductivities.

It is believed that the concept presented in this chapter will stimulate intensive research in the chemistry and physics as well as on potential application of Magnéli nanophases as thermoelectric materials.

3 Rapid SPS-assisted preparation and thermoelectric characterization of $WO_{2.90}$

3.1 Summary

This chapter focuses on the rapid SPS assisted preparation and simultaneous consolidation of the Magnéli phase $WO_{2.90}$. The high temperature thermoelectric properties of the obtained pellets are compared with conventionally processed $WO_{2.90}$ revealing a similar thermoelectric performance.

The preparation of phase pure Magnéli oxides through conventional solid-state techniques usually requires long reaction times. Additionally, the obtained powder requires consolidation for measurement of transport properties. This separate densification step with conventional hot-sintering is performed at high temperatures at which oftentimes the decomposition of the material occurs. In contrast to conventional processing, the rapid and simultaneous preparation through the SPS route shown here opens up the possibility of faster bulk preparation of complex oxides. The resulting pellet is dense and is ready for physical property measurements. Employing high throughput SPS-assisted sample preparation, SPS-assisted preparation can play a key role in understanding the underlying physics in Magnéli oxides and related materials.

In particular, conventional hot-sintering has shown to be unsuitable for the densification of Magnéli oxides. The low heating and cooling rates lead to more reduced oxides and phase purity can not retained. The thermoelectric properties of SPS processed $WO_{2.90}$ are compared with $WO_{2.90}$ prepared *via* solid state synthesis. The measured maximum zT is 0.1 at 1100 K, comparable with the zT of conventionally prepared $WO_{2.90}$.

3.2 Motivation

This section is in parts an adapted reproduction, from *J. Mater. Chem. A* 2013, submitted.

SPS has been known for more than 80 years, but it is only recently that it has attracted great attention. SPS is a field- and pressure-assisted compaction method which allows rapid (>100 K min^{-1}) heating and cooling rates, short holding times, and preparation of dense samples at sintering temperatures several hundred degrees lower than conventional hot sintering.[64, 85]

Instead of using an external heat source (as in conventional hot pressing), an electrical current (DC, pulsed DC) is passed through the conducting pressure die and/or through the sample. The factors that contribute to the rapid densification process are (i) mechanical pressures, (ii) fast heating and cooling rates and (iii) exposure to an electric field.[63] SPS has been applied for the investigation of sintering kinetics and for the rapid densification of materials while preserving small grain sizes, e.g., with minimized grain growth.[86–89] By controlling sintering kinetics, tailored microstructures can be obtained, to optimize material properties, such as the electrical conductivity, thermopower, and thermal conductivity.[66, 90, 91] The optimal balance between these is essential for successful thermoelectric materials with a high figure of merit.[2, 4, 92]

For widespread applications the preparation and subsequent consolidation steps of thermoelectrics should be rapid and inexpensive. Therefore, the single-step preparation of a dense pellet from commercially available precursors such as W and WO_3 is desired.[73, 93] It has previously been shown that this can be achieved with SPS by combined preparation and consolidation. Additionally, it has been demonstrated that there is a strong influence of the applied current on the composition of the synthesized product.[63, 64] In general, the applied current promotes the reaction of precursors, decreasing the required reaction time to form single-phase compounds.[94]

Here the SPS-assisted preparation of the Magnéli phase oxide $WO_{2.90}$ is focused.[43, 44] As shown in the previous chapter, crystallographic shear is responsible for a low intrisic thermal conductivity in $WO_{2.90}$.[95, 96] A figure of merit value of $zT = 0.13$ at 1100 K, previously found for $WO_{2.90}$ prepared by conventional methods is a promising indicator for the non-optimized system.

3.3 Results and discussion

3.3.1 Preparation and processing

The preparation method used in this contribution is illustrated in Fig. 3.1. Commercially available WO_3 and elemental W were used in stoichiometric amounts as precursor materials. A detailed description of the used equipment and procedure is given in the SI, p. 57.

SPS was employed to directly obtain $WO_{2.90}$ pellets in a single step. The processing methodology may be applied to other materials as well. The applied temperature profile is shown in Fig. 3.2. After preparation, samples were phase pure $WO_{2.90}$ with densities > 96% of the calculated theoretical density.

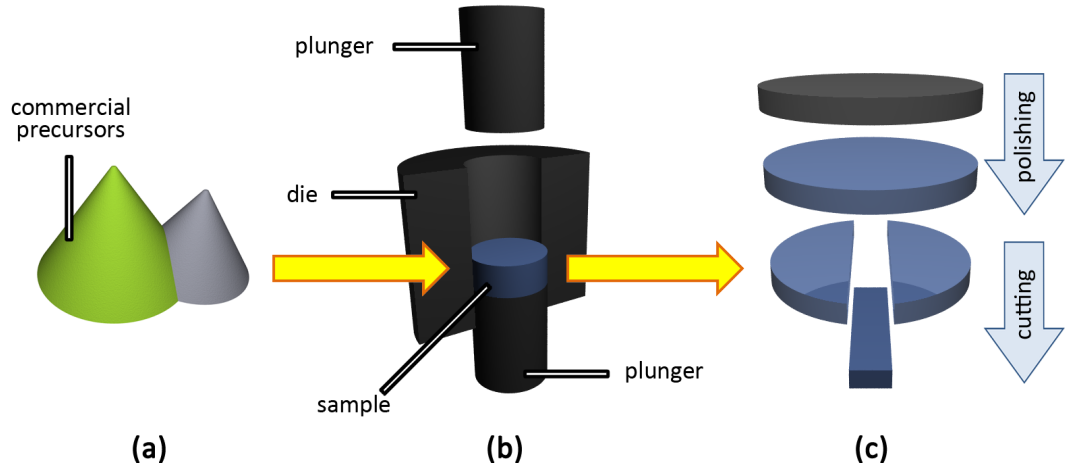

Figure 3.1: Illustration of the processing procedure. Unlike conventional approaches, reaction and consolidation take place concurrently. **(a)** Starting compounds (WO_3 and W), **(b)** the sintering die, and **(c)** processing of the solidified pellet.

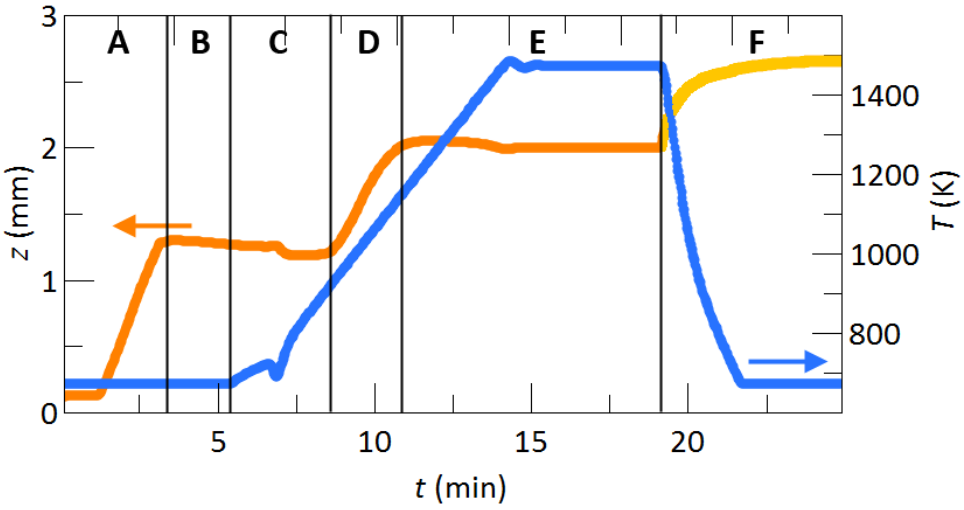

Figure 3.2: Termperature profile (blue), densification curve (orange) and decompression curve (light orange) for the spark-plasma synthesis and simultaneous consolidation of $WO_{2.90}$. Note that the temperature profile is plotted only for the pyrometer controlled heating, starting from 673 K. Capital letters indicate different segments of the process. **A** Compression and **B** heating to 673 K, **C** pyrometer-controlled heating, **D** consolidation and **E** subsequent reaction followed by **F** decompression and cooling. Whereas pressure induced densification is observed in segment **(A)**, temperature induced consolidation occurs in segment **(D)**.

In the first step a pressure of 50 MPa is applied **(A)**. The sample is then heated to 673 K **(B)** followed by pyrometer-controlled heating step **(C)** to the final temperature. The main consolidation occurs during the heating segment where the sample is rapidly heated at 100 K min^{-1} **(D)** to the final temperature 1473 K. This temperature is held for another 5 min **(E)** to ensure the entire conversion of the precursors.

After cooling the cylindrical pellet to room temperature, it is removed from the die and polished with SiC abrasive paper to clean the surface. For measuring the electronic properties, bar-shaped pieces with approximate dimensions of 10 mm × 2 mm × 1.5 mm were cut using a low-speed saw with a diamond wafering blade. The remaining material was used for microscopy and physical characterization.

3.3.2 Microstructure analysis and thermoelectric properties

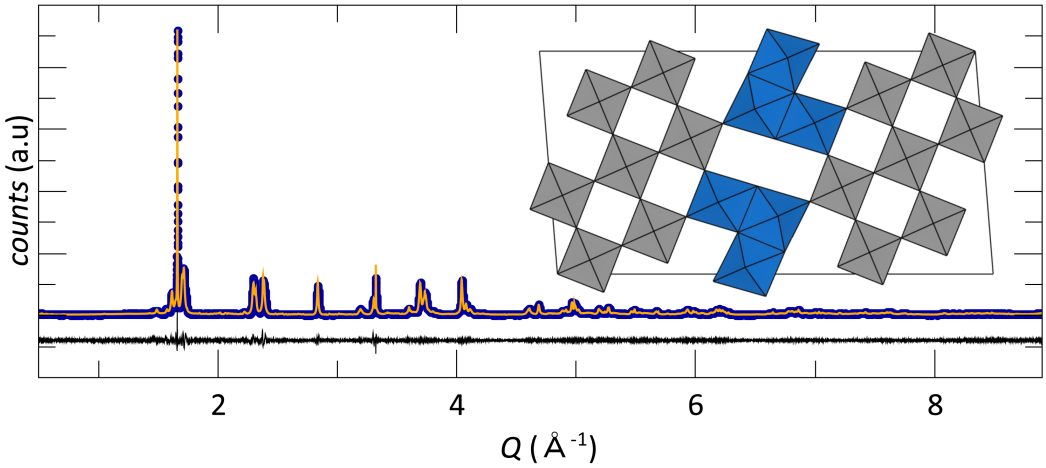

Figure 3.3: Pawley analysis of the synchrotron X-ray powder diffraction pattern indicates that $WO_{2.90}$ is single-phase. The idealized unit cell is shown in the inset, in a manner that highlights the crystallographic shear planes created by alternating layers of corner-sharing (grey) and edge-sharing (blue) octahedrons. Lattice parameters obtained agree with the literature (a = 1200.0 pm, b = 378.1 pm, c = 2350 pm ,R_{WP} = 9.8).[51]

As shown by high energy X-ray diffraction, cf. Fig. 3.3, single phase $WO_{2.90}$ is obtained after 5 min at 1473 K. Although the maximum density of 98% is reached already at 1273 K (orange curve in Fig. 3.1), the temperature must be held at 1473 K for 5 minuntes to obtain the phase pure material. Note that the increase of density in region **F** is caused by measurement artefacts which occur during the cooling process. A detailed description of the underlying sintering mechanisms can be found in the Introduction, p. 16. However, sintering for less than four minutes leads to the formation of a multiphase system. An additional minute is used as a buffer for fluctuations during the sintering process.

SEM micrographs of the polished pellet surface in Fig. 3.4 indicate the formation of a dense pellet. The grains are randomly oriented and the overall microstructure is comparable to the microstructure reported for conventionally prepared $WO_{2.90}$.[55] The grains are similar in size, but have a pronounced rod-like appearance. This observation is supported by the results of the

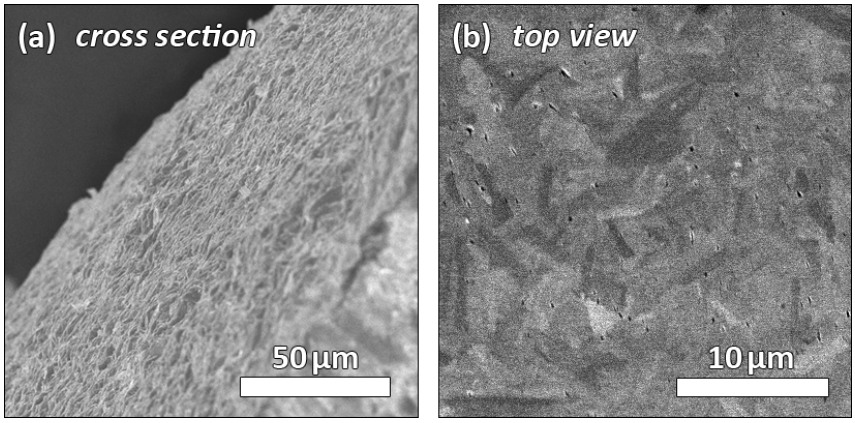

Figure 3.4: Scanning electron micrographs **(a)** cross section, **(b)** top view, reveal that $WO_{2.90}$ pellets are dense, with randomly oriented grains. The grain size is of the same order as in conventionally synthesized $WO_{2.90}$.

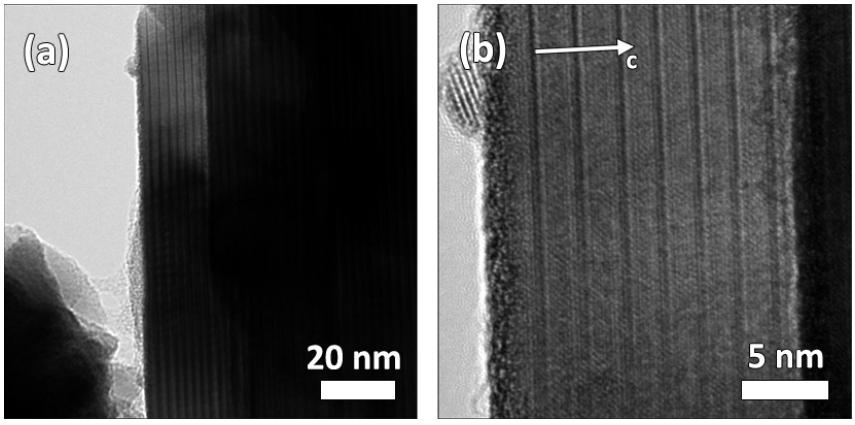

Figure 3.5: High resolution transmission electron micrographs of the obtained material. The material was cut with a diamond saw into small pieces, step size 5 nm. **(a)** shows a overview image of the observed crystal and **(b)** a high resolution image of the occuring crystallographic shear structures with a average spacing of 2.35 nm, therefore the c-axis is identified easily, as indicated.

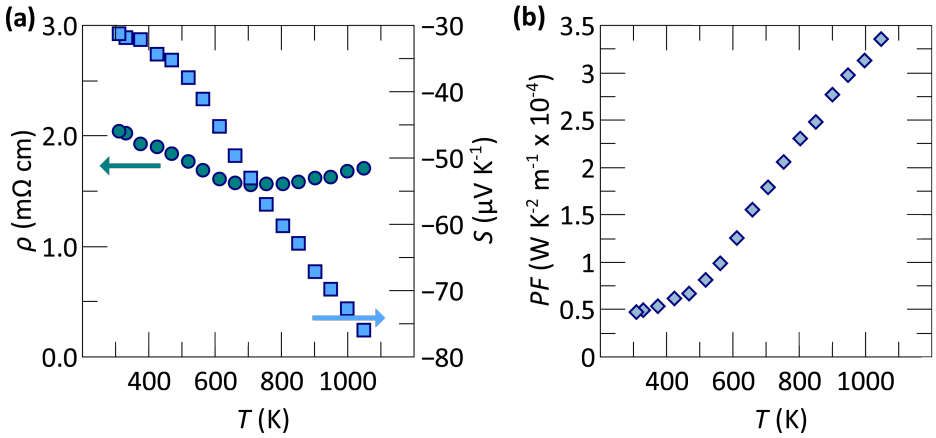

Figure 3.6: Temperature dependence of **(a)** the electrical resistivity and thermopower, and **(b)** the calculated power-factor of SPS-prepared $WO_{2.90}$. The temperature dependence of the electronic transport properties shows the behavior of a heavily doped semiconductor

X-ray powder diffraction, where a refinement of the crystallite axis was performed (average crystallite sizes along the different crystallographic axes are 40 nm (a), 227 nm (b), and 36 nm (c) respectively. The small calculated crystallite sizes reveal that the visible grains are not single crystals. To further investigate the nature of the crystallographic shear, high resolution transmission electrom micrography was conducted, cf. Fig.3.5. The spacing between the different $W^{5+}O$ building blocks (Fig.3.5(b), dark lines) underlies a variation and reflects the natural disorder in Magnéli[51]

The temperature dependence of the electrical resistivity and thermopower of $WO_{2.90}$ prepared by SPS (Fig. 3.6) is that of a heavily doped semiconductor. The monotonic increase of the thermopower with increasing temperature reveals that the maximum of the thermopower is not yet reached at 1100 K, characteristic of a wide band gap semiconductor.[28, 54] These results closely match the behavior of conventionally prepared $WO_{2.90}$.[55]

The temperature dependence of the thermal conductivity (Fig. 3.7(a)) shows a small maximum around 800 K. The temperature regime where Umklapp scattering dominates the scattering mechanism is not reached until 900 K which is consistent with the high Debye temperature of $\approx$ 600 K. Although the values of the thermal conductivity are small for conductive oxides, they are slightly higher than for conventional prepared $WO_{2.90}$. The differences between 15% and 20% are mainly attributed to the uncertainties of the applied measurement method rather than any differences of the microstructure.[60, 61]

The calculated figure of merit zT is shown in Fig. 3.7(b) and has a maximum of 0.1 at 1100 K. In comparison to the state of the art materials and other well-studied *n*-type oxide materials, the Magnéli oxides reported here are entirely non-optimized and seem to be promising in the context of new thermoelectric materials.[19]

In conclusion, SPS assisted preparation and simultaneous consolidation tunred out to be a useful tool for the large scale preparation of the Magnéli phase $WO_{2.90}$. The preparation of phase pure Magnéli oxides through conventional solid-state preparation usually requires long reaction times. Additionally, the obtained powder requires consolidation for measurement of

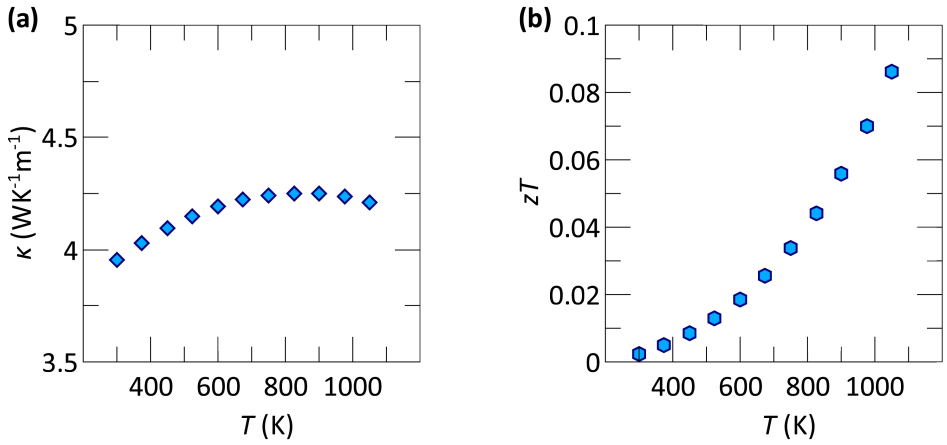

Figure 3.7: Temperature dependence of **(a)** the thermal conductivity and **(b)** the calculated figure of merit, zT of SPS- prepared $WO_{2.90}$. The slope of κ to a maximum at 800 K is consistent with the high Debye temperature (T_D = 600 K).

transport properties. This separate densification step with conventional hot-sintering was performed at high temperatures when decomposition often occurs.

In contrast to conventional processing, the rapid and simultaneous preparation and consolidation through the SPS route shown here opens up the possibility of faster bulk preparation of complex oxides. The resulting pellet is dense and suitable for physical transport property measurements. Through high sample throughput, SPS-assisted preparation can play a key role in understanding the underlying physics in Magnéli oxides and related materials. In particular, conventional hot-sintering has shown to be unsuitable for the densification of Magnéli oxides. The low heating and cooling rates lead to more reduced oxides and phase purity cannot retained.

The measured maximum zT is 0.1 at 1100 K, comparable with the figure of merits of conventionally prepared $WO_{2.90}$. Considering that the Magnéli phases are an entirely new class of materials in the field of thermoelectric research, a zT value of 0.1 for n-type oxides is promising.

4 Reduced thermal conductivity via nanosized crystallites and defects in $WO_{2.90}$

4.1 Summary

The aimed manipulation of a material property is a key step towards materials with high thermoelectric performance. In this chapter, it is shown how (W)-Ta-O scattering centres on the nanoscale can be used to improve the thermoelectric properties of the Magnéli phase $WO_{2.90}$.

SPS assisted preparation and simultaneous consolidation was used as preparation method leading to dense and single phase pellets. In addition to crystallographic shear planes and intrinsic defects as scattering centers in pure $WO_{2.90}$, (W)-Ta-O nanoscaled crystallites in the range of 5-50 nm are introduced as scattering sources. The enhanced phonon scattering on different length scales reduces the thermal conductivity by $\approx 30\%$ without changing the electrical properties, thus, the thermoelectric figure of merit is improved and a maxium zT 0.15 at 1100 K is observed.

These results present the first successful attempt of altering the thermal properties of Magnéli oxides and underlines their potential as non-toxic, chemically stable thermoelectric materials.

Table 4.1: Sample description and nominal composition of the prepared and characterized samples. The amount of Ta_2O_5 in percent is related to the amount of tungsten in $WO_{2.90}$

sample description	nominal composition	PF (900 K) ($W\,m^{-1}\,K^{-2}$)	$\kappa_{lat.}$ (900 K) ($W\,m^{-1}\,K^{-1}$)
$WO_{2.90}$ (reference)	$WO_{2.90}$	2.76×10^{-4}	3.14
3%Ta_2O_5-$WO_{2.90}$	$Ta_{0.03}W_{0.97}O_{2.90}$	2.86×10^{-4}	2.60
4%Ta_2O_5-$WO_{2.90}$	$Ta_{0.04}W_{0.96}O_{2.90}$	2.68×10^{-4}	2.12
5%Ta_2O_5-$WO_{2.90}$	$Ta_{0.05}W_{0.95}O_{2.90}$	2.85×10^{-4}	1.93

4.2 Procedure and experimental

SPS assisted preparation and simultaneous consolidation was used to prepare Magnéli oxide $WO_{2.90}$ and has been described in detail before.

Briefly, stoichiometric amounts of the precursor materials W, WO_3 and Ta_2O_5 were thoroughly ground, loaded into a graphite die and heated to 1473 K with 100 K min^{-1}. Prior to heating, a pressure of 50 MPa was applied. After a holding time of 5 min and cooling to room temperature, the cylindrical pellet was removed from the die and polished with SiC grinding paper to a clean surface.

The Seebeck coefficient and the electrical resistivity were measured simultaneously between 300 K and 1100 K on bar-shaped samples with a ZEM-3 Ulvac instrument perpendicular to the pressure axis in SPS. The thermal diffusivity was measured on compacted discs with a Netzsch laser flash diffusivity instrument (LFA 457) along the pressure axis; the samples were coated with a thin layer of graphite to minimize errors in the emissivity. The data were analyzed using a Cowan model with pulse correction. Specific heat measurements were performed on a Netzsch Pegasus differential scanning calorimeter (DSC). The specimens were heated up to 1073 K under Ar atmosphere with a heating rate of 10 K min^{-1}. The sample densities were calculated from the measured mass-to-volume ratios and the thermal conductivity was calculated with the relation $\kappa = D \cdot d \cdot C$, where D is the diffusivity, d the density and C the heat capacity. The experimental densities were determined to be between 96% and 98% of the theoretical density.[51]

Field-emission scanning electron microscopy was performed on a FEI XL40 Sirion FEG microscope with an attached Oxford Inca X-ray system for chemical analysis. After polishing, the samples (mounted in epoxy) were surrounded with silver paste in order to prevent the sample from charging during imaging. Secondary and backscattered electron images were collected with an acceleration voltages of 5 keV and 15 or 20 keV, respectively. (High resolution) transmission microscopy was perfomed on a tecnai X50 and a working potential of 5kV.[76] Powder X-ray diffraction pattern were obtained on a Philips XŠPert with CuK_α radiation. For quantitative analysis TOPAS academic, v4.1 was used, applying the fundamental parameter approach.

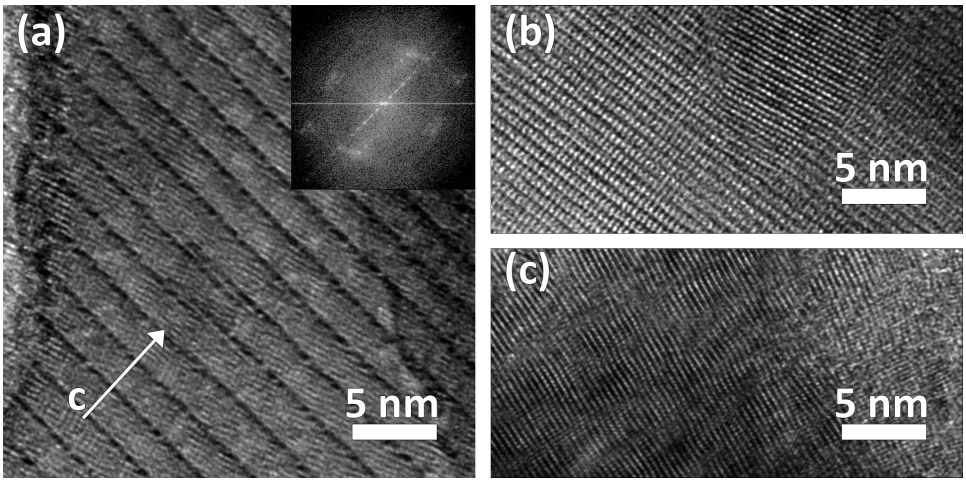

Figure 4.1: High resolution transmission electron micrographs of the reference sample $WO_{2.90}$. **(a)** The superstructure can be observed in real space as well in the corresponding FFT (inset). **(b)** and **(c)** show lattice mismatches and defects in the reference sample which are responsible for phonon scattering in the small nano scale and subnano scale.

4.3 Results and discussion

4.3.1 Microstructure analaysis

PXRD patterns of all samples show $WO_{2.90}$ as main crystalline phase, cf. SI-Fig. 7.3. The average calculated crystallite size of all samples is in the nanometer range (≈ 100 nm) and the obtained lattice parameters are in agreement with reported data, cf. SI-Tab. 7.1.[51]

Scanning electron micrographs of different samples, cf. SI-Fig. 7.4, 7.5 and 7.6 show similar grain sizes in the order of 5 μm for all samples. Therefore visible grains in SEM micrographs do not represent single-crystalline diffraction domains, which is consistent with the disorder typical for this class of oxides cf. Fig.4.1.[51, 53] The cross-sectional and top view micrographs confirm the high density of all samples >97%, with respect to the theoretical density.

High resolution transmission electron micrographs of the reference $WO_{2.90}$ and 5%Ta_2O_5-$WO_{2.90}$ samples are shown in Fig.4.1 and Fig.4.2 respectively. For 5%Ta_2O_5-$WO_{2.90}$, a higher density of defects and nanocrystalline areas can be observed in comparison to the reference sample. The assignment of the d-spacing values is desisted due to several reasons: Because of (i) many possible phases in the ternary W-Ta-O system (even the Ta-O is barely investigated) and (ii) the small crystallites, there are large uncertainties associated with the assignment of certain crystalline phases.[75]

The introduction of tantalum-rich areas in the length scale of 5-50 nm together with the high defect density in the Ta_2O_5-$WO_{2.90}$ samples plays a key role in the scattering mechanism of phonons which is discussed below.

4.3.2 Thermoelectric properties

The temperature dependences of the thermopower α and the electrical resistivity ρ (Fig.4.3, measured between room temperature and 1100 K, show the typical behavior of a heavily doped semiconductor and are insensitive to amounts Ta_2O_5. The maximum of α is not yet reached by 1100 K, which is consistent with data observed in chapter before. The calculated power factors, illustrated in Fig. 4.4(a) underline the insensitivity of the electronic transport properties towards increasing amounts of Ta_2O_5.

Temperature dependence of the thermal conductivity of the samples are shown in Fig. 4.4(b). The thermal conductivity is observed to decrease with increasing amount of Ta_2O_5. Thus the sample 5%Ta_2O_5-$WO_{2.90}$ has the smallest thermal conductivity over the measured temperature range.

Whereas in the reference sample, $WO_{2.90}$ mainly defects smaller than 3 nm contribute to phonon scattering, 5%Ta_2O_5-$WO_{2.90}$ exhibits a high amount of (W)-Ta-O crystallites in the nanoscale between 5-50 nm which further decreases $\kappa_{lat.}$.

In Fig.4.5 the calculated figures of merit are shown, indicating an increase of 50% from the stoichiometric material, due to the smaller thermal conductivity.

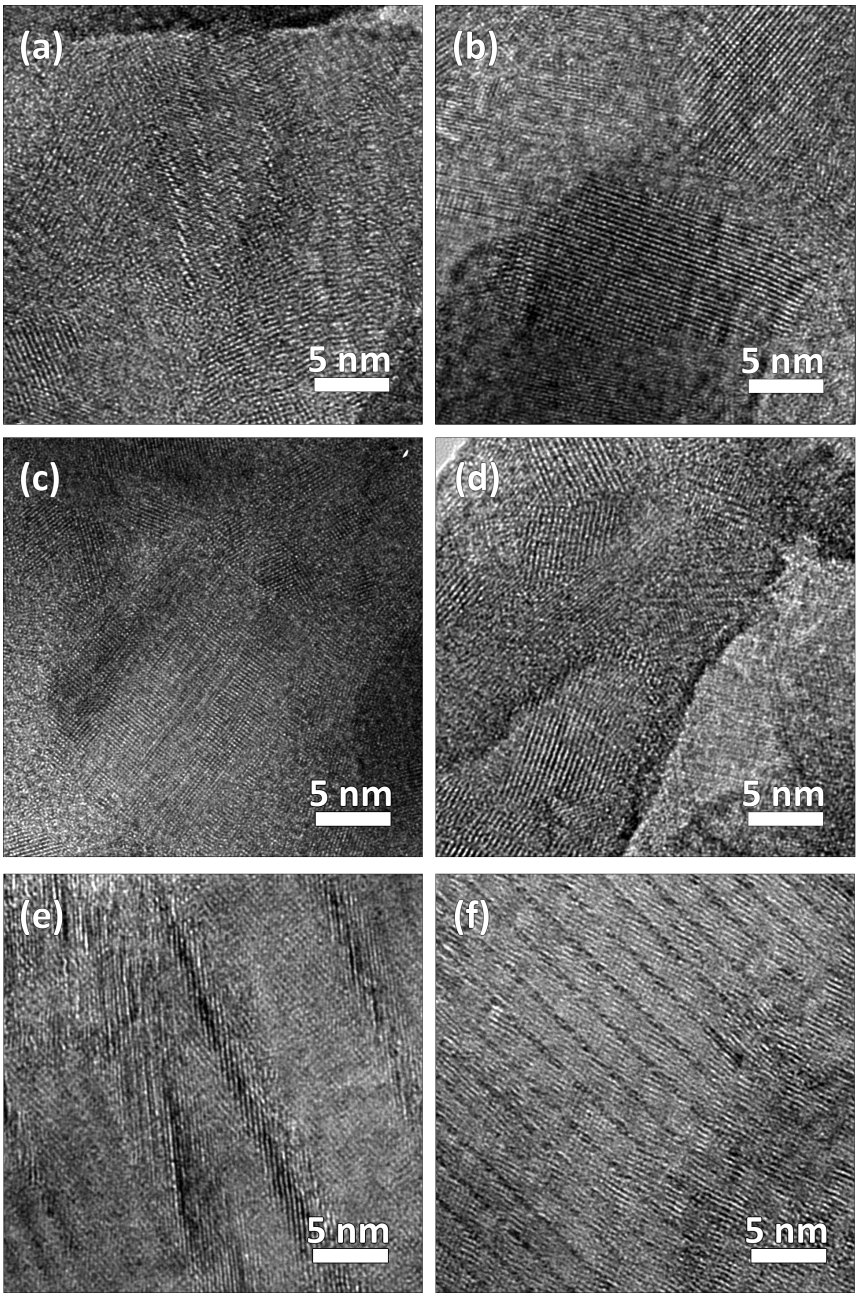

Figure 4.2: High resolution transmission electron micrographs of the sample 5%Ta_2O_5-$WO_{2.90}$ **(a)** - **(f)** show a high density of defects and nanosized crystal areas. Single crystalline areas are in the order of 5-50 nm. As defects, discloations, Wadsley defects and twin structure can be observed.

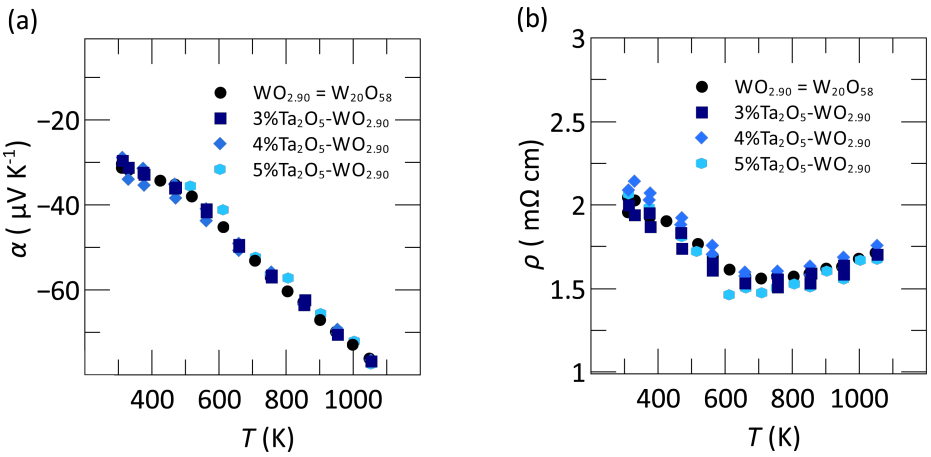

Figure 4.3: Temperature dependence of **(a)** the thermopower and **(b)** the electrical resistivity. Both properties are insensitive towards the Ta_2O_5 impurities and resemble the behavior of a heavily doped semiconductor for all samples.

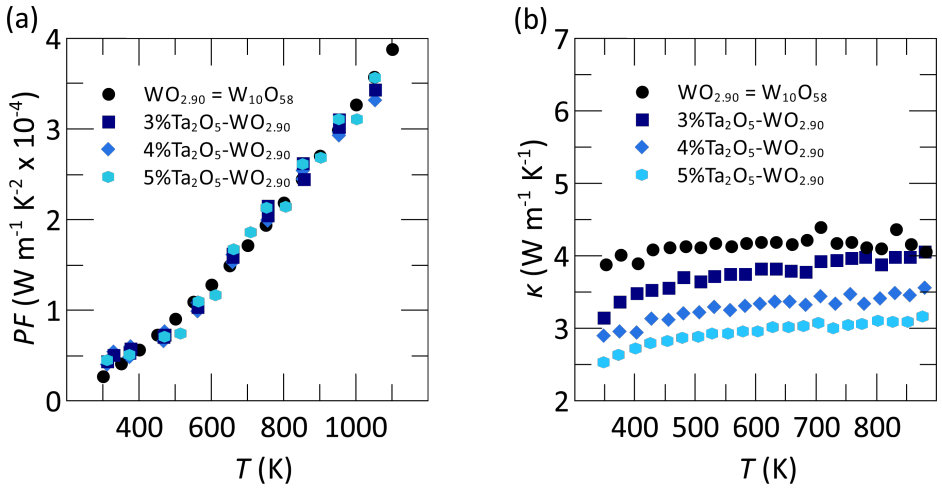

Figure 4.4: Temperature dependence of **(a)** the thermal conductivity and **(b)** the power-factor. Whereas a significant improvement of $\kappa_{Lat.}$ is observed with increasing amount of Ta, the power factors are independent of the Ta amount. Therefore the difference in the thermal conductivity has to be related to the lattice thermal conductivitiy of the samples.

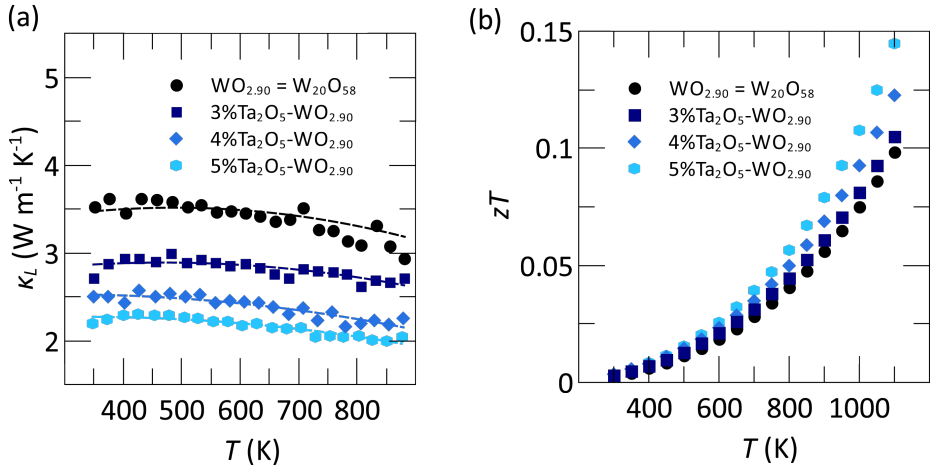

Figure 4.5: (a) Temperature dependence of the lattice part of the thermal conductivity. In contrast to other tungsten based Magnéli phases and many oxide systems, the correlation effects are not signficiant, allowing a calculation of $\kappa_{lat.}$ via the Wiedemann-Franz law **(b)** temperature dependence of the calculated figures of merit, zT. Note that the thermal conductivity was extrapolated to a temperature of 1100 K from.

4.3.3 Discussion

In the absence of bipolar contributions, the absolute thermal conductivity consists of an electronic and a lattice contribution, eq.1.6.

As the electronic transport properties influencing $\kappa_{el.}$ were unaffected by amounts of Ta_2O_5, the difference in κ is attributed to differences in $\kappa_{lat.}$ arising from the underlying microstructure. Using the Wiedemann-Franz law ($\kappa_{el.} = L\sigma T$), the lattice part of the thermal conductivity is calculated. A Lorentz number of $L = 2.00 \cdot 10^{-8}\,W\,\Omega\,K^{-2}$ is used and the resulting temperature dependence of $\kappa_{lat.}$ is presented in Fig. 4.5(a).

To understand the scattering mechanisms qualitatively, $\kappa_{lat.}$ can be expressed with eq.1.17, thereby neglecting the frequency dependency of the different parameters. The frequency dependency of the scattering relaxation time of the different scattering effects is then qualitatively considered. According to Matthiessen's rule the scattering relaxation time τ^{-1} is written as the sum of all scattering processes, eq. 1.18.

In the context of this work, contributions of Umklapp scattering τ_U^{-1}, grain boundary scattering τ_{GB}^{-1} and point defect scattering τ_{PD}^{-1} have to be considered.

Due to the high Debye temperature of the system ($T_D = 600\,K$) a clear T^{-1} behavior cannot be indicated within the applied temperature range. Additionally, it is known that Umklapp scattering can be suppressed by defects and discloations. However, for every sample shown in Fig.4.5 $\kappa_{lat.}$ decreases with increasing temperature.

The decrease of $\kappa_{lat.}$ with increasing amount of Ta_2O_5 is ascribed to enhanced phonon scattering at the defects and nano-sized crystalline areas of (W)-Ta-O. Due to grain boundary scattering τ_{GB}^{-1} is increased, which directly influences the mean free path of the phonons $l = v\tau$, thereby decreasing $\kappa_{lat.}$. Because point defect scattering is usually less dominant or nearly non existent for higher temperatures and the differences of $\kappa_{lat.}$ are constant, contributions of point defect scattering can be neglected. This is supported by (i) the small mass differences

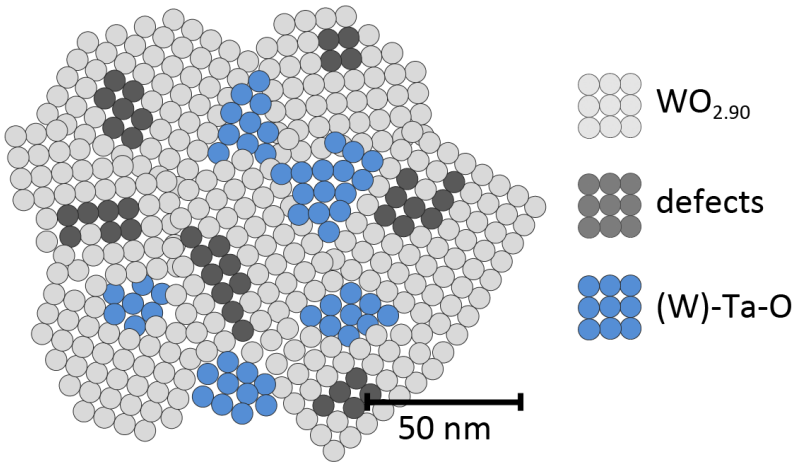

Figure 4.6: Schematic of the underlying microstructure. The nanosized crystallites (blue) consist of (W)-Ta-O and act as scattering centers for phonons thereby decreasing the mean free path of the phonons. The high defect density is indicated by the dark grey areas.

of Ta^{5+} and $W^{5+/6+}$, (ii) the similar radii of the different cations and (iii) the insensitivity of the electronic properties, which suggest that no significant amounts of Ta_2O_5 are built in the $WO_{2.90}$ lattice.[97]

A simplified scheme of the underlying nanostructure is illustrated in Fig. 4.6. The intrinsic defects (dark grey) and (W)-Ta-O scattering centers (blue) are highlighted to underline their influence on the thermal transport characteristics.

In conclusion, this chapter shows how the thermal conductivity of the Magnéli oxide $WO_{2.90}$ phase can be altered by introducing (W)-Ta-O crystallites as scattering centers. In the pure $WO_{2.90}$ compound, crystallographic shear planes and defects on the subnano scale are identified by HRTEM as scattering sources for phonons. With the addition of (W)-Ta-O crystallites, interfacial phonon scattering in the 5-50 nm range is introduced. As a result, $\kappa_{lat.}$ is lowered by 50% over the entire measured temperature range while the electronic properties remain unaffected, therefore enhancing the thermoelectric performance. The observed maxium figure of merit is 0.15 at 1100 K.

The large unit cell and the high electrical conductivity combined with a low lattice thermal conductivity make Magnéli phases an interesting class of materials for thermoelectric research. So far, just a small part of the field of Magnéli phases has been investigated and this work presents the first successful attempt to alter the thermal transport properties. The next step towards an even lower thermal conductivity is the introduction of scattering centers on the scale of 100-500 nm to scatter phonons over the entire distribution of phonon mean free path lengths. Additionally, the electronic properties have not been optimized; a future goal is to control the carrier concentration.

This knowledge is important not only for tungsten based Magnéli oxides but also for the optimization of other binary or ternary systems with potential thermoelectric application.

5 Wet chemistry route towards nanoparticular antimonides and thermoelectric characterization of nano-$FeSb_2$

5.1 Summary

In this chapter a facile wet chemistry route towards nanoparticular binary metal antimonides including the thermoelectric promising material $FeSb_2$ is presented. It is shown how grain boundary scattering on the nanoscale can be used to alter the thermal transport properties of $FeSb_2$. The obtained results emphasize the challenge in thermoelectric research to control the highly interrelated material properties independently of each other.

During the past few decades transition metal antimonides have attracted much industrial and academic interest. Their great variety of electrical and magnetic properties originating from the variable compositions makes them intresting materials in metallurgy and solid-state science. Compounds, such as $FeSb_2$, $CoSb_3$ and Zn_4Sb_3 have long been characterized as promising materials in thermoelectric devices.

Low-dimensional materials and nanomaterials are known to exhibit properties that are fundamentally different from those of the corresponding bulk compounds. The number of low temperature synthesis methods for nanocrystalline intermetallic compounds of the late transition metals has increased dramatically over the past few years, however, the preparation of nanocrystalline antimonides has not been focus of extensive studies. Therefore, a low temperature wet chemistry route is optimized allowing for the formation of intermediate and metastable antimony intermetallic phases including nanoparticular $FeSb_2$, CoSb, NiSb, Cu_2Sb and ZnSb.

In case of *nano*-$FeSb_2$, SPS was used as consolidation method in order to determine the influence of nanoscale interfaces on the thermal transport and thermoelectric properties in general. Although the thermal conductivity is lowered by more than 80% in comparison to the bulk value, an enhancement of the thermoelectric figure of merit is not achieved due to the decreased electronic performance of the compound.

5.2 Motivation

This section is in parts an adapted reproduction from *Inorg. Chem.* **2011**, 50, 6938 and *Dalton Trans.*, **2013**, submitted.

The main task in the field of thermoelectric research is to overcome the highly interrelated material properties and in this context grain boundary scattering of phonons on different length scales has shown to be an effective approach.[2, 98] Due to the decreased mean free path of the phonons the lattice part of the thermal conductivity is reduced thereby improving the thermoelectric performance.[1, 99] Therefore, recent studies have focused on obtaining dense materials of sintered nanoparticles[14, 66, 100] superlattice systems [15, 101] and nanosegregations [102] of high zT bulk materials.[103]

Compounds such as $FeSb_2$, $CoSb_3$ and Zn_4Sb_3 have long been characterized as promising materials in thermoelectric devices and potential anode materials.[104–108] To further investigate possible candidates within the antimonide family, phase pure nanoparticular samples must be prepared and characterized.

The synthesis of intermetallic compounds usually requires high reaction temperatures and long reaction times for the thermodynamically stable phase to be formed. Besides, nanoparticles are sensitive to heat because of crystal growth during longer heating periods. The number of low temperature synthesis methods for nanocrystalline compounds of the late transition metals has increased dramatically over the past few years. *In situ* reduction in high boiling solvents, (modified) polyol processes, and solvothermal reaction allow the syntheses of metastable intermetallic phases.[109–113]

In contrast to the well-established polyol process, the wet chemistry route which is presented here, starts from metal particles and/or carbonyl precursors; that is, no additional salts (from reducing agents) or organic compounds are present in the synthesis (besides possible organic impurities in the solvents used). Therefore this method can yield products without further impurities. In addition, this synthesis route allows the production of macroscopic masses of single-phase nanopowders and thus allows further investigations of the thermoelectric properties.

Kondo systems and highly correlated electron systems such as $FeSb_2$ and $FeSi_2$ are promising candidates for cryogenic thermoelectric applications due to their favorable electronic properties at low temperatures. Localized d- or f-states mix with conduction electron states leading to a formation of a small hybridization gap with extremely sharp densities of states next to the band gap.[114, 115]

For independent electrons interacting with static scatterers the Mott formula describes the relation between the thermopower and the density of states.[116] Clearly, this formula oversimplifies the situation in Kondo systems, but the thermopower is still highly sensitive to the density of states close to the chemical potential. Therefore, large values of the thermopower are expected in Kondo and highly correlated electron systems, as has been shown for $FeSb_2$[105], FeSi[117], CeB_6[118], $Ce_3Sb_4Pt_3$[119], CeF_4P_{12}[120] and $CeRu_4Sb_{12}$[121]. For single crystalline $FeSb_2$, a thermopower of $\alpha = -42000\,\mu V\,K^{-1}$ at 10 K is found[105], leading to the highest reported power-factor ($\alpha^2\sigma$) but so far, the thermoelectric performance is limited by the large thermal conductivity of the compound. Recent approaches on $FeSb_2$ thin films

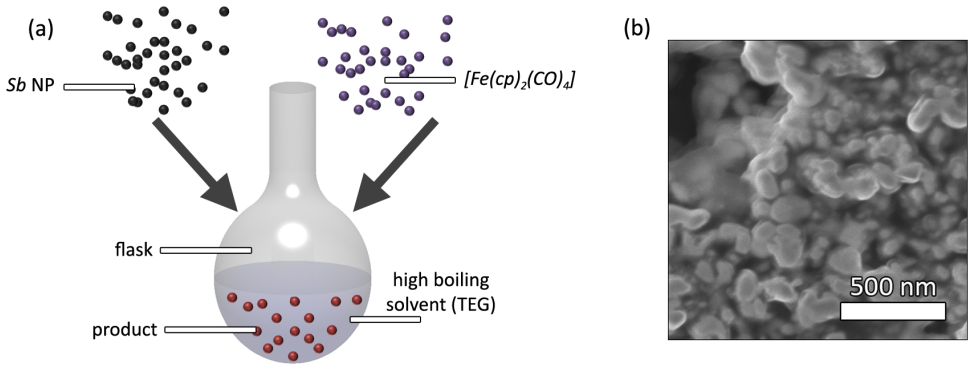

Figure 5.1: (a) Schematic of the applied wet chemistry route. Activated Sb nanoparticles and $Fe(cp)_2CO_4$ are used as precursors and tetraethylenglycol (TEG) as solvent. In contrast to the classical polyol process, no additional reducing agent is necessary therefore minimizing the possibilty of impurities. So far, the detailed influence of the solvent is not determined, but the coordination of the solvent to the reactands and products surface seems to be crucial. **(b)** Scanning electron micrograph of the obtained $FeSb_2$ nanoparticles reveals agglomerated particles with sizes in the range of 50 to 200 nm.

and nanoparticular $FeSb_2$ prepared via a solvothermal method indicate a significant reduction in both the thermal conductivity and the thermopower of the compound.[122, 123]

5.3 Experimental

A description of the detailed experimental procedure can be found in the Supporting Information, p.64. Here, the experimental approach is briefly described and compared to other preparation methods for nanoparticular antimonides.

A schematic of the wet chemistry route for the preparation of $FeSb_2$ nanoparticles is shown in Figure 5.1. In general, antimony nanoparticls are either reacted with other metal nanoparticles or reacted with a molecular precursor and are produced by a reduction of $SbCl_3$ with lithium triethylboronhyride $Li[(Et)_3B]H$ at room temperature.

Activated nanoparticles are highly reactive in ambient air, leading primarily to the formation of Sb_2O_5. ^1H NMR data of Sb nanoparticles kept in an inert gas atmosphere show an intense signal according to surface bond stibane ($\delta \approx 1.05\,ppm$), which broadened when the particles were in contact with air.[124, 125]

In case of antimony it is very difficult to obtain well separated, monodisperse nanoparticles. Nevertheless this synthetic technique was studied to obtain intermetallic binary antimonides for a proof of principal study with a focus on the thermal conductivity, therefore, the interface density is important. However, the activated Sb particles are used in a solution based approach, which allows to study the influences of additional reaction parameters on the forming binary antimonide nanoparticles. Therefore the activated nature of the nanoparticles without any capping agents or polymers on their surface is of great importance. A TEM image and powder X-ray diffraction pattern of activated Sb nanoparticles are shown in SI-Fig. 7.13. Ni, Cu and Zn nanoparticles were prepared from the corresponding chlorides. For the syn-

Table 5.1: Reaction conditions for the preparation of nanoparticular late transition metal antimonides. Activated Sb nanoparticles were used as antimony source and reacted with stoichiometric amounts of the metal precursor.

compound	metal precursor	solvent	reaction temperature (K)	heating rate ($K\,min^{-1}$)
$FeSb_2$	$[Fe_2(cp)_2(CO)4]$	TEG	300	10
$CoSb$	$Co_2(CO)_8$	TEG	280	5
$NiSb$	Ni NP	TEG	180	5
Cu_2Sb	Cu NP	TOA	160	5
$ZnSb$	Zn NP	TOA	300	15

thesis of NiSb, ZnSb and Cu_2Sb nanoparticles of the corresponding metal were dispersed in a high-boiling solvent and added to the solution of antimony nanoparticles and the mixture was heated to temperatures between 420 K and 570 K. For the formation of $FeSb_2$ and CoSb, antimony nanoparticles were reacted with $Fe(cp)_2CO_4$ and Co_2CO_8. Presynthesized Fe and Co nanoparticles did not lead to the formation of a phase pure compound.

With the help of powder X-ray diffraction data of the reaction intermediates, the reaction conditions for the formation of the different antimonides were optimized in terms of (shortest) reaction time, phase purity and crystallinity.

5.4 Results and discussion

5.4.1 Wet chemistry route

By starting from small metal particles, solid state diffusion is no longer the rate-limiting step of the reaction and different phases are accessible. In contrast to conventional solid state reactions that allow the formation of the thermodynamically stable product, nanostructured metastable[113] and intermediate compounds can be made by this approach.

However, this synthesis approach is highly sensitive to a variety of parameters, such as heating rate, final temperature, reaction time, solvent and precursor material. On the other hand, this variety of reactions conditions also allows an optimization of the reaction process to obtain the target phase. For example, in the case of NiSb, ZnSb and Cu_2Sb, metal nanoparticles could be used as precursor materials, whereas $FeSb_2$ and CoSb could only be obtained by using molecular precusors, cf. Table 5.1. Additionally, for CoSb, Cu_2Sb and ZnSb only the solvent shown in Table 5.1 led to the formation of phase pure materials, whereas for NiSb the solvent seems to have a minor influence.

The NiSb phase was also obtained if other solvents (trioctylamine, triethylenglycol) were used. One reason for the higher flexibility of the synthesis conditions for NiSb could be its rather broad phase width compared to those of the other compounds described here.
PXRD studies of the reaction intermediates and final products revealed that all target phases form during the heating step. For the synthesis of CoSb, Sb was consumed upon further heating. The reaction yields pure CoSb at 550 K, cf. SI-7.16. For $FeSb_2$, NiSb, Cu_2Sb and ZnSb the target phases and precursor compounds were crystalline at the final temperature

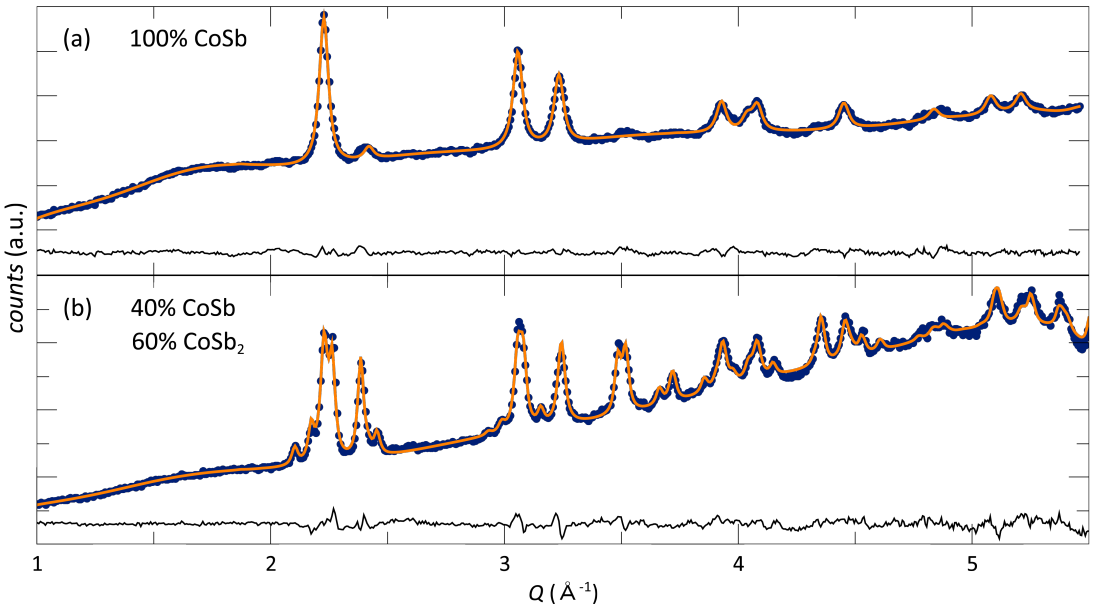

Figure 5.2: Influence of the heating rate on the composition of the $CoSb/CoSb_2$ system. Experimental data (blue dots), Rietveld fits (orange line), and corresponding difference plots (black line). **(a)** Optimized heating rate, $5\,K\,min^{-1}$, yields phase pure CoSb. **(b)** Heating rate $15\,K\,min^{-1}$ yields a mixture of CoSb and $CoSb_2$. Excess Co was removed with 1 M HCl.

and subsequently reacted to form the final product. The size of the obtained nanoparticles is between 10-250 nm and the nanoparticles show no evidence for anisotropic particle growth, cf. SI-Fig. 7.14.

As mentioned above, the resulting nanoparticle phases and the product distribution strongly depend upon the reaction conditions, and they are sensistive towards variation of these variables. The most important reaction parameters are (i) overall reaction time, (ii) final temperature and (iii) heating rate.

The overall reaction time seems to control the progress of the reaction between the antimony nanoparticles and the metal precursors. Thus, short reaction times result in impurities of unreacted antimony. The final temperature and heating rate control the phase formation and the phase purity as shown in Figure 5.2 for the $CoSb/CoSb_2$ system. In a similar way, variations of the synthesis parameters lead to the formation of $NiSb_2$ impurities during the synthesis of NiSb.

5.4.2 Densification of *nano*-$FeSb_2$ and microstructure analysis

In the wet chemistry approach no additional surfactants are used and therefore agglomerated particles in the range of 50-200 nm are obtained, cf. Figure 5.1(b). Infrared spectroscopy measurements of the obtained black powder show a absorption band at $2870\,cm^{-1}$, typically observed for C-H vibrations, which is attributed to remaining solvent molecules attached to the surface.

SPS was used as a consolidation method in order to prevent nanoparticles from growing during the densification process. Neglecting the consolidation due to particle rearrange-

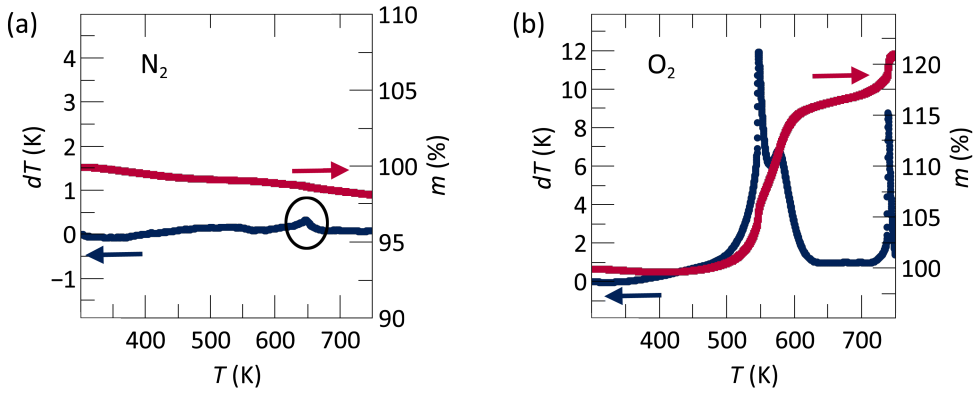

Figure 5.3: TG/DTA measurements of $FeSb_2$ nanoparticles prepared by the wet chemistry approach described above, **(a)** under N_2 and **(b)** O_2 atmosphere. An exothermic reaction is observed around 650 K and therefore sintering was conducted with a final temperature of 523 K.

ment, densification mainly occurs as a result of surface-energy minimizing processes. In this simple picture SPS can be interpreted as a competition between particle growth and densification. Grain growth processes usually exhibit lower activation energies and therefore low heating rates and long-time sintering favor particle growth whereas high heating rates mainly suppress growth processes. Additionally, particle rearrangement is supported by high temperatures. Therefore, SPS with its high heating rates represents the optimal tool for the consolidation of nanoparticles thereby maintaining the small crystallite sizes.

The optimal sintering temperature was achieved *via* DTA/TG measurements under N_2 cf. Fig. 5.3(a). Over the whole temperature regime a mass loss of 2 % was observed. The first significant exothermic reaction occurs at around 620 K which is ascribed to a decomposition into $FeSb_{1+x}$ and elementary Sb. Sintering was conducted with a final temperature of 523 K, 100 K below the phase transition considering local temperature fluctuations. DTA/TG measurements under O_2 atmosphere reveal oxidation processes starting at around 500 K. However, previously conducted transmission electron microscopy studies on nanoparticular $FeSb_2$ which were stored under ambient conditions revealed a passivating oxide layer that formed at room temperature and therefore all experiments were conducted under inert atmosphere.[124]

Powder X-ray diffraction analysis of a sintered bar revealed $FeSb_2$ to be the main phase. As determined by PXRD analysis the average diffraction domain size of SPS-treated $FeSb_2$ was 88 nm (see Fig. 5.4) which is consistent with the average crystallite size of 40 nm of pristine $FeSb_2$. Although SPS is the optimal tool for the consolidation of nanoparticles, particle coarsening cannot entirely be suppressed. Elemental Sb was found as impurity and inhomogenity is confirmed by element mapping (Fig. 5.5). Carbon as possible impurity after SPS treatment was excluded by microstructure analysis (Fig. 5.5(d)). Oxygen was found only in the small cracks (Fig. 5.5(e)). The content of iron and antimony varies in the volume of the sample ((Fig. 5.5(b) and (c)) and regions with different iron to antimony rations can be recoginzed. Among all those phases, only $FeSb_2$, elemental antimony and iron oxide were detected as

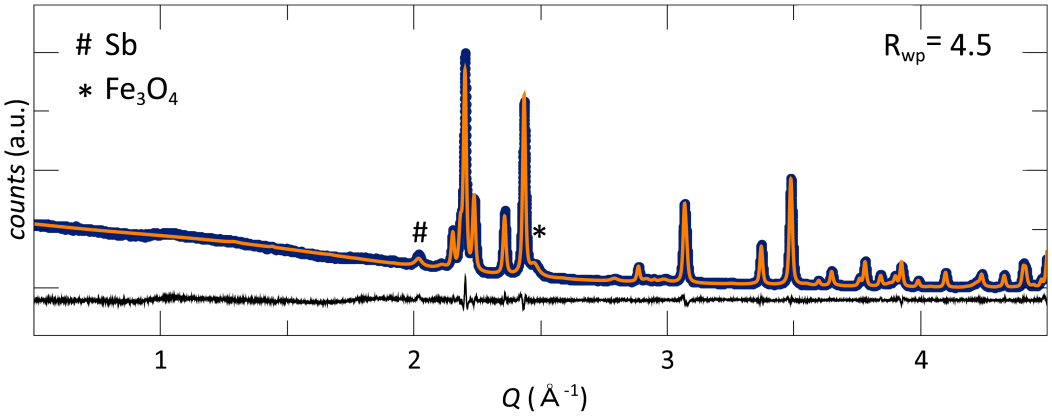

Figure 5.4: Powder X-ray diffraction pattern of the sintered sample (blue), Rietveld fit (orange) and corresponding difference curve (black). The calculated average crystallite size is 88 nm and the obtained lattice parameters match those reported in the literature (a = 582.8 pm, b = 673.6 pm, c = 319.9 pm).[126] Strongest reflections of the impurities are indicated with # (Sb) and ∗ (Fe_3O_4).

crystalline ones by PXRD (Fig. 5.4). All other phases observed in the microstructure seem to be amorphous intermediates of the preparation reaction.

5.4.3 Thermoelectric properties of spark plasma sintered *nano*-$FeSb_2$

Temperature dependence of the thermopower α and electrical resistivity ρ are shown in Fig. 5.6(a). α rapidly decreases with increasing temperature to a minimum of $\alpha_{min.}$ = -78 $\mu V\,K^{-1}$ at $T_{min.}$ = 30 K, indicating *n*-type conduction in the low temperature regime. As the temperature increases further, α increases reaching positive values around 148 K. The overall values of the electronic transport properties match with previous studies conducted on nanoparticular $FeSb_2$ synthesized *via* a solvothermal process.

The observed minimum of α is shifted to higher temperatures and smaller values compared to single crystalline $FeSb_2$ ($T_{min.}$ = 10 K, $\alpha_{min.} \approx 47000\,\mu V\,K^{-1}$) and polycrystalline bulk $FeSb_2$ ($T_{min.}$ = 25 K, $\alpha_{min.}$ = -500 $\mu V\,K^{-1}$).[105, 123] The reported value is significantly smaller than for single crystalline and bulk $FeSb_2$ where a giant mobility was found for the charge carriers, $\mu = 10^5\,cm^2\,V^{-1}\,s^{-1}$.[127] The collapse of the thermopower is attributed to reduced correlation effects associated with the small size of particles.

ρ decreases with increasing temperature; the higher resistivity in comparison to bulk $FeSb_2$ is ascribed to the lower mobility of the charge carriers. These results are highly consistent with values reported in the literature and stress the relation between electrical resistivity and thermopower. Studies on $FeSb_2$ thin films also connected the reduced mobility with the low value of α.[122, 123, 127]

The temperature dependence of the thermal conductivity of SPSed $FeSb_2$ nanoparticles is shown in Figure 5.6 (b). In order to estimate the direct influence of grain boundary scattering on the thermal conductivity, the lattice part of the thermal conductivity is calculated using the Wiedemann-Franz law, $\kappa_{el.} = L\sigma T$, with $L = 2{\cdot}10^{-8}\,W\,\Omega\,K^{-2}$ the Lorenz-number.[30, 128]

In comparison to bulk polycrystalline $FeSb_2$ a reduction of nearly 80% is achieved. This reduction is presumably caused by the small crysallite sizes, leading to enhanced phonon

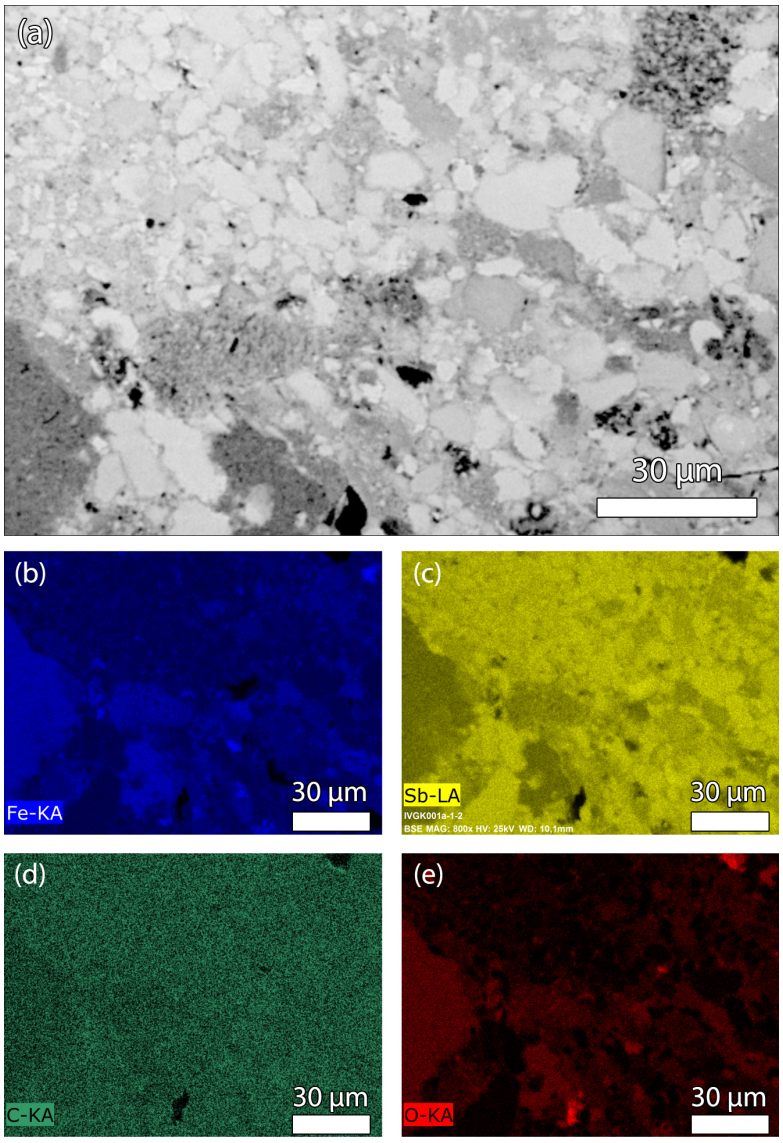

Figure 5.5: (a) Microstructure and element mapping of sintered $FeSb_2$ with distribution of (b) iron, (c) antimony, (d) carbon and (d) oxygen.

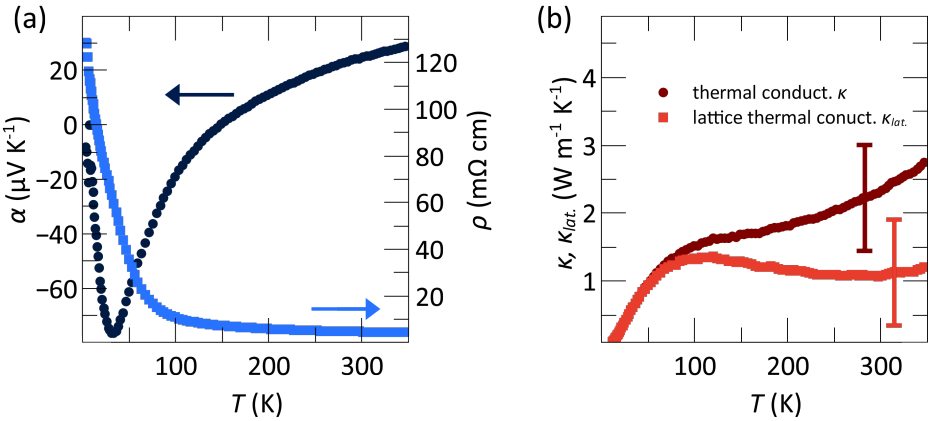

Figure 5.6: Temperature dependence of **(a)** the thermopower (dark blue), the electrical resistivity (light blue) **(b)** the thermal conductivity (red) and the lattice part of the thermal conductivity, $\kappa_{lat.}$ (light red). Although the thermal conductivity is reduced about nearly 80% with respect to the bulk value, an enhancement of the figure of merit is not achieved because of the drop of the thermopower. Note, the error of the measurement of the thermal conductivity is in the order of the obtained values, as highlighted in the figure.

scattering at the nanoscaled interfaces. According to eq. 1.17, $\kappa_{lat.}$ can be treated within the Debye approximation, thereby neglecting the frequency dependencies of the parameters. By introduction of grain boundary scattering on the nanoscale, l is reduced significantly leading to a reduction of $\kappa_{lat.}$.

Although an exceptional reduction of the thermal properties of the compound is achieved, no enhancement of the thermoelectric figure of merit is gained. The reduced crystal size suppresses the correlation effects and therefore a thermopower is obtained which is signficiantly smaller than for polycrystalline and single crystalline $FeSb_2$.

In conclusion, this chapter presents a facile, flexible wet chemistry route towards nanoparticular late transition metal antimony nanoparticles, $FeSb_2$, CoSb, NiSb, Cu_2Sb and ZnSb. Furthermore the low temperature thermoelectric properties of spark plasma sintered $FeSb_2$ nanoparticles are reported.

Powder X-ray diffraction analysis of the sintered pellet reveals nanoparticular $FeSb_2$ as main phase with elementary Sb and Fe_3O_4 as impurities. The conducted microstructure investigations show a dense pellet with an inhomogeneous appearance and EDX analysis reaveal several regions with different antimony to iron ratios. However, the obtained temperature dependent thermoelectric properties match with previous reported results of nanoparticular $FeSb_2$ which were prepared by a solvothermal approach. The thermal conductivity is reduced by more than 80% with respect to the bulk value caused by enhanced grain boundary scattering on the nanoparticular interfaces.

Although the thermal conductivity is reduced exceptionally, an enhancement of the figure of merit could not be achieved because of the absolute thermopower is decreased which is attributed to reduced correlation effects caused by the small crystal size.

These results give another remarkable example how grain boundary scattering on the nanoscale can help to improve the thermoelectric performance of a material but also emphasizes the challenge in the field of materials science in general, to overcome the highly interrelated material properties, to prepare desired materials with distinct physical properties.

6 Conclusion and outlook

This thesis focused on the investigation of the thermoelectric properties of tungsten Magnéli oxides and spark plasma sintered $FeSb_2$ nanoparticles.

With tungsten Magnéli phases a highly promising class of oxides for thermoelectric materials has been identified. The combination of a metal-like electrical conductivity, crystallographic shear structures, and a large primitive unit cell makes this materials interesting for thermoelecric research. In a proof of principle study the suboxides $WO_{2.90}$ and $WO_{2.722}$ have been prepared *via* solid state preparation and the powders were densified using SPS. The fast heating rates of SPS ensure no further reduction during densification and dense single phase pellets of $WO_{2.90}$ and $WO_{2.722}$ could be obtained. Transport measurements showed semiconducting ($WO_{2.90}$) and metal-like ($WO_{2.90}$) behavior with a zT of 0.13 at 1100 K. Especially $WO_{2.90}$ exhibits a low intrinsic thermal conductivity which is ascribed to crystallographic shear planes acting as phonon scattering centers.

To further enhance the thermoelectric performance more systematically, a rapid SPS-assisted preparation towards phase pure $WO_{2.90}$ was elaborated starting from commercially available precursors. This SPS-assisted approach was then used for the gradual introduction of (W)-Ta-O scattering centers on the nanoscale. The increased interfaces density led to a reduction of $\kappa_{lat.}$ with increasing amounts of Ta_2O_5 thereby enhancing the thermoelectric figure of merit, zT to 0.15 at 1100 K.

The next step towards a high zT material is the detailed investigation of the elecronic structure of Magnéli oxides and complex oxide materials in general, followed by an optimization of the power factor, $\alpha^2\sigma$. So far, *ab initio* calculations showed that $WO_{2.90}$ can be treated as a heavily doped semiconductor, however, the carrier concentration does not seem optimized for thermoelectric application. The great variety of complex oxides which fulfill the requirements for materials with inherent low thermal conductivities such as defect perovskite solid solutions and ternary Magnéli oxides is encouriging for the future.

Furthermore, a facile wet chemistry route towards binary nanoparticular antimonides was developed to obtain pure $FeSb_2$ nanoparticles and other late transition metal antimonides such as CoSb, NiSb, Cu_2Sb and ZnSb. In order to perform transport measurements, spark plasma sintering was used as consolidation method to prevent particles from grain growth. Low temperature thermoelectric properties of $FeSb_2$ show a reduction of thermal conductivity by more than 80% due to grain boundary scattering of heat carrying phonons. However, an improvement of the zT could not be achieved due to a decreased thermopower in the nanoparticles. These results emphasize the difficult challenge in thermoelectric research to overcome the highyl interrelated material properties.

7 Supporting Information

Experimental: SPS assisted Preparation of $WO_{2.90}$

For the preparation and simultaneous consolidation the temperatre profile described in Chapter 3 was applied. SPS treatments were provided on the SPS - HP D 5, FCT machine (Germany). Stoichiometric amounts of W and WO_3 were ground to a fine powder and loaded into graphite dies with an inner diameter of 20 mm. Carbon foil was used to surround the powder specimen on all sides, isolating the specimen from contact with the graphite die and plungers during the SPS experiment.

After cooling to room temperature, the cylindrical pellet was removed from the die and treated with SiC abrasive paper to clean the surface from any carbon residues. For measuring the electronic properties, bar-shaped specimens were cut using a low-speed saw (Allied Inc.) with a diamond blade. The remaining material was used for microscopy and physical characterization. Samples for microscopy were fixed in epoxy (Buehler Epomet) by hot compression mounting, ground with silicon carbide abrasive paper, and finally polished to 0.25 μm surface roughness with colloidal diamond on cloth.

High-resolution synchrotron powder diffraction data were collected at beamline 11-BM at the Advanced Photon Source (APS), Argonne National Laboratory using a wavelength of $\lambda = 0.41315$ nm. Data were fit using TOPAS Academic v4.1 program suite, using the fundamental parameter approach.[76] Field-emission scanning electron microscopy was performed on a FEI XL40 Sirion FEG microscope with an attached Oxford Inca X-ray system for chemical analysis. After polishing, the samples (mounted in epoxy) were surrounded with silver paste in order to prevent samples from charging during imaging. Secondary and backscattered electron images were collected with acceleration voltages of 5 keV and 15 or 20 keV, respectively.

The Seebeck coefficient and the electrical resistivity were measured simultaneously between 300 K and 875 K on bar-shaped pieces perpendicular to pressure axis in SPS with a ZEM-3 Ulvac instrument. The thermal diffusivity, D, was measured on compacted discs with a Netzsch laser flash diffusivity instrument (LFA 457) along the pressure axis; the samples were coated with a thin layer of graphite to minimize errors in the emissivity. The data were analyzed using a Cowan model with pulse correction. The specific heat (C) measurements were performed on a Netzsch Pegasus differential scanning calorimeter (DSC). The specimens were heated up to 1073 K under Ar atmosphere with a heating rate of 10 K min^{-1}. The experimental sample densities, d, were calculated from the measured mass-to-volume ratios and were determined to be between 96 % and 100 % of the theoretical density. The temperature dependent thermal conductivity D was calculated using the relationship $\kappa = C_p \cdot D \cdot d$.

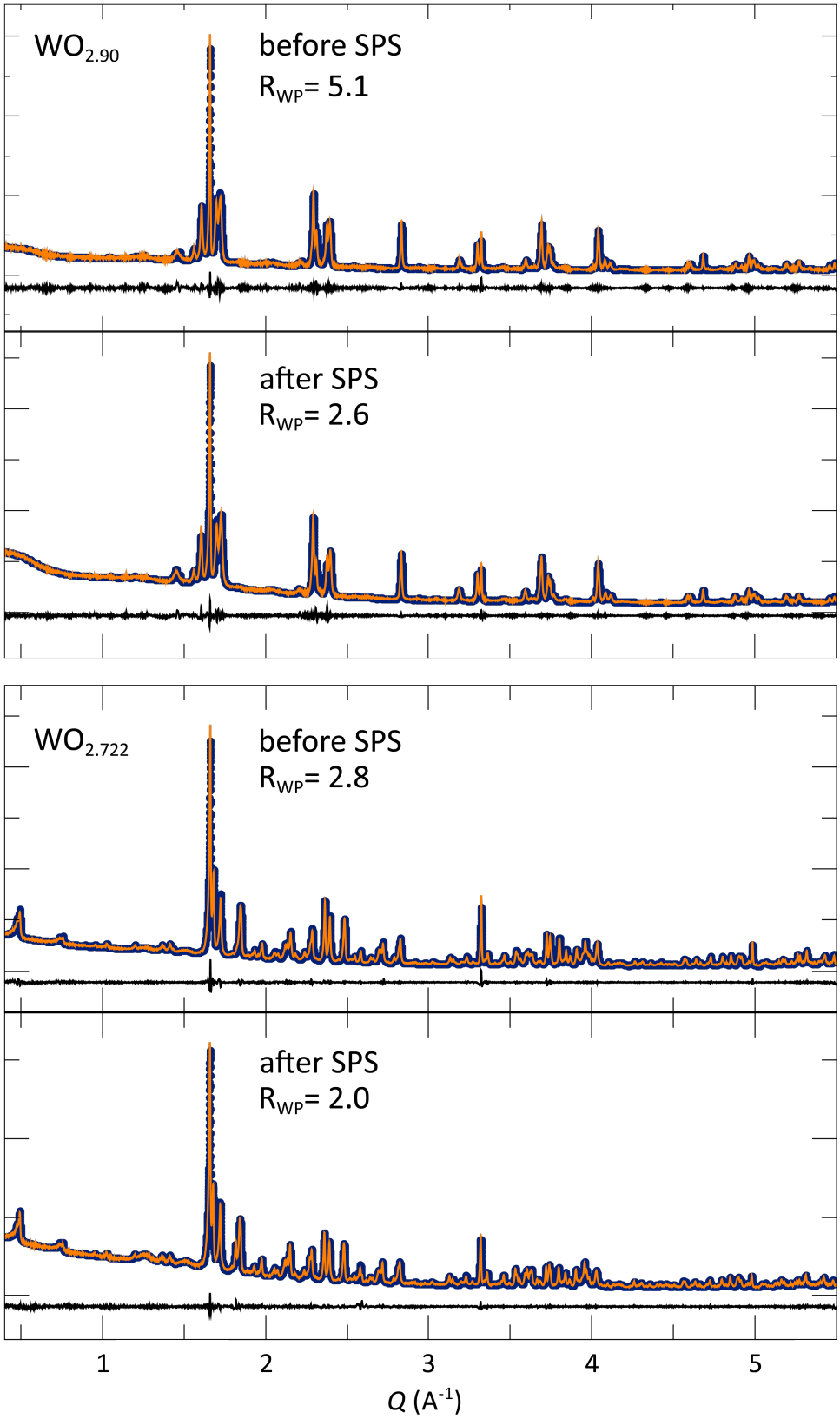

SI-Figure 7.1: Powder X-ray diffraction pattern of $WO_{2.90}$ (top) $WO_{2.722}$ (bottom) before and after spark plasma (SPS) treatment including the profile fit and profile difference of the corresonding Pawley refinement. No Phase decomposition is observed during consolidation.

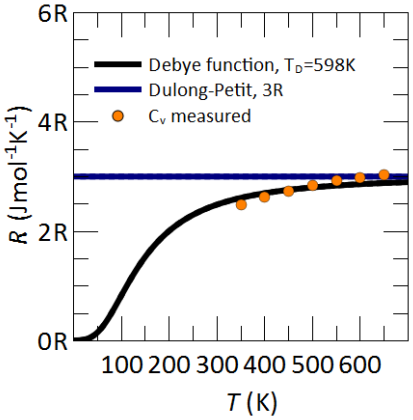

SI-Figure 7.2: Numerical fit (black) of the Debye function to the heat capacity of $WO_{2.90}$ reveals a Debye temperature of $T_D \approx 600$ K. The error is estimated to ± 25 K.

Table 7.1: Refined lattice parameters of the different samples $WO_{2.90}$, 3%Ta_2O_5-$WO_{2.90}$, 4%Ta_2O_5-$WO_{2.90}$ and 5%Ta_2O_5-$WO_{2.90}$. The lattice parameter reported in the literature are a = 12.1 Å, b = 3.76 Åand c =23.6 Å.[51] The errors of the refined lattice parameter are smaller $\pm$ 0.002 Å. The errors for the calculated crystallite size are $\pm$ 5 nm.

compound	refined lattice parameters (Å)	calculated avg. crystallite size (nm)	R_{WP} (R_{Bragg})
$WO_{2.90}$	a = 12.03 b = 3.783 c =23.59	183.1	8.5 (0.56)
3%Ta_2O_5-$WO_{2.90}$	a = 12.01 b = 3.777 c =23.57	196.1	8.4 (0.56)
4%Ta_2O_5-$WO_{2.90}$	a = 12.03 b = 3.784 c =23.61	167.5.1	8.8 (0.53)
5%Ta_2O_5-$WO_{2.90}$	a = 12.03 b = 3.783 c =23.61	201.2	8.3 (0.50)

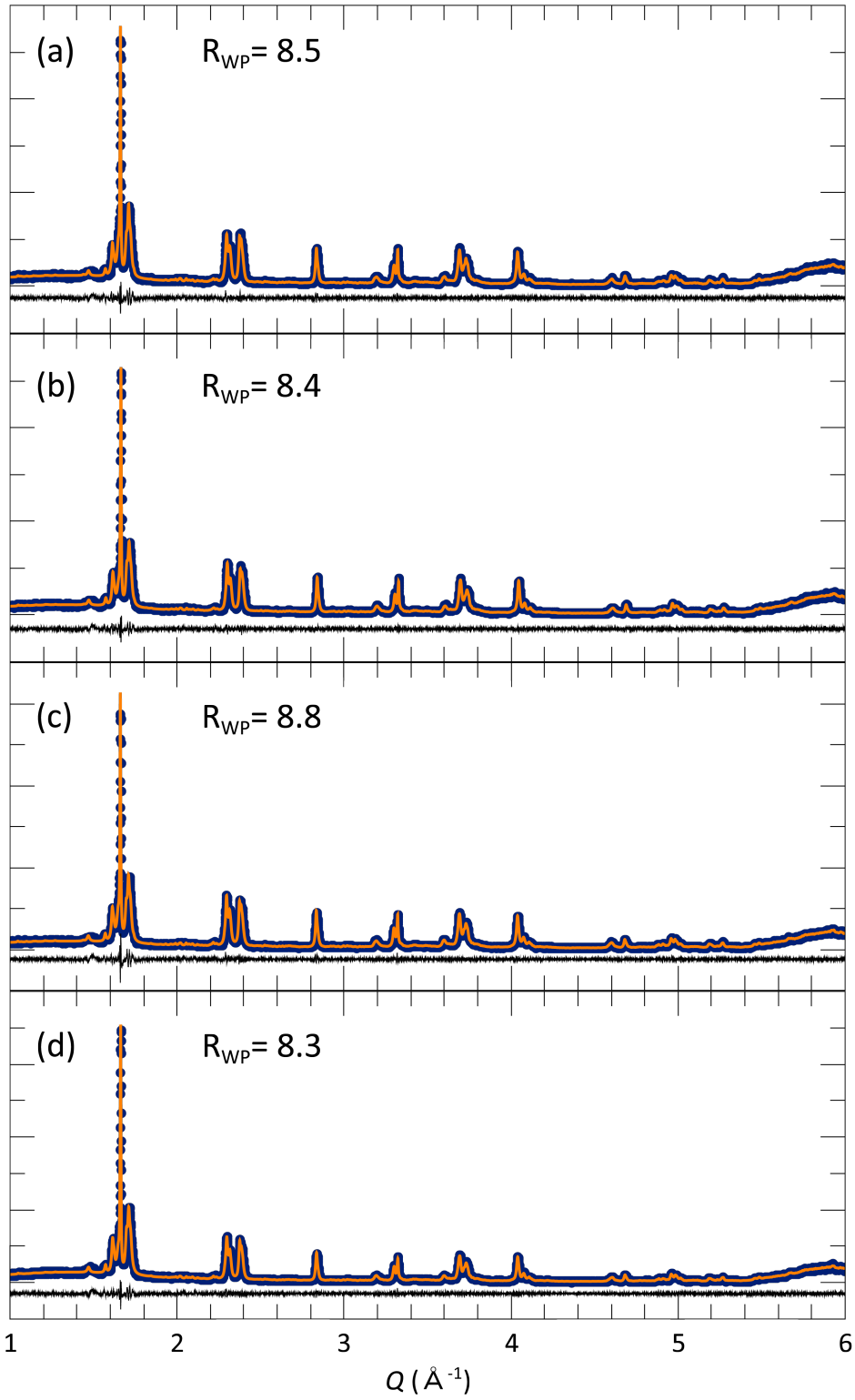

SI-Figure 7.3: Powder X-ray diffraction pattern of **(a)** $WO_{2.90}$, **(b)** 3%Ta_2O_5-$WO_{2.90}$, **(c)** 4%Ta_2O_5-$WO_{2.90}$ and **(d)** 5%Ta_2O_5-$WO_{2.90}$ including profile fit and profile difference of the corresponding Pawley refinement. All patterns show single phase $WO_{2.90}$.[51]

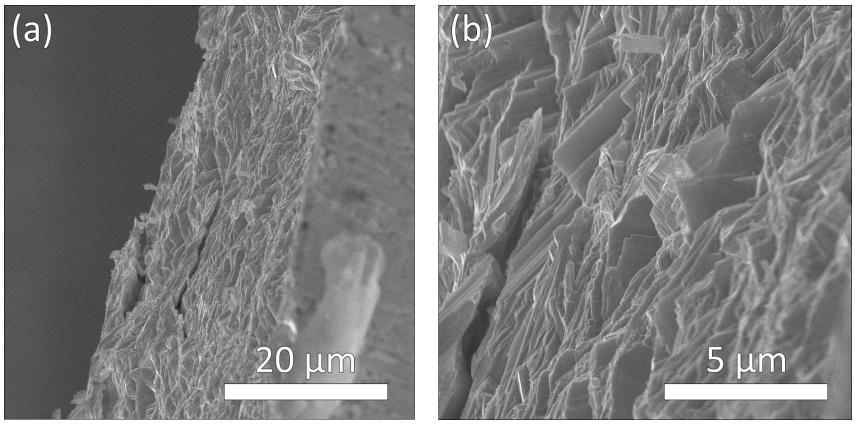

SI-Figure 7.4: Scanning electron micrographs of 3%Ta_2O_5-$WO_{2.90}$, cross section image

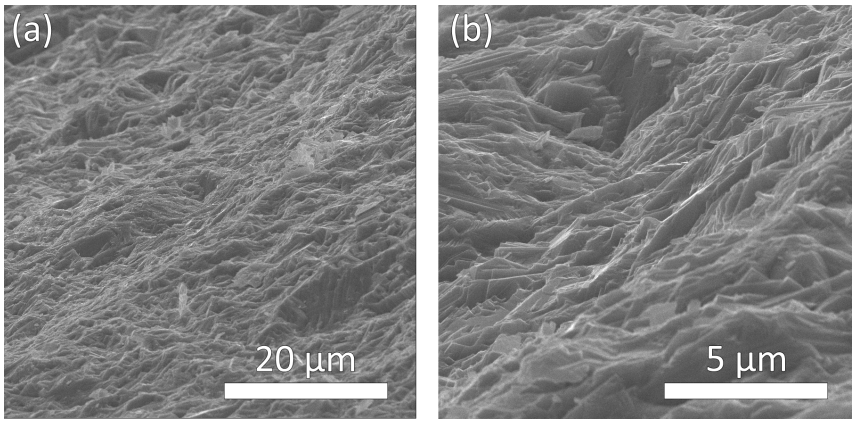

SI-Figure 7.5: Scanning electron micrographs of 4%Ta_2O_5-$WO_{2.90}$, cross section image

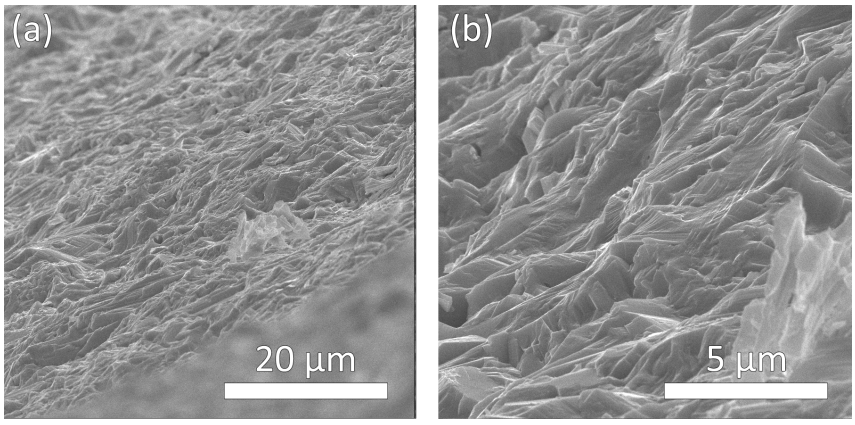

SI-Figure 7.6: Scanning electron micrographs of 5%Ta_2O_5-$WO_{2.90}$, cross section image

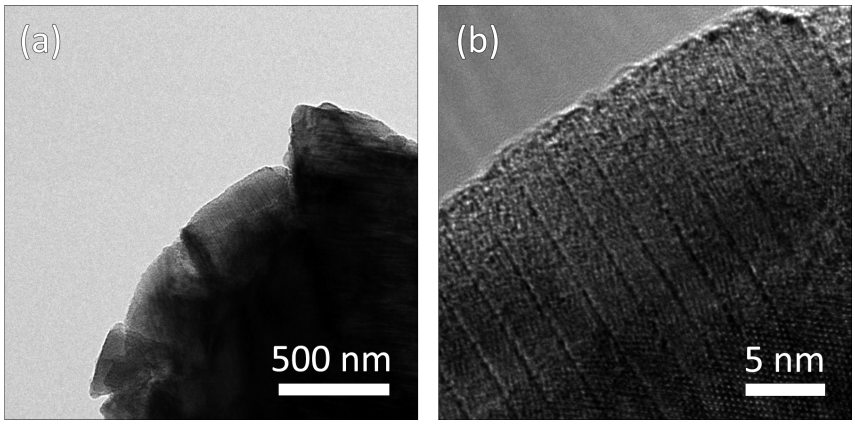

SI-Figure 7.7: HRTEM micrographs of $WO_{2.90}$

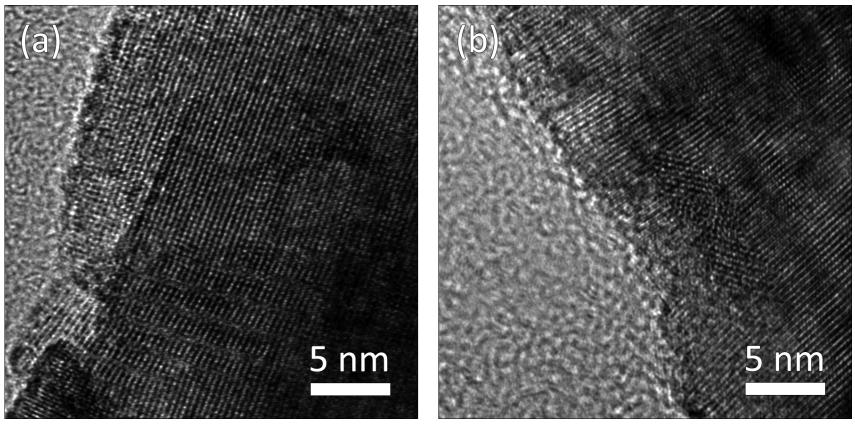

SI-Figure 7.8: HRTEM micrographs of $WO_{2.90}$

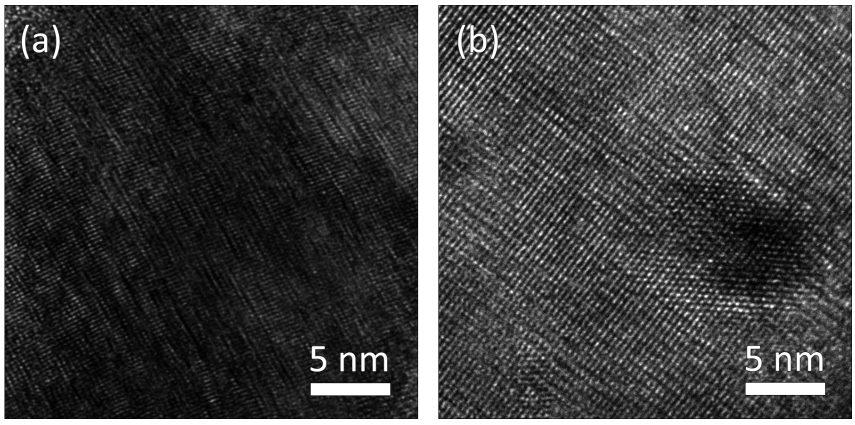

SI-Figure 7.9: HRTEM micrographs of $WO_{2.90}$

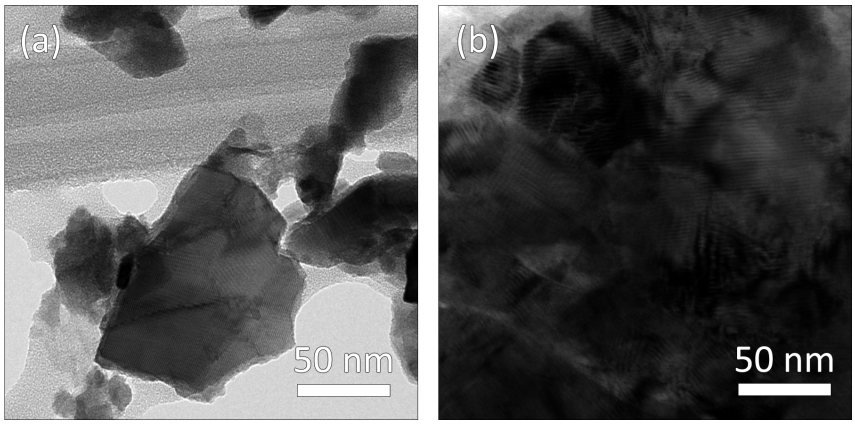

SI-Figure 7.10: HRTEM micrographs of 5%Ta_2O_5-$WO_{2.90}$

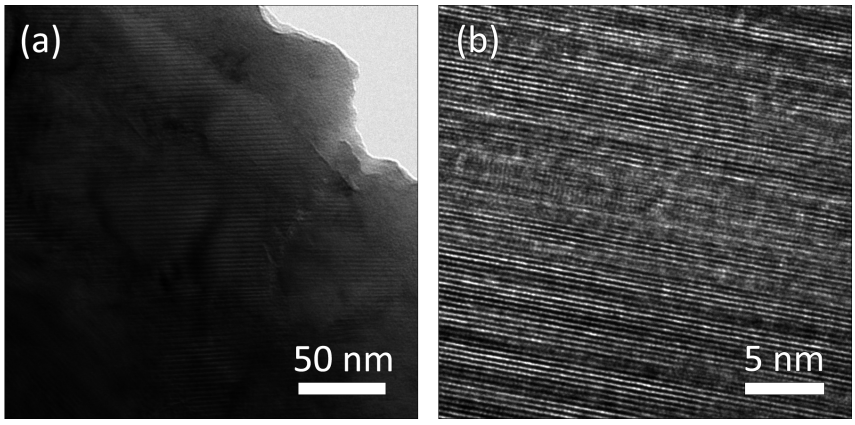

SI-Figure 7.11: HRTEM micrographs of 5%Ta_2O_5-$WO_{2.90}$

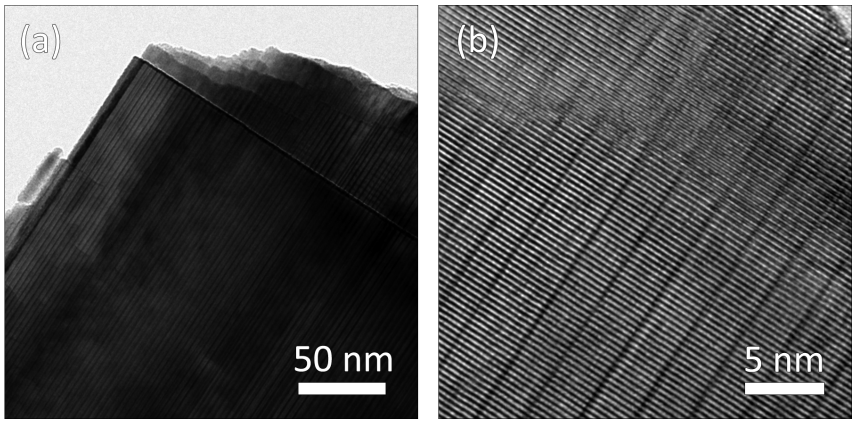

SI-Figure 7.12: HRTEM of 5%Ta_2O_5-$WO_{2.90}$

Experimental: Preparation of metal nanoparticles

Synthesis of Metal Nanoparticles. $ZnCl_2$ (ABCR, 99.999%), $NiCl_2$ (Sigma-Aldrich, 99.99%), and CuCl (ABCR, 99.995%) were first dried with thionylchloride, washed with toluene, dried *in vacuo*, and stored in a glovebox under N_2 atmosphere. Tetrahydrofuran was dried with $CaCl_2$ and Na/K and freshly distilled before use. Lithium triethylboronhydride Li[Et_3BH] (Aldrich, 1M in THF, referred to as superhydride) and $SbCl_3$ (ABCR, 99.99%) were used as obtained, and $SbCl_3$ was stored in a glovebox. Zn particles were synthesized by the reaction of $ZnCl_2$with 2 equiv. of the 1 M solution of superhydride in THF at 338 K. The particles were washed several times with THF, dried in a vacuum, and stored in a glovebox. Sb particles, Ni particles, and Cu particles were produced by reducing $SbCl_3$, $NiCl_2$, and CuCl with 3, 2, and 1 equiv. of the 1 M superhydride solution at room temperature, respectively. The black poweder was repeatedly redispersed in THF and decanted from the solution, dried in a vacuum, and kept in a glovebox.

Synthesis of Binary Antimonide Nanoparticles. Trioctylamine and tetraethyleneglycol (Aldrich, 98%) were degassed and stored under Ar before use.

$FeSb_2$. In a typcial synthesis, nanoparticles of the nominal composition $FeSb_2$ were prepared by reacting Sb nanoparticles (1 mmol) in tetraethleneglycol with a heating rate of $\approx$15 K min^{-1}. A dispersion of cyclopentadienyl iron(II) dicarbonyl dimer (0.5 mmol) in approximately 3 mL of tetraethyleneglycol was added to the reaction when the Sb solution reached a temperature of around 373 K. The reaction mixture was then heated to 573-583 K at a rate of 10 K min^{-1} and held at that temperature for 60 min. For intermediate products, 2 ml of the solution was extracted by a syringe at approximately 473, 523, and 573 K and after 60 min.

CoSb. In a typical synthesis, nanoparticles of the nominal composition CoSb were prepared by heating of Sb-nanoparticles (1 mmol) and $Co_2(CO)_8$ (0.5 mmol) in tetraethyleneglycol with a heating rate of about 5 K min^{-1}. The reaction mixture was heated to ca. 553 K. For intermediate products, 2 mL of the solution was extracted by syringe at approximately 423, 473, 523, and 553 K. After the solution was cooled to room temperature, the resulting black product was collected by centrifugation (9000 rpm), washed with ethanol, and dried under a steady Ar flow.

NiSb. In a typical synthesis, nanoparticles of the nominal composition NiSb were prepared by heating of Sb-nanoparticles (1 mmol) and Nanoparticles (1 mmol) in tetraethyleneglycol (ultrasound bath for 10 min) with a heating rate of about 5 K min^{-1}. The reaction mixture was heated to ca. 443 K and held there 210 min. For intermediate products, 2 mL of the solution was extracted by syringe at approximately 343, 353, 413, and 443 K. After the solution was cooled to room temperature, the resulting black product was collected by centrifugation (9000 rpm), washed with ethanol, and dried under a steady Ar flow.

Cu_2Sb. In a typical synthesis, nanoparticles of the nominal composition Cu_2Sb were prepared by heating of Sb-nanoparticles (1 mmol) and Cu-nanoparticles (2 mmol) in tricotylamine (ultrasound bath for 10 min) with a heating rate of about 5 K min^{-1}. The reaction mixture was heated to ca. 433 K and held there for 180 min. For intermediate products, 2 mL of the solution was extracted by syringe at approximately 323 and 373 K. After the solution was cooled to room temperature, the resulting black product was collected by centrifugation (9000 rpm)

and washed with ethanol. Afterward, the black powder was washed two times with 1 M HCl in saturated NH_4Cl solution to remove possible Cu residues. The powder was then again washed with ethanol and dried under a steady Ar flow.

ZnSb. In a typical synthesis, Sb- and Zn-nanoparticles were heated to 573 K at a rate of ca. 15 K min^{-1} in a polar, strongly coordinating solvent (trioctylamine) to prevent nanoparticle aggregation. The reaction mixture was held at ca. 573 K for 60 min before it was allowed to cool down. Products were collected by centrifugation, washed with ethanol, and subsequently dried in vacuo. The syntheses had to be carried out using an excess (3:1) of zinc metal to ensure all Sb reacted to form the desired product. The additional Zn can be removed after the reaction by repeated treatment of the solid residue with dilute acetic acid. The product was then washed with ethanol and dried with streaming Ar to a dry powder.

Compaction and Characterization. SPS treatments were carried out on a SPS-515 ET, Dr Sinter setup (SDC-Fuji, Japan). The fine powders were prepared in an Ar-filled glove box and loaded into WC dies with an inner diameter of 8×1.5 mm. High density $FeSb_2$ bars were obtained by heating to 523 K wit a rate of 100 K min^{-1} under an uniaxial pressure of 650 MPa in vacuum with a hodlding time of 5 min. Temperature measurement within the SPS setup was performed by means of a thermocouple insde the die wall.

Low-temperature transport properties were peasured on the bar-shaped specimen using a PPMS system (Quantum Design). Energy dispersive X-ray spectroscopy was performed on a scanning electron microscope Philips XL30 (cathode LaB_6; EDAX Phoenix system, Si(Li) detector). Carbon-coated specimen were used for SEM studies.

Powder X-ray diffraction experiments were carried out with a Huber G670 camera (Guinier geometry) Co $K_{\alpha 1}$ radiation with a step size of $\Delta 2\theta = 0.005$ř.

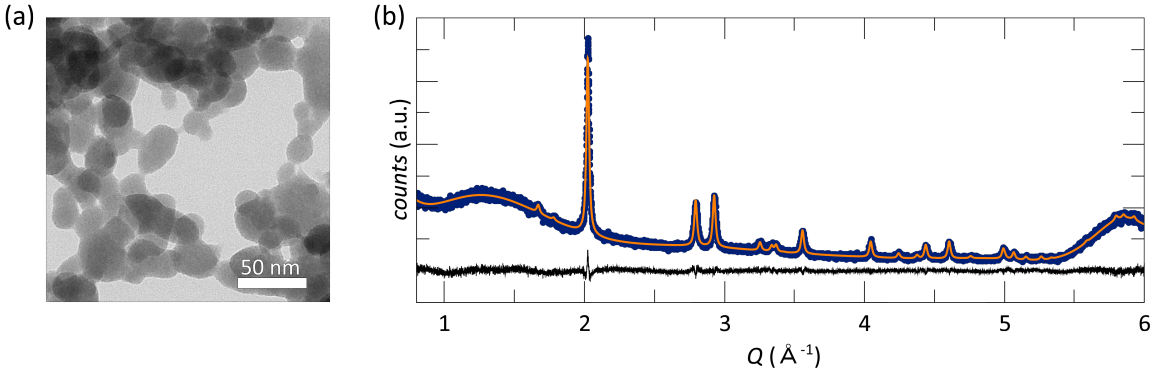

SI-Figure 7.13: (a) Transmission electron micrograph of activated *Sb* nanoparticles and **(b)** powder diffraction pattern including pawley fit. The calculated lattice parameters and average crystal size of 30 nm agree with the particle sizes obtained from transmission electron micrographs.

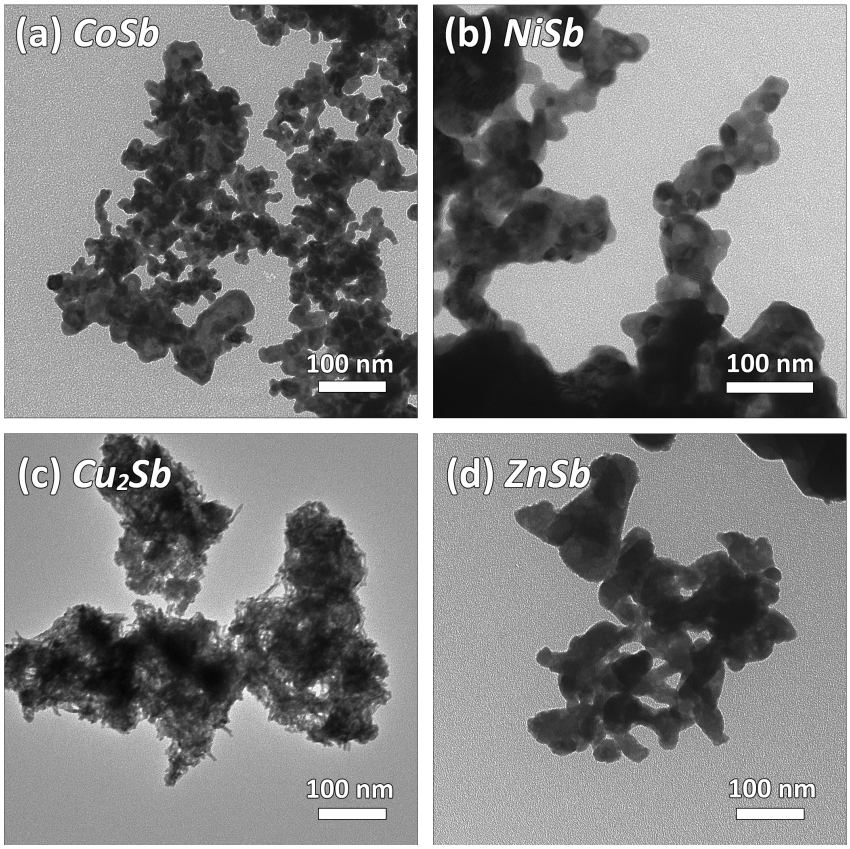

SI-Figure 7.14: Transmission electron micrographs of prepared antimonide nanoparticles that show particle sizes in the range of 10 - 250 nm.

Table 7.2: Refined lattice parameters of the obtained compounds and literature values. The errors of the refined lattice parameter are smaller $\pm$ 0.003 Å. The errors for the calculated crystallite size are between $\pm$ 0.14 nm and $\pm$ 1.82 nm.

compound	reported lattice parameters (Å) (bulk)	refined lattice parameters (Å) (nano)	calculated avg. crystallite size (nm)	r_{WP} (r_{Bragg})
$FeSb_2$	a = 5.833 b = 6.539 c = 3.204	a = 5.833 b = 6.539	39.1	5.9 (1.9)
$CoSb$	a = 3.890 c = 5.186	a = 3.899 c = 5.207	16.14	2.28 (1.31)
$NiSb$	a = 3.934 c = 5.138	a = 3.934 c = 5.145	12.75	5.48 (1.53)
Cu_2Sb	a = 4.001 c = 6.104	a = 4.008 c = 6.112	33.84	2.81 (0.89)
$ZnSb$	a = 6.202 b = 7.742 c = 8.100	a = 6.214 b = 7.756 c = 8.098	82.13	5.17 (2.07)

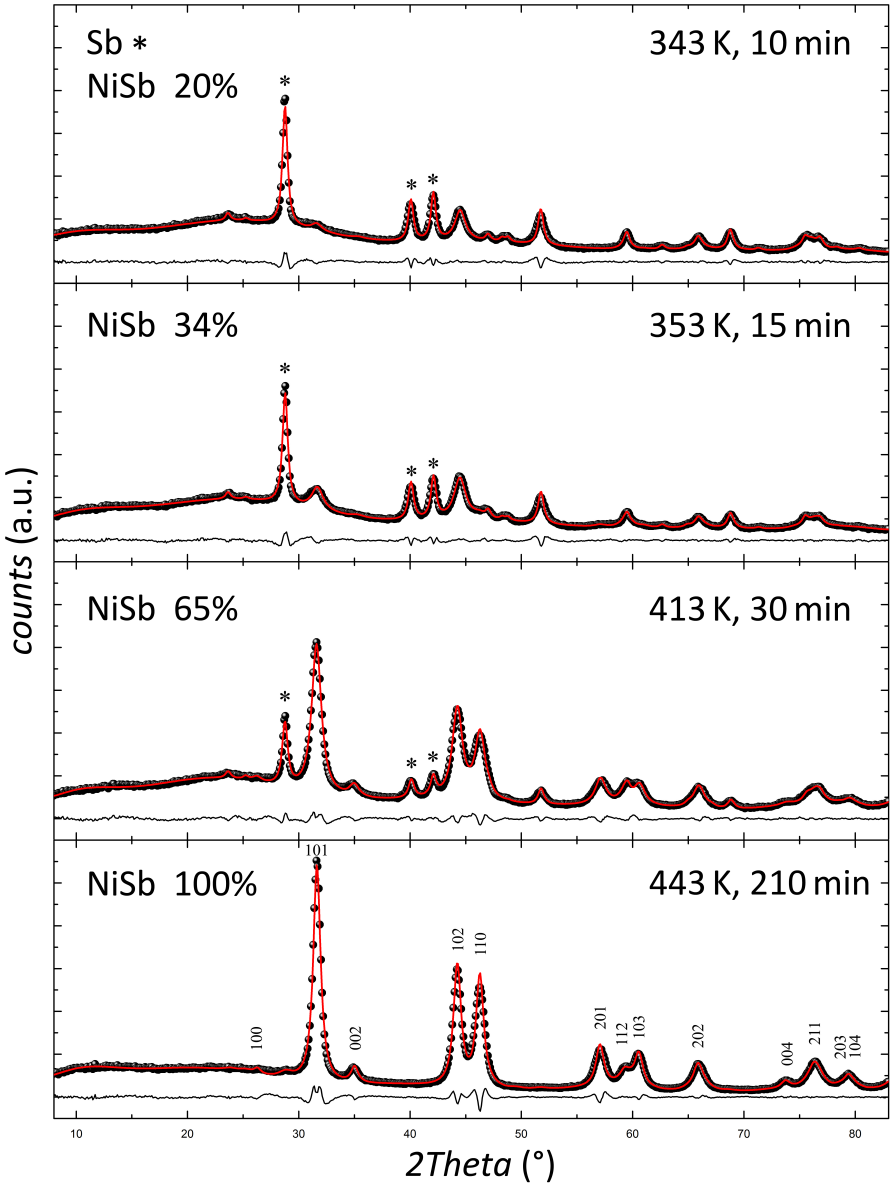

SI-Figure 7.15: Formation of NiSb. Time-dependent and temperature-dependent (ex situ) PXRD: experimental data (black dots), Rietveld fits (red line), and corresponding difference plots (black line) at different reaction temperatures and times.

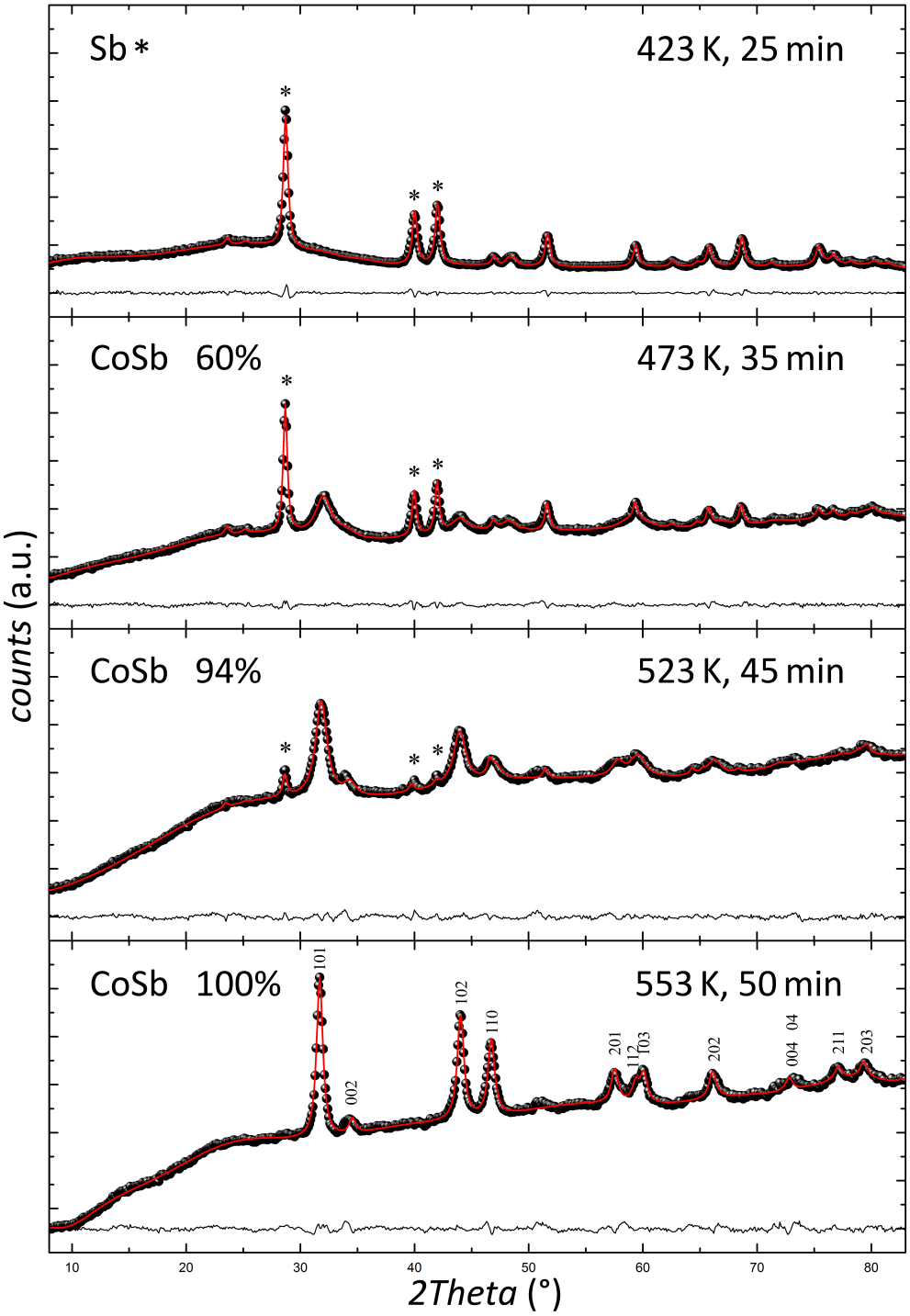

SI-Figure 7.16: Formation of CoSb. Time-dependent and temperature-dependent (ex situ) PXRD: experimental data (black dots), Rietveld fits (red line), and corresponding difference plots (black line) at different reaction temperatures and times.

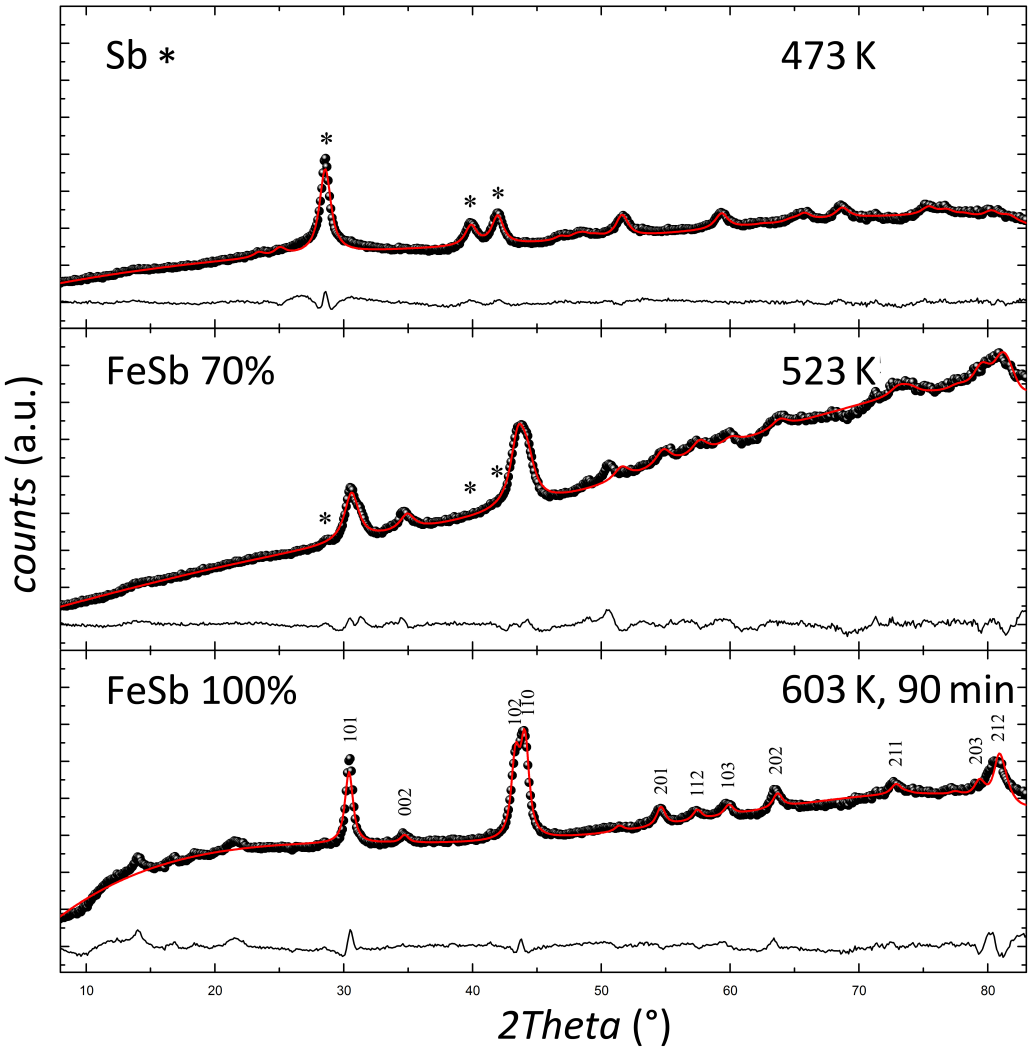

SI-Figure 7.17: Formation of FeSb. Time-dependent and temperature-dependent (ex situ) PXRD: experimental data (black dots), Rietveld fits (red line), and corresponding difference plots (black line) at different reaction temperatures and times.

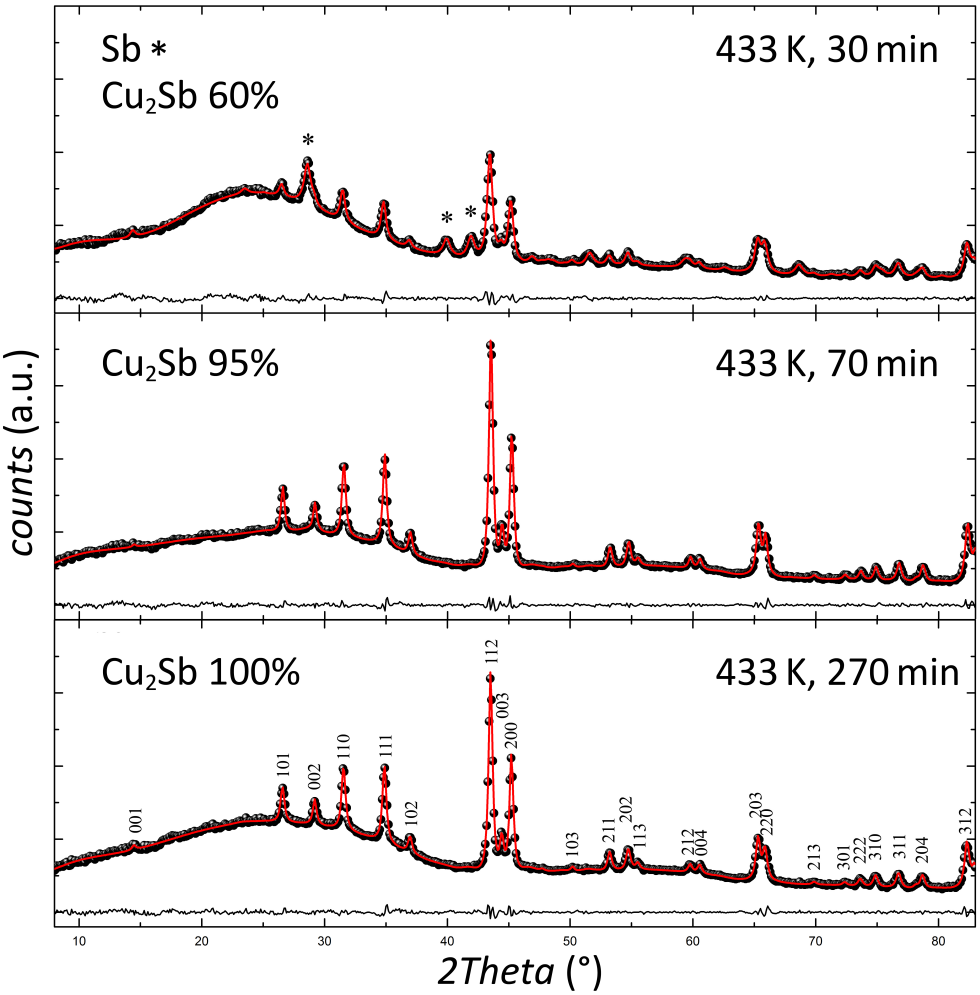

SI-Figure 7.18: Formation of Cu_2Sb. Time-dependent and temperature-dependent (ex situ) PXRD: experimental data (black dots), Rietveld fits (red line), and corresponding difference plots (black line) at different reaction temperatures and times.

Bibliography

[1] Hicks, L.; Dresselhaus, M. *Phys Rev. B.* **1993**, *47*, 12727.

[2] DiSalvo, F. J. *Science* **1999**, *285*, 703.

[3] Snyder, G. J.; Toberer, E. S. *Nature Mater.* **2008**, *7*, 105–114.

[4] Zebarjadi, M.; Esfarjani, K.; Dresselhaus, M. S.; Ren, Z. F.; Chen, G. *Energy Env. Sci.* **2012**, *5*, 5147.

[5] Goldsmid, H. *Applications of Thermoelectricity*; Butler & Tanner Ltd: London, 1960.

[6] Goldsmid, H. *Thermoelectric Refrigeration*; Plenum Press: New York, 1964.

[7] *CRS Handbook of Thermoelectrics: Macro to Nano*, 2nd ed.; Rowe, D., Ed.; CRC Press: Boca Raton, 2006.

[8] Furlong, R.; Wahlquist, E. *Nuclear News* **1999**, 26.

[9] LaLonde, A. D.; Pei, Y.; Wang, H.; Jeffrey Snyder, G. *Mater. Today* **2011**, *14*, 526.

[10] Minnich, A. J.; Dresselhaus, M. S.; Ren, Z. F.; Chen, G. *Energy Env. Sci.* **2009**, *2*, 466.

[11] Snyder, G.; Ursell, T. *Phys. Rev. Lett.* **2003**, *91*, 148301.

[12] S. HÃl'bert, A. M. In *Functional Oxides*; Bruce, D. W., Ed.; John Wiley and Sons, Ltd: West Sussex, 2010; p 203.

[13] Li, J.-F.; Liu, W.-S.; Zhao, L.-D.; Zhou, M. *Asia Mater.* **2010**, *2*, 152.

[14] Biswas, K.; He, J.; Blum, I. D.; Wu, C.-I.; Hogan, T. P.; Seidman, D. N.; Dravid, V. P.; Kanatzidis, M. G. *Nature* **2012**, *489*, 414.

[15] Venkatasubramanian, R.; Siivola, E.; Colpitts, T.; O'Quinn, B. *Nature* **2001**, *413*, 597.

[16] Kauzlarich, S. M.; Brown, S. R.; Jeffrey Snyder, G. *Dalton Trans.* **2007**, 2099.

[17] Shi, X.; Yang, J.; Salvador, J. R.; Chi, M.; Cho, J. Y.; Wang, H.; Bai, S.; Yang, J.; Zhang, W.; Chen, L. *J. Am. Chem. Soc* **2011**, *133*, 7837.

[18] Xie, W.; Weidenkaff, A.; Tang, X.; Zhang, Q.; Poon, J.; Tritt, T. *Nanomaterials* **2012**, *2*, 379.

[19] Koumoto, K.; Wang, Y.; Zhang, R.; Kosuga, A.; Funahashi, R. *Ann. Rev. Mater. Res.* **2010**, *40*, 363.

[20] Koshibae, W.; Tsutsui, K.; Maekawa, S. *Phys. Rev. B* **2000**, *62*, 6869.

[21] Limelette, P.; Hardy, V.; Auban-Senzier, P.; Jérome, D.; Flahaut, D.; Hébert, S.; Frésard, R.; Simon, C.; Noudem, J.; Maignan, A. *Phys. Rev. B* **2005**, *71*, 233108.

[22] He, J.; Liu, Y.; Funahashi, R. *J. Mater. Res.* **2011**, *26*, 1762.

[23] Li, J.; Sui, J.; Pei, Y.; Barreteau, C.; Berardan, D.; Dragoe, N.; Cai, W.; He, J.; Zhao, L.-D. *Energy Env. Sci.* **2012**, *5*, 8543.

[24] Ohtaki, M.; Araki, K.; Yamamoto, K. *J. Elec. Mater.* **2009**, *38*, 1234.

[25] Toberer, E. S.; May, A. F.; Snyder, G. J. *Chem. Mater.* **2010**, *22*, 624.

[26] Heremans, J. P.; Jovovic, V.; Toberer, E. S.; Saramat, A.; Kurosaki, K.; Charoenphakdee, A.; Yamanaka, S.; Snyder, G. J. *Science* **2008**, *321*, 554.

[27] Toberer, E. S.; Zevalkink, A.; Snyder, G. J. *J. Mater. Chem.* **2011**, *21*, 15843.

[28] T. M. Tritt, *Thermal Conductivitiy. Theory, Properties and Applications*; Kluwer Academic: New York, 2004.

[29] Yu, Y. P. C. M. *Fundamentals of Semiconductors: Physics and Materials Properties*; Springer-Verlag GmbH, 2010.

[30] Parrott, J. E. *Thermal Conductivity of Solids*; Pion Ltd, 1975.

[31] Kittel, C. *Introduction to Solid State Physics*; John Wiley and Sons Inc.: New York, 1986.

[32] Born, M. H. K. *Dynamical Theory of Crystal Lattices*; Chapter IV; Oxford University Press: New York, 1954.

[33] Slack, G. *Solid State Physics*; Academic Press: New York, 1979.

[34] Roufosse, M.; Klemens, P. *Phys. Rev. B* **1973**, *7*, 5379.

[35] Ibach, H.; Lüth, H. *Solid-State Physics*, 4th ed.; Springer-Verlag GmbH: Heidelberg, 1981.

[36] Clarke, D. R. *Surf. Coat. Technol.* **2003**, *163-164*, 67.

[37] Winter, M. R.; Clarke, D. R. *J. Am. Chem. Soc.* **2007**, *90*, 533.

[38] Chung, J. D.; McGaughey, A. J. H.; Kaviany, M. *J. Heat Transfer* **2004**, *126*, 376.

[39] Murashov, V.; White, M. In *Thermal Conductivity-Theory, Properties and Applications*; Tritt, T., Ed.; Kluwer Academic / Plenum Publisher: New York, 2004; pp 93–104.

[40] Slack, G. *Phys. Rev. B* **1957**, 829.

[41] Morelli, D.; Meisner, G. *J. Appl. Phys.* **1995**, 3777.

[42] Yang, J. In *Thermal Conductivity-Theory, Properties and Applications*; Tritt, T., Ed.; Kluwer Academic / Plenum Publisher: New York, 2004; pp 1–20.

[43] Magnéli, A.; Virtanen, A. I.; Laaksonen, T.; Hakala, M. *Acta Chem. Scand.* **1949**, *3*, 88.

[44] Magnéli, A.; Blomberg-Hansson, B.; Kihlborg, L.; Sundkvist, G. *Acta Chem. Scand.* **1955**, *9*, 1382.

[45] Gadó, P.; Magnéli, A.; Niklasson, R. J. V.; Brunvoll, J.; Hinton, M. *Acta Chem. Scand.* **1965**, *19*, 1514.

[46] Eyring, L. R.; Tai, L. T. *Annu. Rev. Phys. Chem.* **1973**, *24*, 189.

[47] Putnis, A. *Introduction to mineral sciences*; Cambridge University Press: Cambridge, 1992.

[48] Yamamoto, A.; Nakazawa, H. *Acta Cryst. A* **1982**, *38*, 79.

[49] Press, M.; Ellis, D. *Phys. Rev. B* **1987**, *35*, 4438.

[50] Iijima, S. *Acta Cryst. A* **1973**, *29*, 18.

[51] Booth, J.; Ekström, T.; Iguchi, E.; Tilley, R. *J. Solid State Chem.* **1982**, *41*, 293.

[52] Allpress, J.; Tilley, R.; Sienko, M. *J. Solid State Chem.* **1971**, *3*, 440.

[53] Sundberg, M. *J. Solid State Chem.* **1980**, *35*, 120.

[54] Migas, D. B.; Shaposhnikov, V. L.; Borisenko, V. E. *J. Appl. Phys.* **2010**, *108*, 093714.

[55] Kieslich, G.; Veremchuck, I.; Antonyshyn, I.; Zeier, W. G.; Birkel, C.; Grin, Y.; Tremel, W. *Phys. Chem. Chem. Phys.* **2012**, 15399.

[56] Berak, J. M.; Sienko, M. *J. Solid State Chem.* **1970**, *2*, 109.

[57] Polaczek, A.; Pekala, M.; Obuszko, Z. *J. Phys. Condens. Matter* **1994**, *6*, 7909.

[58] Viswanathan, K.; Brandt, K.; Salje, E. *J. Solid State Chem.* **1981**, *36*, 45.

[59] Harada, S.; Tanaka, K.; Inui, H. *J. Appl. Phys.* **2010**, *108*, 083703.

[60] Wang, H. et al. *J. Elec. Mater.* **2013**, *42*, 654.

[61] Wang, H. et al. *J. Elec. Mater.* **2013**, *42*, 1073.

[62] Orrù, R.; Licheri, R.; Locci, A. M.; Cincotti, A.; Cao, G. *Mat. Sci. Eng. B* **2009**, *63*, 127.

[63] Garay, J. *Ann. Rev. Mater. Res.* **2010**, *40*, 445.

[64] Munir, Z. A.; Anselmi-Tamburini, U.; Ohyanagi, M. *J. Mater. Sci.* **2006**, *41*, 763.

[65] Ju-Nam, Y.; Lead, J. R. *Sci. Total Environ.* **2008**, *400*, 396.

[66] Scheele, M.; Oeschler, N.; Meier, K.; Kornowski, A.; Klinke, C.; Weller, H. *Adv. Funct. Mater.* **2009**, *19*, 3476.

[67] Dong, G.-H.; Zhu, Y.-J.; Chen, L.-D. *J. Mater. Chem.* **2010**, *20*, 1976.

[68] Yin, T.; Liu, D.; Ou, Y.; Ma, F.; Xie, S.; Li, J.-F.; Li, J. *J. Phys. Chem. C* **2010**, *114*, 10061.

[69] Hulbert, D. M.; Anders, A.; Dudina, D. V.; Andersson, J.; Jiang, D.; Unuvar, C.; Anselmi-Tamburini, U.; Lavernia, E. J.; Mukherjee, A. K. *J. Appl. Phys.* **2008**, *104*, 033305.

[70] Bertolino, N.; Garay, J.; Anselmi-Tamburini, U.; Munir, Z. **2002**, *82*, 4487.

[71] Paris, S.; Gaffet, E.; Bernard, F.; Munir, Z. *Scr. Mater.* **2004**, *50*, 691.

[72] Penilla, E.; Kodera, Y.; Garay, J. *Mater. Sci. Eng. B* **2012**, *177*, 1178.

[73] Recknagel, C.; Reinfried, N.; Höhn, P.; Schnelle, W.; Rosner, H.; Grin, Y.; Leithe-Jasper, A. *Sci. Tech. Adv. Mater.* **2007**, *8*, 357.

[74] Kuczynski, G. *Acta Met.* **1956**, *4*, 58.

[75] Krumeich, F. *J. Solid State Chem.* **1996**, *124*, 58.

[76] Coelho, A. *TOPAS Academic, 4.1* **1996**, *124*, Software: Brisbane, Australia.

[77] Inoue, M.; ÅŇhara, S.; Horisaka, S.; Koyano, M.; Negishi, H. *Phys. Status Solidi B* **1988**, *148*, 659.

[78] Pei, Y.; LaLonde, A. D.; Wang, H.; Snyder, G. J. *Energy Env. Sci.* **2012**, *5*, 7963.

[79] Qazilbash, M. M.; Hamlin, J. J.; Baumbach, R. E.; Zhang, L.; Singh, D. J.; Maple, M. B.; Basov, D. N. *Nature Physics* **2009**, *5*, 647.

[80] *Thermal Conductivity-Theory, Properties and Applications*; Tritt, T., Ed.; Kluwer Academic / Plenum Publisher: New York, 2004.

[81] Goldsmid, H. *Proc. Phys. Soc. B* **1956**, 203.

[82] Yu, F.; Zhang, J.; Yu, D.; He, J.; Liu, Z.; Xu, B.; Tian, Y. *J. Appl. Phys.* **2009**, *105*, 094303.

[83] Zeier, W. G.; LaLonde, A.; Gibbs, Z. M.; Heinrich, C. P.; Panthöfer, M.; Snyder, G. J.; Tremel, W. *J. Am. Chem. Soc* **2012**, *134*, 7147.

[84] Plirdpring, T.; Kurosaki, K.; Kosuga, A.; Day, T.; Firdosy, S.; Ravi, V.; Snyder, G. J.; Harnwunggmoung, A.; Sugahara, T.; Ohishi, Y.; Muta, H.; Yamanaka, S. *Adv. Mater.* **2012**, *24*, 3622.

[85] Tokita, M. *J. Soc. Powder Technol. Jpn.* **1993**, 790.

[86] Liu, J.; Shen, Z.; Nygren, M.; Su, B.; Button, T. W. *J. Am. Ceram. Soc.* **2006**, *89*, 2689.

[87] Shen, Z.; Johnsson, M.; Zhao, Z.; Nygren, M. *J. Am. Ceram. Soc.* **2002**, *85*, 1921.

[88] Guo, X.; Xiao, P.; Liu, J.; Shen, Z. *J. Am. Ceram. Soc.* **2005**, *88*, 1026.

[89] Chaim, R.; Shen, Z.; Nygren, M. *J. Mater. Res.* **2004**, *19*, 2527.

[90] Wang, H.; Li, J.-F.; Nan, C.-W.; Zhou, M.; Liu, W.; Zhang, B.-P.; Kita, T. *Appl. Phys. Lett.* **2006**, *88*, 092104.

[91] Tran, T. B.; Hayun, S.; Navrotsky, A.; Castro, R. H. R.; Chaim, R. *J. Am. Ceram. Soc.* **2012**, *95*, 1185.

[92] Fergus, J. W. *J. Eur. Ceram. Soc* **2012**, *32*, 525.

[93] Prikhna, T. et al. *Mat. Sci. Forum* **2012**, *721*, 3.

[94] Chen, W.; Anselmi-Tamburini, U.; Garay, J.; Groza, J.; Munir, Z. *Mater. Sci. Eng. A* **2005**, *394*, 132.

[95] Stedman, N. J.; Cheetham, A. K.; Battle, P. D. *J. Mater. Chem.* **1994**, *4*, 641.

[96] Dreele, R. B. V.; Cheetham, A. K. *Proc. Roy. Soc. A* **1974**, *338*, 311.

[97] Klemens, P. G. *Proc. Roy. Soc. A* **1951**, *208*, 108.

[98] Baxter, J. et al. *Energy Env. Sci* **2009**, *2*, 559.

[99] Shakouri, A.; LaBounty, C.; Abraham, P.; Piprek, J.; Bowers, J. *Mater. Res. Soc. Symp. Proc.* **1999**, 449.

[100] Portehault, D.; Maneeratana, V.; Candolfi, C.; Oeschler, N.; Veremchuk, I.; Grin, Y.; Sanchez, C.; Antonietti, M. *ACS Nano* **2011**, *5*, 9052.

[101] Kim, W.; Zide, J.; Gossard, A.; Klenov, D.; Stemmer, S.; Shakouri, A.; Majumdar, A. *Phys. Rev. Lett.* **2006**, *96*, 045901.

[102] Pei, Y.; Heinz, N. A.; LaLonde, A.; Snyder, G. J. *Energy Env. Sci.* **2011**, *4*, 3640.

[103] Bux, S. K.; Fleurial, J.-P.; Kaner, R. B. *Chem. Comm.* **2010**, *46*, 8311.

[104] Schmoldt, A.; Benthe, H. F.; Haberland, G. *Biochemical pharmacology* **1975**, *24*, 1639.

[105] Bentien, A.; Johnsen, S.; Madsen, G. K. H.; Iversen, B. B.; Steglich, F. *Europhys. Lett.* **2007**, *80*, 17008.

[106] Kleinke, H. *Chem. Mater.* **2010**, *22*, 604.

[107] Xie, J.; Zhao, X.; Cao, G.; Zhao, M.; Zhong, Y.; Deng, L. *Mater. Lett.* **2003**, *57*, 4673.

[108] Xie, J.; Zhao, X.; Yu, H.; Qi, H.; Cao, G.; Tu, J. *J. Alloys. Compd.* **2007**, *441*, 231.

[109] Cable, R. E.; Schaak, R. E. *Chem. Mater.* **2005**, *17*, 6835.

[110] Kumari, L.; Li, W.; Huang, J. Y.; Provencio, P. P. *J. Phys. Chem. C* **2010**, *114*, 9573.

[111] Schaak, R. *Abstr. Pap. Am. Chem. Soc.* **2005**, *229*, U965.

[112] Cushing, B. L.; Kolesnichenko, V. L.; O'Connor, C. J. *Chem. Rev.* **2004**, *104*, 3893.

[113] Birkel, C. S.; Mugnaioli, E.; Gorelik, T.; Kolb, U.; PanthoÌĹfer, M.; Tremel, W. *J. Am. Chem. Soc* **2010**, *132*, 9881.

[114] Riseborough, P. *Adv. Phys.* **2000**, *49*, 257.

[115] Aeppli, G.; Fisk, Z. *Condens. Matter Phys.* **1992**, *16*, 155.

[116] Jonson, M.; Mahan, G. *Phys. Rev. B* **1980**, *21*, 4223.

[117] Sales, B.; Jones, E.; Chakoumakos, B.; Fernandez-Baca, J.; Harmon, H.; Sharp, J.; Volckmann, E. *Phys. Rev. B* **1994**, *50*, 8207.

[118] Harutyunyan, S. R.; Vardanyan, V. H.; Kuzanyan, A. S.; Nikoghosyan, V. R.; Kunii, S.; Wood, K. S.; Gulian, A. M. *Appl. Phys. Lett.* **2003**, *83*, 2142.

[119] Jones, C.; Regan, K.; DiSalvo, F. *Phys. Rev. B.* **1998**, *58*, 16057.

[120] Sato, H.; Abe, Y.; Okada, H.; Matsuda, T.; Abe, K.; Sugawara, H.; Aoki, Y. *Phys. Rev. B* **2000**, *62*, 15125.

[121] Abe, K.; Sato, H.; Matsuda, T. D.; Namiki, T.; Sugawara, H.; Aoki, Y. *J. Phys. Condens. Matter* **2002**, *14*, 11757.

[122] Sun, Y.; Zhang, E.; Johnsen, S.; Sillassen, M.; Sun, P.; Steglich, F.; Bøttiger, J.; Iversen, B. B. *J. Appl. Phys. D* **2010**, *43*, 205402.

[123] Datta, A.; Nolas, G. S. *Eur. J. Inorg. Chem.* **2012**, *2012*, 55.

[124] Birkel, C. S.; Kieslich, G.; Bessas, D.; Claudio, T.; Branscheid, R.; Kolb, U.; Panthöfer, M.; Hermann, R. P.; Tremel, W. *Inorg. Chem.* **2011**, *50*, 11807.

[125] Kieslich, G.; Birkel, C. S.; Stewart, A.; Kolb, U.; Tremel, W. *Inorg. Chem.* **2011**, *50*, 6938.

[126] Melnyk, G.; Tremel, W. *J. Alloys Compd.* **2003**, *349*, 164.

[127] Hu, R.; MitrovicÌĄ, V. F.; Petrovic, C. *Appl. Phys. Lett.* **2008**, *92*, 182108.

[128] Franz, R.; Wiedemann, G. *Annalen der Physik und Chemie* **1853**, *165*, 497.

Curriculum Vitae

Education

2010 - 2013
Ph.D. in Chemistry, Johannes Gutenberg University of Mainz, Germany

2006 - 2010
Diploma in Chemistry, Johannes Gutenberg University of Mainz, Germany

Research Experience

Johannes Gutenberg-University Mainz, Germany

Ph.D. Candidate, September 2010 to June 2013
Advisors: Prof. Dr. [redacted] and Prof. Dr. [redacted]

Max-Planck-Institute CPfS Dresden, Germany

Joint student, weekly research visits
Advisor: Prof. Dr. [redacted]

University of California, Santa Barbara, CA, USA

Joint student, March 2012 to September 2012
Advisors: Prof. Dr. [redacted] and Prof. Dr. [redacted]

Awards and Recognitions

August 2010 - June 2013
Fellowship of the Konrad Adenauer Stiftung, graduate program

December 2010 - June 2013
Colleague of the Graduate School of Excellence MAINZ

March 2012 - September 2012
International Center of Materials Research at UCSB, Santa Barbara

August 2010 - June 2013
Member, SPP 1386, DFG, *"'Nanostructured Thermoelectrics"'*

Februrary 2011
Best poster award, Spring School, German Thermoelectric Society

April 2005
Abitur with honors, exceptional school achievement, computer sciences